Engaging Multiple Mechanisms of Plasticity to Promote Functional Recovery after Stroke

Karam Khateeb

A dissertation

submitted in partial fulfillment of the

requirements for the degree of

Doctor of Philosophy

University of Washington

2025

Reading Committee:

Azadeh Yazdan-Shahmorad, Chair

Steve Perlmutter

Andre Berndt

Program Authorized to Offer Degree:

Bioengineering

University of Washington

Abstract

Engaging Multiple Mechanisms of Plasticity to Promote Functional Recovery after Stroke

Karam Khateeb

Chair of the Supervisory Committee:
Azadeh Yazdan-Shahmorad
Department of Bioengineering

The human brain is responsible for executing a vast range of functions such as movement, somatosensation, visual processing, and cognition. These and other abilities depend critically on a delicate balance between the stability and adaptability of neuronal connections. Neural injuries such as stroke disrupt these connections and often result in serious debilitating effects on the brain's ability to perform critical functions. A major challenge in developing effective rehabilitative treatments for stroke is the absence of a unifying framework for investigating multiple physiological processes in preclinical animal models. In this dissertation, I describe a framework by which we can study various aspects of cortical physiology in non-human primates (NHPs), a clinically relevant animal model, under healthy and stroke conditions (Chapter 2). Although neurons possess a diverse repertoire of plasticity mechanisms to modify and stabilize their connections, stimulation-based stroke therapies have largely focused on Hebbian forms of plasticity. Other mechanisms remain underexplored despite their potential relevance for recovery. I present two approaches to engage homeostatic and Hebbian plasticity mechanisms to induce targeted changes in functional connectivity in NHPs and rodents (Chapters 3 and 4). The combination of these tools and approaches can drive the development of effective rehabilitative stroke treatments to restore the loss of critical functions such as mobility, somatosensation, and visual processing.

Table of Contents

Acknowledgements

It takes a village to earn one PhD. There are contributions from many people throughout my life that have led me to this stage and to whom the least I owe is an acknowledgement.

First, I acknowledge my late paternal grandmother Hamda, who still visits me in my dreams, and who I will always remember for her matriarchal strength, radiant joy, and protective love. Her tight embrace has imprinted onto me forever and continues to transmit to me her strength. I also acknowledge my late paternal grandfather Sobhe Khateeb, to whom I am told I bear physical and behavioral resemblances. Somehow, Sobhe and Hamda managed to raise their youngest son, my father, to become a professor. I thank my maternal grandparents, Ahmad and Suaad Sheikh Suleiman. My grandfather, a retired stone mason, devotedly toiled throughout his life to support his family and descendants. His contagious wit can flood any room with joy. I thank my grandmother, whose loving voice on distant calls and whose hand-knit hats and sweaters still envelop me in the enduring warmth of her love. All my grandparents have taught me to be proud of my roots.

Importantly, I thank my father, Hasan, who has always been my guiding figure. Since I was a child, his spontaneous lectures on genetics and biology have instilled in me an excitement for the study of life and a reverence for the scientific process. Without my father, I may have never considered academia or bioengineering as a field of study. I also thank my mother, Hanan, whose constant love and support are always with me despite the physical distance. I would not be in this position without the great sacrifices she has made for me and my siblings. It was my mother who walked me to school every morning and made sure that I never forgot to touch the lucky branch on my lucky tree while on the way. Having my mother's permission to play in the forest during my childhood augmented my admiration for the natural world. Together, my parents shielded me and my siblings from a troubled world. I also thank my siblings, Rawi, Haya, and my sister-in-law Bri for their unwavering support and belief in me.

I also thank the remainder of my family back home and abroad. This includes the families of my uncles Imad, Baligh, and Sameeh, along with the families of my aunts Lamees and Maysa. Together, they provide me with a strong community with whom I can always find comfort and belonging. I miss them all dearly.

I am forever grateful to Dr. Azadeh Yazdan-Shahmorad for her steadfast support and belief in me. Her mentorship and trust gave me the freedom and encouragement to pursue my passion. Being part of

her lab has been an incredibly rewarding experience that has profoundly shaped my growth as a scientist and as a person.

I am grateful to Dr. Kate O'Connor-Giles, Dr. Scott Gratz, and Dr. Joseph Bruckner for their exceptional mentorship and support. Their investment in my growth during my undergraduate years gave me the confidence and preparation I needed to thrive in graduate school and beyond. Their trust and encouragement helped me see myself as a capable and curious scientist.

I am thankful to my Supervisory Committee members for their guidance and constructive feedback. Dr. Perlmutter, Dr. Berndt, and Dr. Barria have always been charitably available to offer me their scientific and career advice. Their guidance has been invaluable throughout the course of my PhD.

From the Perlmutter lab, I am grateful to Rob Robinson, Logan Murphy, and Ali Sadeghi for generously teaching me their rodent surgical procedures. Without their help, this dissertation would have one less chapter.

I am grateful to all the Yazdan lab members, past and present, who have contributed to my work. I am especially thankful to Toni Haun, our exceptional lab manager, whose resourcefulness and uncanny ability to solve any problem have been nothing short of magical. I am thankful to Anne Pierce, without whom I may still be trying to learn how to work with rats. I am also thankful to my undergraduate mentees who have spent countless hours helping me run experiments.

I am thankful to Zach Ip, whose true name is only known by me. His friendship and lighthearted spirit helped make the journey through my PhD feel shorter and more enjoyable. I will see you in the promised land.

Finally, I would like to thank my best friend, Larissa Grieves, whose steady support over the last three years has been a cornerstone of my journey through this PhD. Her clinical insight as an occupational therapist has also meaningfully shaped my perspective on the future of rehabilitative therapies for stroke patients.

Chapter 1: Introduction

Background and Motivation

The human brain is a complex, dense, labyrinthine ecosystem. It is highly dynamic, a source of stability, and a point of fragility. Our personalities, memories, emotions, and skills are encoded by the trillions of connections between the billions of neurons within our brains. When this dynamic ecosystem is perturbed (e.g. by an injury), it is able to adapt and accommodate its structure in an attempt to maintain its ability to execute the multitude of its functions. However, the complexity of the brain often means that such perturbations can expose its fragility, leading to debilitating outcomes. One such perturbation is neural injury due to stroke.

The Need for Additional Post-Stroke Interventions

Strokes result from disruptions in cerebral blood flow. Ischemic strokes account for approximately 85% of stroke incidences and are caused by thromboembolic occlusions in the cerebral vasculature (Feigin et al., 2021; Virani et al., 2021). This leads to the death of downstream neurons and brain tissue that rely on the occluded blood supply for survival. In one study, approximately 77.4% of ischemic stroke patients reported weakness of the upper limbs (Lawrence et al., 2001). Other common ailments include impaired consciousness (44.7%), impaired cognition (43.9%), dysphagia (difficulty swallowing, 44.7%), and urinary incontinence (48.2%) (Lawrence et al., 2001). Others have also shown that up to 60% of stroke survivors develop significant cognitive impairments within their first year after stroke (Douiri et al., 2013; Guo et al., 2024; El Husseini et al., 2023; Jacquin et al., 2014; Lo et al., 2019). As a result, stroke is a leading cause of long-term disability among adults globally (Donkor, 2018; Feigin et al., 2021; Katan and Luft, 2018; Virani et al., 2021).

One effective method to treat ischemic stroke is to pharmacologically restore blood flow to the affected regions, namely through the use of recombinant tissue plasminogen activator (rtPA) (Clark et al., 2000). Typically, this type of treatment is limited to the first few hours after stroke and can significantly improve patient outcomes (Prabhakaran et al., 2015). However, due to the short treatment window, only about 10-30% of ischemic stroke patients receive rtPA treatment, although this percentage is steadily rising (Adeoye et al., 2011; Koge et al., 2023). Moreover, most patients receiving reperfusion treatments still require additional long-term care and rehabilitative therapy (Cramer, 2018; Hacke et al., 2008; Li et al., 2023). Thus, there is a strong need for additional

interventions that can complement existing rehabilitative treatments to help restore patients' lost abilities, functions, and sense of self.

Stimulation-based approaches have the potential to enhance functional recovery after stroke. One high-profile Phase III clinical trial investigated the use of epidural electrical stimulation of the motor cortex administered concurrently with rehabilitation (Levy et al., 2016). This combined approach aimed to enhance plasticity and promote functional recovery in stroke patients. Although this strategy was successful in a subset of patients, there was no significant difference in overall improvement between the investigational and control groups after four weeks of treatment. This outcome was unexpected given the successes of earlier preclinical and clinical trials (Levy et al., 2016). The failure to meet the primary endpoint has prompted researchers in the field to reexamine the limitations of stimulation-based approaches. One notable limitation of these clinical trials was the predominant reliance on rodent models in the preclinical stage, rather than on non-human primates (NHPs), which offer greater clinical relevance due to their closer anatomical and functional similarity to humans. Another weakness was the lack of efficacy with which the stimulation protocols were able to engage plasticity mechanisms to promote recovery (Levy et al., 2016). This dissertation aims to develop and investigate strategies for engaging diverse plasticity mechanisms to promote functional recovery following neural injury using both rodent and NHP animal models. To achieve this, it is important that we have an understanding of a few key plasticity mechanisms.

Mechanisms of Plasticity

The brain's highly dynamic and plastic disposition can be a natural gateway towards driving functional recovery after stroke. In as early as the 4th century BCE, Aristotle described the mind as a being shaped by experience (McKeon et al., 1967). Remarkably, in 1890, the philosopher William James described the idea of neural plasticity as we know it today in *The Principles of Philosophy*. In this treatise, he described, "Plasticity… means the possession of a structure weak enough to yield to an influence, but strong enough not to yield all at once" (James, 1890). Through this, he argued that our habits and experiences can influence the shape and structure of the brain. This foundational insight paved the way for the work of psychologist Donald Hebb, a seminal figure in the field of neural plasticity.

Hebbian and Spike Timing-Dependent Plasticity

Donald Hebb cemented the concept of experience-dependent plasticity in *The Organization of Behavior*, in which he postulated that synaptic strengths could increase through repeated co-

activation of both presynaptic and postsynaptic neurons (Hebb, 1949). The Hebbian model of plasticity has since guided many of our approaches to stimulation-based stroke therapies (Edwardson et al., 2013). Early empirical evidence of Hebbian plasticity was demonstrated by Bliss and Lømo in 1973. In urethane-anesthetized rabbits, they delivered high-frequency electrical stimulation to the perforant path, which provides input into the dentate gyrus of the hippocampus. By measuring field potentials in the granule cell layer of the dentate gyrus, they observed an input-specific persistent increase in synaptic strength (potentiation) (Bliss and Lømo, 1973). In *ex vivo* rat cortical slice preparations, Markram et al. demonstrated that postsynaptic neuronal firing within a brief time window after presynaptic neuronal firing resulted in the potentiation of that synapse. However, if the postsynaptic neuron fired before the presynaptic neuron, then the synapse would weaken in strength (depression) (Markram et al., 1997). They then demonstrated that blocking N-methyl-D-aspartate receptors (NMDARs) in the postsynaptic neuron prevented this potentiation (Markram et al., 1997). They attributed this spike-timing-dependent potentiation as being reliant on back-propagating action potentials (bAPs) and NMDAR activation. Specifically, they suggested that bAPs facilitate the removal of Mg^{2+} ions that block NMDARs in a voltage-dependent manner, leading to Ca^{2+} influx and subsequent potentiation. Soon afterwards, Bi and Poo demonstrated a similar phenomenon in cultured hippocampal neurons and further elucidated the effect of timing and order of spiking on potentiation and depression (Bi and Poo, 1998). Thus, the term “spike timing-dependent plasticity” (STDP) was established (Song and Abbott, 2001). In the classical STDP curve (Figure 1), long-term potentiation (LTP) occurs when the firing of a presynaptic neuron repetitively and causally contributes to the firing of a postsynaptic neuron within about 20 ms. Conversely, when the postsynaptic neuron fires prior to the presynaptic neuron, this noncausal relationship results in long-term depression (LTD) (Feldman, 2012). Although a multitude of alternative STDP rules have since been elucidated, some of which are synapse-specific and context-dependent (Egger et al., 1999; Feldman, 2012; Fino et al., 2005, 2007; Lu et al., 2007; Sjöström and Häusser, 2006; Tzounopoulos et al., 2004), the canonical STDP relationship has remained a foundational model for stimulation-based stroke treatment strategies (Edwardson et al., 2013).

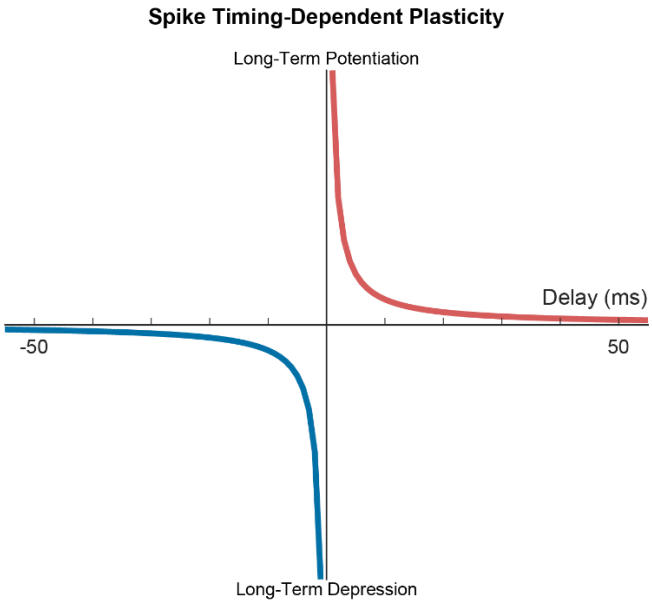

Figure 1. Classical spike timing-dependent plasticity curve. Repeated causal firing of a presynaptic neuron onto a postsynaptic neuron (positive delay) leads to long-term potentiation (LTP). Conversely, repeated noncausal firing in which the postsynaptic neuron fires prior to the presynaptic neuron leads to long-term depression (LTD).

Homeostatic Metaplasticity

One challenge posed by the Hebbian framework of plasticity is explaining how neural circuits maintain stability despite ongoing activity-dependent changes. For example, during Hebbian synaptic strengthening, a strong synapse increases the likelihood of postsynaptic neuronal firing after presynaptic firing. This then would lead to further strengthening, increased correlated activity and more synaptic strengthening. In weaker synapses, noncausal activation of pre- and post-synaptic neurons can lead to the elimination of synapses. Alternatively, the strengthening of one synapse and subsequent increased postsynaptic activation can lead to increased correlated activity with all presynaptic inputs regardless of initial strength. These positive feedback loops left unhindered can therefore lead to loss of input diversity and reduced adaptability (Turrigiano, 2012). Consequently, the need for additional plasticity rules to homeostatically maintain network stability has since become apparent (Abbott and Nelson, 2000; Katz and Miledi, 1968; Miller and MacKay, 1994).

A leading theory of homeostatic plasticity, supported by *in vivo* observations across multiple sensory systems, proposes that the threshold for inducing plasticity is determined by a neuron's prior activity (Bear et al., 1987; Bienenstock et al., 1982; Cooper and Bear, 2012; Guo et al., 2012; Hardingham et al., 2008; Kirkwood et al., 1996). This metaplasticity (other terms include BCM and sliding threshold)

model dictates that periods of high activity increase the activity threshold needed to achieve LTP induction. Meanwhile, periods of low activity decrease the activity threshold for LTP induction. In this manner, neuronal firing rates can be maintained within physiologically plausible limits (Figure 2).

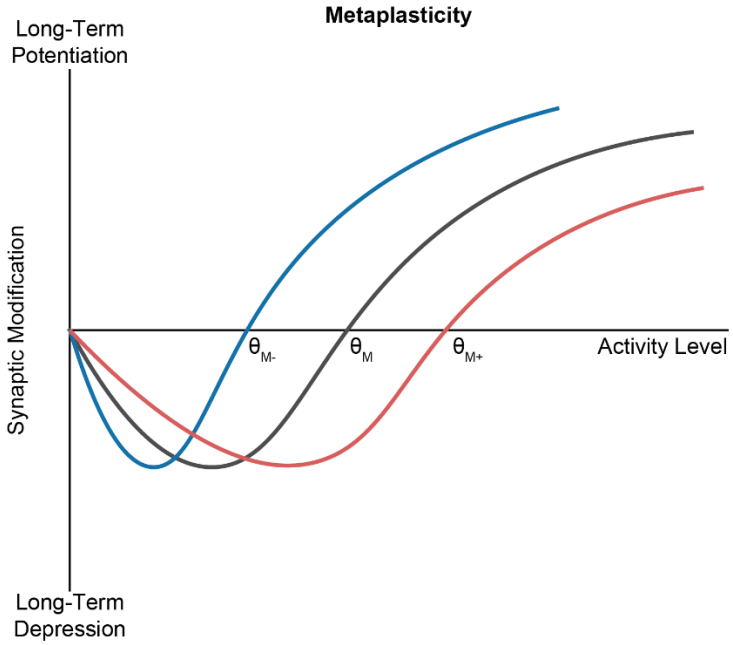

Figure 2. Classical representation of the metaplastic relationship between activity levels and modification threshold. The threshold for LTP induction (θ_M) is a function of previous activity levels. When neurons experience periods of low activity, the modification threshold is shifted leftwards (θ_{M-}) such that lower activity levels are needed to potentiate synapses. When neurons experience periods of high activity levels, the modification threshold is shifted rightwards (θ_{M+}) such that greater activity levels are needed to achieve potentiation.

Sensory deprivation studies have been crucial for the elucidation of metaplasticity mechanisms. In early studies, rearing rats in the dark decreased the LTP induction threshold measured in visual cortex of *ex vivo* slice preparations (Kirkwood et al., 1995, 1996). This modification of the induction threshold is bidirectionally coordinated by altering the levels of NMDARs containing GluN2B subunits (Barria and Malinow, 2005; Gambrill et al., 2011; Philpot et al., 2001, 2003; Quinlan et al., 1999). GluN2B subunits allow for slower NMDAR kinetics that are more optimal coincidence detection compared to GluN2A subunits (Rumbaugh and Vicini, 1999) and improved binding affinity to calmodulin-dependent protein kinase II (Barria and Malinow, 2005), which is crucial for LTP. Thus, reduced LTP induction thresholds corresponded with increased GluN2B-containing NMDARs, while increased thresholds corresponded with a decrease in GluN2B-containing NMDARs (Lee and Kirkwood, 2019; Quinlan et al., 1999).

Homeostatic Inhibition and Disinhibition

Metaplasticity and other forms of homeostatic plasticity have traditionally been regarded as mechanisms that unfold over timescales longer than those associated with Hebbian plasticity *in vivo* (Turrigiano and Nelson, 2000). This difference in timescales can theoretically lead to runaway dynamics during Hebbian plasticity at shorter timescales (Zenke and Gerstner, 2017; Zenke et al., 2017). Thus, the modulation of excitation and inhibition (E/I) ratio within cortical microcircuits has been hypothesized to rapidly regulate Hebbian dynamics. In mouse visual cortex, it was found that excitatory neurons receive inhibitory inputs proportional to the extent of their excitation in an activity-dependent manner (Xue et al., 2014). Whisker deprivation in rats induced a rapid increase in the E/I ratio in the somatosensory cortex through reduced inhibition (disinhibition), serving to maintain stable firing rates (Li et al., 2014). Deprivation-induced disinhibition in somatosensory cortex was also found to facilitate spike timing-dependent LTP (Gambino and Holtmaat, 2012). Importantly for stimulation-based therapies, Hebbian-informed facilitatory stimulation in NHPs was counterbalanced by a rapid onset of inhibition (Andrei et al., 2023).

Stroke and Plasticity

The brain undergoes a slew of structural and functional connectivity changes after stroke. During spontaneous recovery, widespread redundant connectivity can play a significant role in compensating for any lost functions. In regions surrounding the stroke necrotic core, blood flow is typically reduced in what is known as the penumbra. Within the penumbra, the discrepancy between metabolic demand and supply of surviving neurons renders them vulnerable to apoptotic and necrotic cell death, and the subsequent expansion of the necrotic core in the absence of intervention by reperfusion therapies (Dirnagl et al., 1999). However, these surrounding regions which are likely to contain connections redundant to the those of the necrotic core, can also become sites of competitive cortical remapping in an activity-dependent manner (Berger et al., 2007; Brown et al., 2009; Ferezou et al., 2007; Murphy and Corbett, 2009; Nudo et al., 1996; Smits et al., 1991; Winship and Murphy, 2008; Zeiger et al., 2021). For large stroke sizes, however, more distantly related regions must be engaged to facilitate functional recovery (Biernaskie et al., 2005; Frost et al., 2003; Takatsuru et al., 2009). These redundant networks that are crucial for functional recovery can therefore form the substrates over which we can engage mechanisms of plasticity to promote functional recovery following stroke.

Dissertation Overview

The aim of this dissertation is to introduce three methodologies that can lay the groundwork for effectively engaging plasticity mechanisms in a targeted manner to drive functional recovery after neural injuries such as stroke.

In Chapter 2, I describe a multifaceted toolbox for studying cortical physiology in NHPs in healthy and ischemically lesioned brains. With this toolbox, we can simultaneously monitor large-scale neurophysiological and vascular dynamics *in vivo* before, during, and after focal ischemic lesioning. The toolbox also allows for the testing of electrical stimulation paradigms that can be used to investigate stimulation-induced plasticity approaches.

Chapter 3 describes an approach in NHPs to incorporate homeostatic metaplasticity and Hebbian plasticity principles to drive changes in functional connectivity. I show that homeostatically priming the network prior to Hebbian-informed paired electrical stimulation facilitated targeted and network-wide functional connectivity changes in posterior parietal cortex. As a result, these changes became less reliant on the underlying network. I also show that homeostatic priming prior to Hebbian-informed stimulation altered information flow between stimulation sites and their neighboring regions. Importantly, the setup used in this study utilizes tools described Chapter 2, paving the way for testing this approach in the context of ischemically lesioned cortex.

In Chapter 4, I explore how artificially induced network disinhibition can aid in the facilitation of Hebbian changes in functional connectivity. In anesthetized rats, I showed that simultaneous network disinhibition and Hebbian-informed paired electrical stimulation can drive both targeted and network-wide changes in functional connectivity in primary somatosensory cortex. These Hebbian functional connectivity changes were associated with increases in excitability across the network.

This thesis provides a paradigm for the development of stimulation-based interventions that promote post-stroke functional recovery through targeted engagement of neural plasticity mechanisms. By gaining physiological access to large regions of neocortical structures in clinically relevant animal models such as NHPs, we can explore and assess a wide variety of creative approaches towards this aim. Moreover, I demonstrate that the integration of multiple plasticity mechanisms in stimulation-based approaches can enhance our ability to modulate functional connectivity in neocortical circuits. Through an iterative process, the approaches presented here can be combined and refined

to establish novel treatment methods to promote functional recovery in patients suffering from prevalent neurological disorders such as stroke.

Chapter 2: A versatile toolbox for studying cortical physiology in primates

Published as: **Khateeb K**, Bloch J, Zhou J, Rahimi M, Griggs DJ, Kharazia VN, Le MN, Wang RK, and Yazdan-Shahmorad A. (2022). A versatile toolbox for studying cortical physiology in primates. Cell Reports Methods. *2*, 100183.

Summary

Lesioning and neurophysiological studies have facilitated the elucidation of cortical functions and mechanisms of functional recovery following injury. Clinical translation of such studies is contingent on their employment in non-human primates (NHPs), yet tools for monitoring and modulating cortical physiology are incompatible with conventional lesioning techniques. To address these challenges, we developed a toolbox validated in seven macaques. We introduce the photothrombotic method for inducing focal cortical lesions, a quantitative model for designing experiment-specific lesion profiles, and optical coherence tomography angiography (OCTA) for large-scale (~5 cm^2) monitoring of vascular dynamics. We integrate these tools with our electrocorticographic array for large-scale monitoring of neural dynamics and testing stimulation-based interventions. Advantageously, this versatile toolbox can be incorporated into established chronic cranial windows. By combining optical and electrophysiological techniques in NHP cortex, we can enhance our understanding of cortical functions, investigate functional recovery mechanisms, integrate physiological and behavioral findings, and develop neurorehabilitative treatments.

Motivation

The primate neocortex encodes for complex functions and behaviors, the physiology of which are yet to be fully understood. Such an understanding in both healthy and diseased states can be crucial for the development of effective neurorehabilitative strategies. However, there is a lack of a comprehensive and adaptable set of tools that enables the study of multiple physiological phenomena in healthy and injured brains. Therefore, we developed a toolbox with the capability to induce targeted cortical lesions, monitor dynamics of underlying cortical microvasculature, and record and stimulate neural activity. With this toolbox we can enhance our understanding of cortical functions, investigate functional recovery mechanisms, test stimulation-based interventions, and integrate physiological and behavioral findings.

Introduction

The primate neocortex is responsible for a variety of complex tasks and behaviors, including long-term memory storage, sensory processing, and movement. Historically, both lesioning and neurophysiological studies have been critical for elucidating functions of specific cortical regions (Ferrier, 1876) such as somatosensory (Borich et al., 2015; Brinkman et al., 1985; Gerlai et al., 2000), visual (Humphrey, 1974; Wurtz and Goldberg, 1972), auditory (Heffner and Heffner, 1986), and posterior parietal (Murphy et al., 2016; Vallar et al., 1994) cortices. Recently, such strategies have also been employed to investigate mechanisms of plasticity and recovery following injury (Friel et al., 2007; Guo et al., 2021; Harrison et al., 2013; Kaeser et al., 2010; Khanna et al., 2021; Liu and Rouiller, 1999; Nudo and Milliken, 1996; Nudo et al., 1996; Padberg et al., 2010; Pons et al., 1988; Xerri et al., 1998). The study of these phenomena in non-human primate (NHP) models with strong evolutional and physiological relevance to the human cortex is critical for understanding fundamentals of cortical physiology and designing novel clinical treatments for cortical injury. This was particularly highlighted following the lack of success of clinical trials for novel stroke therapies in recent decades. One major contributing factor to this lack of success has been attributed to a heavy reliance on rodent studies and a lack of pre-clinical studies in NHPs (Kotak et al., 2005; Levy et al., 2016). Thus, there is a strong need to expand the tools available for studying NHP cortical physiology for clinical translation.

Typical strategies for investigating *in vivo* NHP cortical physiology include either monitoring or perturbing the native cortical activity then correlating neural activity with behavior. Neural activity is frequently monitored through electrical recording, or calcium imaging, while perturbations include lesioning, electrical stimulation, or optogenetic manipulation (Acker et al., 2016; Tremblay et al., 2020). Previously, we developed a large-scale interface enabling optogenetic neuromodulation in concert with simultaneous electrical recording (Ledochowitsch et al., 2015; Yazdan-Shahmorad et al., 2015, 2016, 2018c, 2018a, 2018b). However, to the best of our knowledge, there is no single unifying paradigm through which the full spectrum of strategies can be combined for the unhindered investigation of cortical physiology in NHPs. Conventional lesioning techniques lack compatibility with tools for monitoring and modulating cortical physiology and lack flexibility in controlling lesion location and extent. Here, we adapt and integrate in NHPs a versatile focal ischemic lesioning technique with large-scale monitoring of cortical vascular dynamics, and electrophysiological recording and stimulation. The mutual compatibility of the integrated tools within this versatile

toolbox enables for the inclusion or exclusion of any of the tools depending on experimental needs. Importantly, with large-scale stable optical access, this toolbox can be combined with established chronic cranial windows for optical stimulation and imaging techniques such as optogenetics and calcium imaging, respectively.

Commonly utilized NHP cortical lesioning techniques are challenging to employ. One method of lesioning cortex in NHPs is through middle cerebral artery occlusion (Maeda et al., 2005; Virley et al., 2004). Because middle cerebral artery occlusion is used to mimic ischemic stroke as observed in the clinic, the resulting lesions are broad and are constrained only to regions downstream of the middle cerebral artery. Moreover, obtaining access to the middle cerebral artery for occlusion requires complex surgical intervention regardless of the occlusion technique. Similarly, common focal cortical lesioning techniques such as endothelin-1 (Dai et al., 2017; Teo and Bourne, 2014), electrocoagulation (Nudo et al., 2003; Xerri et al., 1998), ibotenic acid (Kaeser et al., 2010; Liu and Rouiller, 1999), cooling (Brinkman et al., 1985), and aspiration (Heffner and Heffner, 1986; Padberg et al., 2010; Pons et al., 1988) also involve technically challenging surgical procedures that are susceptible to variability across animals. Importantly, these techniques lack compatibility with tools for monitoring cortical physiological dynamics during lesion formation and recovery.

When conducting lesion studies in NHPs, it is critical that lesions are validated *in vivo* for studies involving long-term post-lesion behavioral and physiological assessment. Current lesion validation methods primarily consist of behavioral assessment and post-mortem histological analysis (Kaeser et al., 2010; Liu and Rouiller, 1999; Murata et al., 2008). Methods of *in vivo* lesion validation, in addition to behavioral assessment, include magnetic resonance imaging (MRI) (Le Friec et al., 2020), or visual assessment of tissue blanching due to devascularization (Nudo and Milliken, 1996; Nudo et al., 1996; Xerri et al., 1998). While MRI validation can provide both anatomical and physiological assessment of lesion induction, it exhibits poor spatial and temporal resolution (Baran and Wang, 2016). Moreover, visual assessment can result in unreliable estimation of lesion boundaries (Xerri et al., 1998). The reliance on behavioral and post-mortem histological analysis alone is deficient of direct anatomical and physiological lesion validation during the lifetime of the animal. Ideally, lesion validation would be accomplished reliably, and in a manner that allows for monitoring of anatomical and physiological changes over the course of recovery.

In addition to these techniques, the investigation of cortical neurophysiological dynamics can play an important role in enhancing our understanding of cortical physiology and in developing

neurorehabilitative strategies. The monitoring of neurophysiological dynamics in neuroscience is often accomplished through electrical stimulation and recording of neural activity. For example, intracortical microstimulation of primary motor cortex following a lesion has been crucial for elucidating the remapping of cortical somatotopic representations (Nudo and Milliken, 1996; Nudo et al., 1996). In other cortical regions, electrophysiological recordings have also been used to monitor neural activity following lesion induction (Padberg et al., 2010; Schmid et al., 2009). The incompatibility of the lesioning methods used in these studies with recording and stimulation techniques, however, prevents the monitoring of neural activity simultaneously during lesion formation. Ideally, neural activity would be recorded before, during, and after lesion formation, while stimulation-based interventions could be tested after lesioning.

In this study, we addressed the technical shortcomings of studying cortical physiology in NHPs. We successfully demonstrate the combination of a photochemical lesion induction technique with a controlled spatial profile, an *in vivo* lesion validation method with high spatial resolution, and the ability to simultaneously monitor the underlying neural activity and blood flow as lesions form at a large scale (~5 cm^2). The utility of implementing these techniques in NHPs is expanded by the capability to simultaneously monitor neural activity and test stimulation-based interventions. Moreover, the sizes of focal lesions induced with our toolbox are comparable to previously reported focal lesions capable of eliciting behavioral deficits (Murata et al., 2008; Padberg et al., 2010). Importantly, the tools presented here are compatible with previously established interfaces offering large-scale access for optical and electrical stimulation as well as imaging (Chen et al., 2002; Griggs et al., 2021b; Macknik et al., 2019; Trautmann et al., 2021; Yazdan-Shahmorad et al., 2016), providing unparalleled access to the primate cortex. Although not demonstrated here, the tools described in this study can easily be adapted for use in smaller model organisms, expanding their utility beyond research groups with access to macaques. Through this integrative approach, the large-scale monitoring of cortical network activity and reorganization concurrently with vascular dynamics expands the questions and interventions we can explore, profoundly impacting the development of neurorehabilitative therapies.

Results

To address the challenges of studying cortical physiology in NHPs, we developed a toolbox that allows for targeted focal lesioning, large-scale imaging of cortical blood flow, and large-scale electrophysiological recording and stimulation. Our toolbox is comprised of the photothrombotic

technique for inducing focal ischemic lesions, optical coherence tomography angiography (OCTA) imaging for *in vivo* lesion validation, histological validation, a computational model for designing lesion profiles, and electrocorticographic (ECoG) recording during lesion formation. We implemented the photothrombotic technique (Figure 1) in 7 adult macaques (monkeys A-G) and validated the disruption of cortical blood flow *in vivo* using OCTA imaging as described in the STAR Methods. Lesions were induced by illuminating through an opaque apertured mask (Figure 1A) in a 25 mm diameter cranial window with an uncollimated white light source following intravenous infusion of the photoactive dye Rose Bengal (Figure 1B). Photoactivation of Rose Bengal in the cerebral vasculature results in the release of reactive oxygen species, subsequent endothelial cell damage, platelet activation, and vascular occlusion due to the formation of thrombi. We tested the effects of a range of aperture diameters (0.5 to 2 mm) and illumination intensities (0.1 to 18.6 mW) on lesion size. To test these variables, we used an opaque mask with multiple apertures of various diameters dispersed throughout the cranial window (Supplementary Figure 1). A single uncollimated white light source was used to illuminate through the mask apertures such that the light intensity was highest through centrally located apertures. Through this approach we were able to test a variety of illumination parameters while reducing the number of animal subjects, time under anesthesia, and the number of light sources to practical levels.

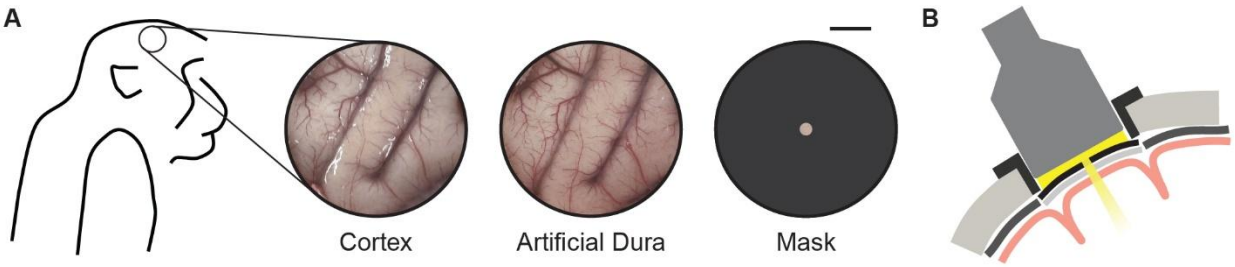

Figure 1. Schematic of photothrombotic technique application to induce focal cortical ischemic lesions. (A) Following a 25 mm diameter circular craniotomy, a thin, transparent artificial dura was placed over the exposed cortical surface. Next, an apertured mask was placed on top of the artificial dura. Scale bar is 5 mm. (B) Coronal schematic of light illumination through the apertured mask following intravenous Rose Bengal infusion.

Validation of Neuronal Cell Loss by Histology and Immunohistochemistry

Approximately 4 hours after the end of illumination, animals were perfused with 4% paraformaldehyde (PFA) and the brains were extracted. Prior to histological staining of coronal slices, we observed bright pink areas corresponding with the illuminated regions (Figure 2A), suggesting that the formation of thrombi occluded the vasculature, entrapping the pink-colored Rose Bengal even

after perfusion. We then stained coronal sections of the brains for Nissl bodies (Figure 2B,C). In illuminated regions, we observed areas characterized by well-defined borders that lacked Nissl staining, demonstrating cell loss in those regions (Figure 2B,C). We identified these areas as lesions. To test for neuronal cell loss, we performed NeuN staining and observed similarly defined borders in the illuminated regions (Supplementary Figure 2). Depending on aperture sizes and illumination intensities, lesion depths extended through all cortical layers. To gain perspective of the relative locations and sizes of the lesions, we reconstructed the lesions in three-dimensional space using the coronal Nissl-stained sections (Figure 2D-H). With this method, we measured lesion volumes ranging between 1.7 mm^3 and 35.4 mm^3. We observed 22 histologically detected lesions out of 30 illuminated areas across monkeys B-E. Notably, high intensity illumination through centrally located apertures more consistently resulted in histologically detected lesions (lesion volumes ranging from 10.1 mm^3 to 31.2 mm^3, median of 19.6 mm^3) compared to lower intensity illumination in peripheral apertures (volumes 0 mm^3 to 35.4 mm^3, median of 2.9 mm^3).

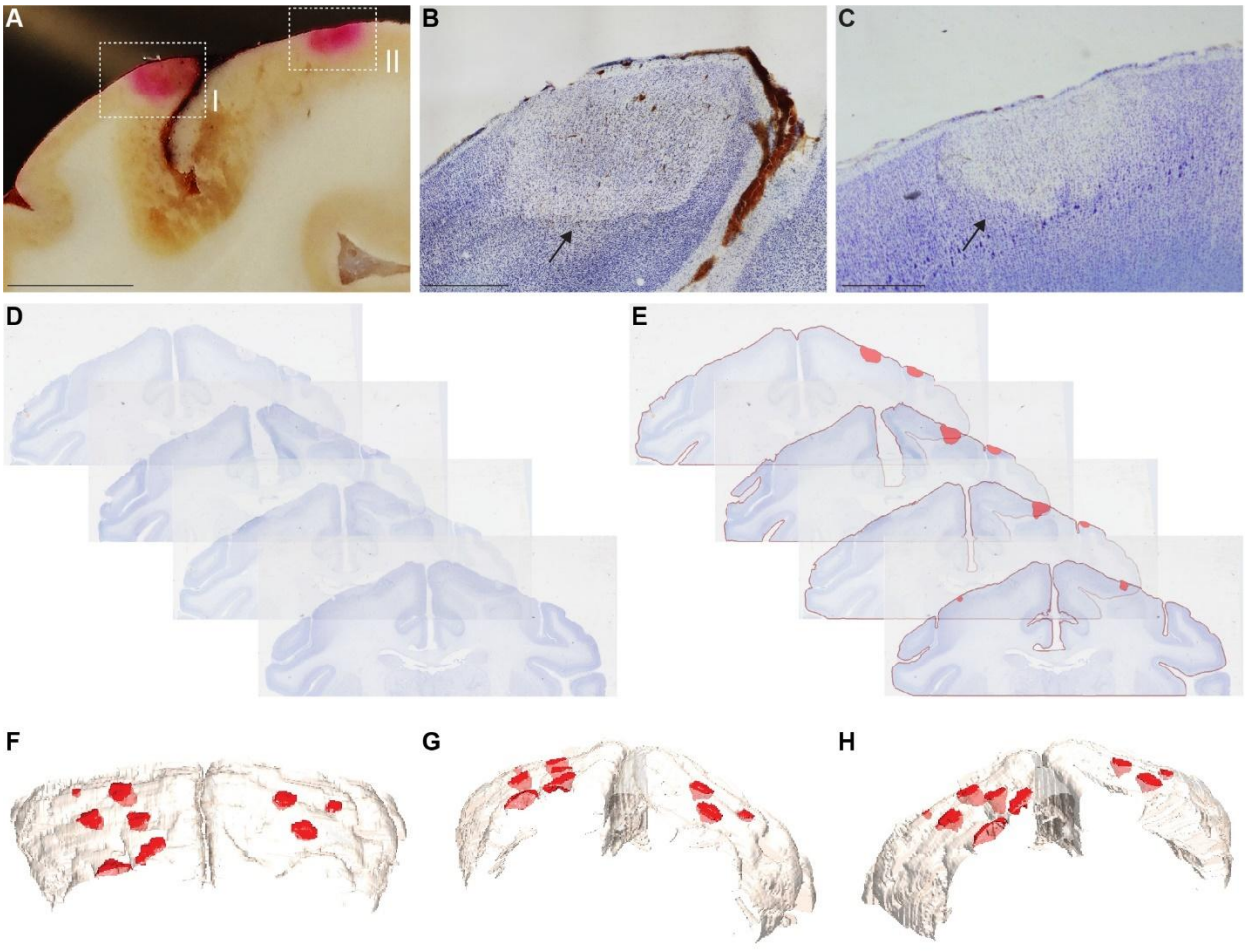

Figure 2. Histological lesion validation and reconstruction. (A) Unstained coronal section from monkey A. Pink regions corresponding with illuminated regions highlighted in boxes I and II indicate the presence of Rose Bengal entrapped in the cortical microvasculature. Scale bar is 5 mm. (B,C) Coronal Nissl-stained slice adjacent to the slice shown in panel (A), showing cell loss in the region encapsulated in box I (B) and II (C) and indicated by the black arrows. Scale bars are 1 mm. (D,E) Reconstruction of induced lesions in 3D space was done by first co-registering coronal Nissl-stained slices (D), followed by identification of lesion boundaries (E). (F-H), 3D reconstruction of lesions in monkey C from three different angles.

Optical Coherence Tomography Angiography for Large-Scale Blood Flow Imaging and *In Vivo* Lesion Validation

The extent of optical access afforded by our toolbox enables for the application of large-scale imaging techniques such as OCTA imaging. OCTA is a non-invasive angiographic technique that is capable of imaging functional vascular networks within tissue beds *in vivo*. OCTA has been demonstrated to detect inflammatory conditions in skin (Deegan and Wang, 2019; Deegan et al., 2018a), eyes (Kashani et al., 2017), and brain (Li et al., 2018; Park et al., 2018). While post-mortem histological analysis is the predominant method of measuring focal lesion size, we introduce OCTA as an *in vivo* tool to image blood flow in the cortical microvasculature, validate lesion induction, and measure ischemic lesion sizes.

OCTA imaging 3 hours after illumination revealed clear localized disruptions in cortical blood flow compared to baseline images in the illuminated regions (Figure 3, Supplementary Figure 3), as evidenced by a lack of functional blood vessels in regions interrogated by the photothrombotic illumination. Thus, we demonstrated the ability to validate lesion induction *in vivo* through OCTA imaging.

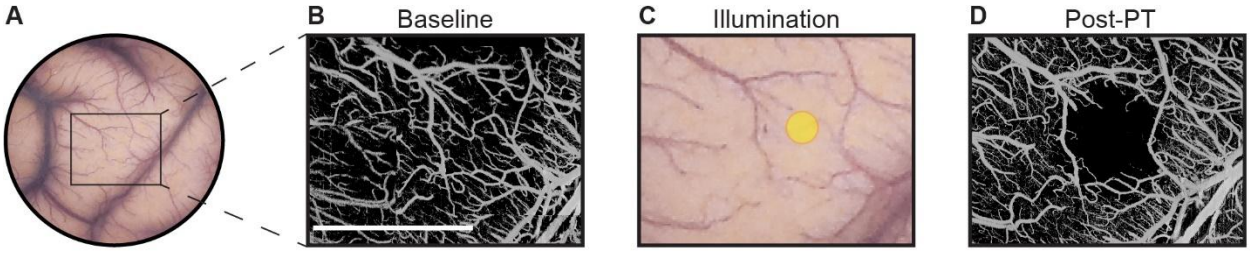

Figure 3. Optical coherence tomography angiography (OCTA) validation of lesion induction. (A) Surface of sensorimotor cortex through an artificial dura in monkey C. (B) OCTA imaging of the rectangular area prior to lesion induction. Scale bar is 5 mm. (C) Illumination of a cortical region of interest indicated by the yellow circle following intravenous Rose Bengal infusion. (D) OCTA imaging 3 hours post-photothrombosis.

We then compared OCTA and histological lesion validation modalities (Figure 4A-C). Not all illuminated regions resulted in lesions detected through both modalities. Across monkeys B through E, we illuminated 30 regions to induce photothrombosis. 26 of the illuminated regions were imaged

within the OCTA field of view (FOV), of which 16 lesions were detected through OCTA imaging. 15 of the 16 OCTA-detected lesions were later confirmed histologically with one lesion undetected histologically. Similar to histology, illumination through centrally located apertures corresponding with higher light intensities more consistently resulted in lesions detected with OCTA compared to peripheral apertures with lower light intensities. Additionally, 8 of the 10 imaged regions in which no lesions were detected in OCTA images corresponded with regions occupied by large blood vessels. Of those 8 regions, only 3 resulted in lesions detected through histology (3.7 to 17.6 mm^3). Of the 22 histologically detected lesions, 15 were detected through OCTA. Histologically detected lesions within the OCTA FOV that were not detected in OCTA images (4 lesions) were likely a result of illumination of large vessels (3 lesions), or the lesion may have been too small to be detected via OCTA imaging (1 lesion, 2.83 mm^3). Notably, OCTA detection of lesions was unsuccessful in all instances in which the illuminated region coincided with large blood vessels, regardless of histological detection (Supplementary Figure 4). Because of the inconsistencies of large vessel illumination due to differences in optical and biological properties, we excluded data corresponding with large vessel illumination from further analysis.

We then quantitatively assessed OCTA-measured lesion diameters as *in vivo* proxy measurements of histologically measured lesion diameters (Figure 4B). We observed a positive linear relationship between OCTA-measured lesion diameters and histologically measured lesion diameters, with a Pearson's correlation coefficient of 0.90 ($p = 3.9e-7$; Figure 4B). We then assessed the correlation between histologically measured lesion depths and OCTA-measured lesion diameters (Figure 4C). We observed a positively correlated linear relationship between histological lesion depth and OCTA-measured lesion diameter with a Pearson's correlation coefficient of 0.70 ($p = 0.0011$; Figure 4C). Interestingly, we also observed a significant positive correlation between both histologically measured lesion depths and diameters ($r = 0.81$; $p = 5.3e-6$; Supplementary Figure 4). Importantly, our results demonstrate that OCTA-measured lesion diameter is highly correlated to histologically measured diameters.

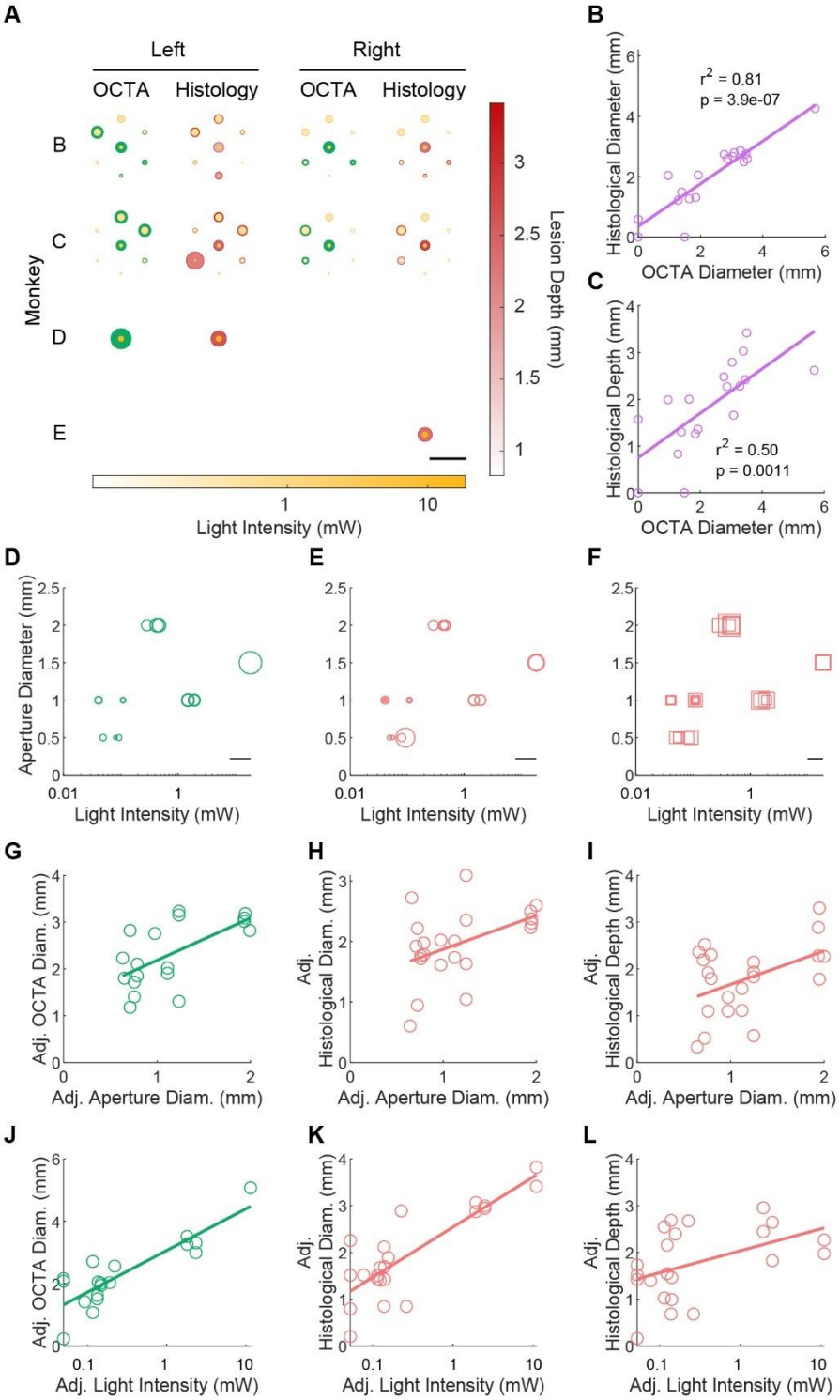

Figure 4. Comparison of OCTA and histological lesion validation and effect of illumination parameters. (A) Schematic demonstrating the OCTA-measured lesion diameters (green circles) in the illuminated regions (aperture diameter represented by yellow circles) of both hemispheres for monkeys B-E. The shading of the yellow circles indicates illumination intensity. The histologically measured lesion diameters are also shown (pink circles), with the shading indicating lesion depth. Scale bar is 10 mm. (B) OCTA-measured and

histologically measured lesion diameters were highly correlated (r = 0.90, p = 3.94e-7). (C) OCTA-measured lesion diameters also correlated with histologically measured lesion depth (r = 0.70, p = 0.0011). (D) Combined effect of aperture diameter and illumination intensity on histologically measured lesion depth. The width of the square markers denotes histologically measured lesion depth. Scale bar is 2 mm. (E) Combined effect of aperture diameter and light intensity on OCTA-measured lesion diameter. Circular marker diameters represent OCTA-measured lesion diameter. Scale bar is 5 mm. (F) Combined effect of aperture diameter and light intensity on histologically measured lesion diameter, where the diameter of the circular markers represents histologically measured lesion diameter. Scale bar is 5 mm. (G) Partial correlation coefficients (r) between illumination parameters (aperture diameter and log-transformed light intensity) and histologically measured lesion depth and diameter, and OCTA-measured lesion diameter along with their respective p-values.

Illumination Parameters Determine Lesion Size

To determine the degree to which the illumination aperture diameter and intensity modulated the resulting lesion depth and diameter, we calculated the partial correlations between the illumination variables and each lesion metric (lesion depth and diameter). The partial correlations for log-transformed light intensity were 0.46 (p = 0.037) for histologically measured lesion depth, 0.84 (p = 2.2e-6) for histologically measured lesion diameter, and 0.86 (p = 7.8e-6) for OCTA-measured lesion diameter (Figure 4G). The partial correlations for aperture diameter were 0.46 (p = 0.038) for histologically measured lesion depth, 0.46 (p = 0.037) for histologically measured lesion diameter, and 0.63 (p = 0.0066) for OCTA-measured lesion diameter (Figure 4G). These results indicate that the light intensity and the aperture diameter are both significant determinants of the lesion size and shape.

Prediction of Lesion Size by Simulation of Light Propagation through Cortical Tissue

The utility of this lesioning tool can be expanded by the development of a model informed by the results of this study to predict the sizes of lesions induced by illumination parameters tested here and beyond. We incorporated both light intensity and aperture diameter into a biophysically inspired model to jointly predict both lesion diameter and depth. Photothrombotic lesions arise due to thrombi formation and subsequent cell death mediated by the topography of the underlying microvasculature. As such, we developed a two-stage modeling process in which we simulated photons penetrating brain tissue (Figure 5A) to generate a profile of the spatial fluence distribution (Figure 5B) and transformed fluence contours to recreate the lesion shapes observed through histology (Figure 5C,D, see STAR Methods for details). Using this method, we identified the best optical properties as a gray matter absorption coefficient of 0.395 mm^{-1}, gray matter scattering coefficient of 53.6 mm^{-1}, white matter absorption coefficient of 0.09 mm^{-1}, white matter scattering

coefficient of 54.066 mm^{-1}, and a spatial fluence distribution threshold for lesion induction of 19.9 $\mu W/mm^2$.

From identified best-matching light simulations, we quantified the degree to which they predict lesion shapes and sizes. We observed that while the simulation results qualitatively align with the lesion profiles, the light simulation alone was not adequate for explaining the observed lesions. By using the maximal depth and average diameter of individual fluence threshold contours of the simulation as predictions of their corresponding lesion profiles, we observed that the contours resulted in an r-squared value of -0.04 for lesion depth and 0.32 for diameter. These results indicate that the extent of induced photothrombotic ischemic lesions *in vivo* is not simply a function of the fluence profile in the cortex but is likely also governed by biological factors such as vascular topography.

We therefore incorporated a scaling process to transform the light intensity contours to the biological lesion profiles observed through histology (Figure 5C,D). The depth did not scale linearly well, however, as the best linear scaling of depth yielded an r-squared value of 0.13 (Supplementary Figure 5). From examining the residuals, we observed that square root transforming the depth before linear scaling would yield a more accurate prediction (Supplementary Figure 5). Indeed, by square root transforming the depth and scaling by a factor of 1.6969 we obtained an r-squared value of 0.41 (Figure 5E). We observed that the diameters from the simulation scaled linearly to match the diameters observed from histology, with a scaling factor of 0.726 yielding an r-squared value of 0.82 (Figure 5F). Interestingly, although our model was developed based on histologically derived lesion contours, the resulting model-derived lesion diameters were also highly predictive of OCTA-measured lesion diameters with an r-squared value of 0.60 (Figure 5G). Thus, our quantitative model can accurately predict lesion shape, diameter, and depth.

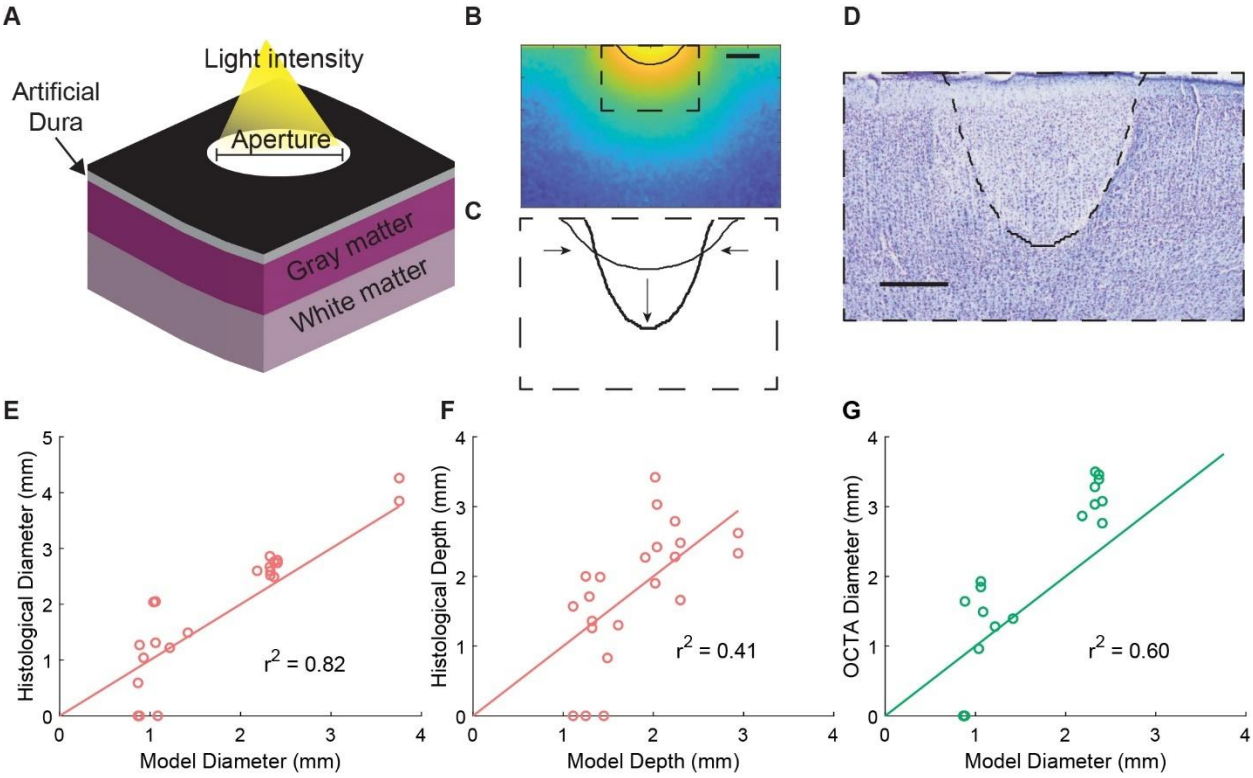

Figure 5. Prediction of lesion size by simulation of light propagation through cortical tissue. (A) Schematic of simulated cortical volume with our experimental setup. An uncollimated light beam passes through an aperture and a transparent artificial dura (0.5 mm thick), into gray and white matter of a virtual cortical medium. Gray matter thickness is 2.5 mm. (B) A contour is identified from the light profile matching the light intensity threshold (19.9 μW/mm^2) most closely matching the lesions. Scale bar is 100 μm. (C) The light intensity contour is scaled to generate a biological lesion contour. Scaling factors were obtained through regression on our dataset of simulated lesion dimensions and corresponding histologically measured lesions. (D) Predicted lesion contour overlayed on a coronal Nissl-stained slice of a corresponding lesion from monkey B. Scale bar is 50 μm. (E-G) Simulated lesions accurately predict histologically measured lesion depths (0.41 r-squared) (E) diameters (0.82 r-squared) (F), and OCTA-measured diameters (0.60 r-squared) (G).

Large-Scale Neurophysiological Recording Before, During, and After Lesion Formation

A valuable tool for studying neurophysiological dynamics following cortical lesioning *in vivo* is the ability to record neural activity. In monkeys D and E we used a semi-transparent 32-electrode ECoG array to record neural activity in sensorimotor cortex during the formation of a lesion (Figure 6A). The transparency of the ECoG array allowed for the induction of a lesion by illuminating through the array. For monkeys D and E, only a single region in the center of the cranial window was illuminated with a 1.5 mm diameter aperture to induce photothrombosis unilaterally. Similarly, the transparency also enabled imaging of the underlying cortical microvasculature by OCTA to confirm the presence of the

lesion (Figure 6A,B). We recorded baseline local field potentials (LFPs) for 30 minutes, followed by 30 minutes during the illumination period, and for up to three hours following illumination.

To measure the effect of lesioning on neural activity levels, we analyzed the changes in gamma band (30-59 Hz) signal power from LFPs recorded during the formation of the lesions. The analysis of gamma band signals is demonstrated here as a relevant example frequency band of interest and as an indicator of local activity levels (Buzsáki and Wang, 2012). Among other roles, gamma activity also exhibits a conserved association with attention and movement in sensorimotor cortex across species, evidence of which includes NHP and human ECoG studies (Aoki et al.; Bouyer et al., 1981; MacKay and Mendoncc ą, 1995). The average gamma power was calculated over the course of 30 minutes of baseline activity, and between 2.5 to 3 hours after the illumination period (Figure 6C). We calculated the change in power across the array and identified regions with statistically significant reductions in gamma power as corresponding to the lesioned areas (left-tailed paired t-test, family-wise error rate < 0.001). As expected, channels near the illuminated region exhibited significant decreases in gamma power in both monkeys D and E compared to more distant regions (one-way ANOVA, monkey D: $p = 5.2e-9$; monkey E: $p = 1.0e-5$; Figure 6C,D). Notably, we demonstrated the capability to monitor neurophysiological dynamics during lesion formation. Here, the reduction in gamma power was observed early during the illumination period across all channels, after which distant channels returned to baseline levels while channels near the illuminated region remained suppressed (Figure 6E).

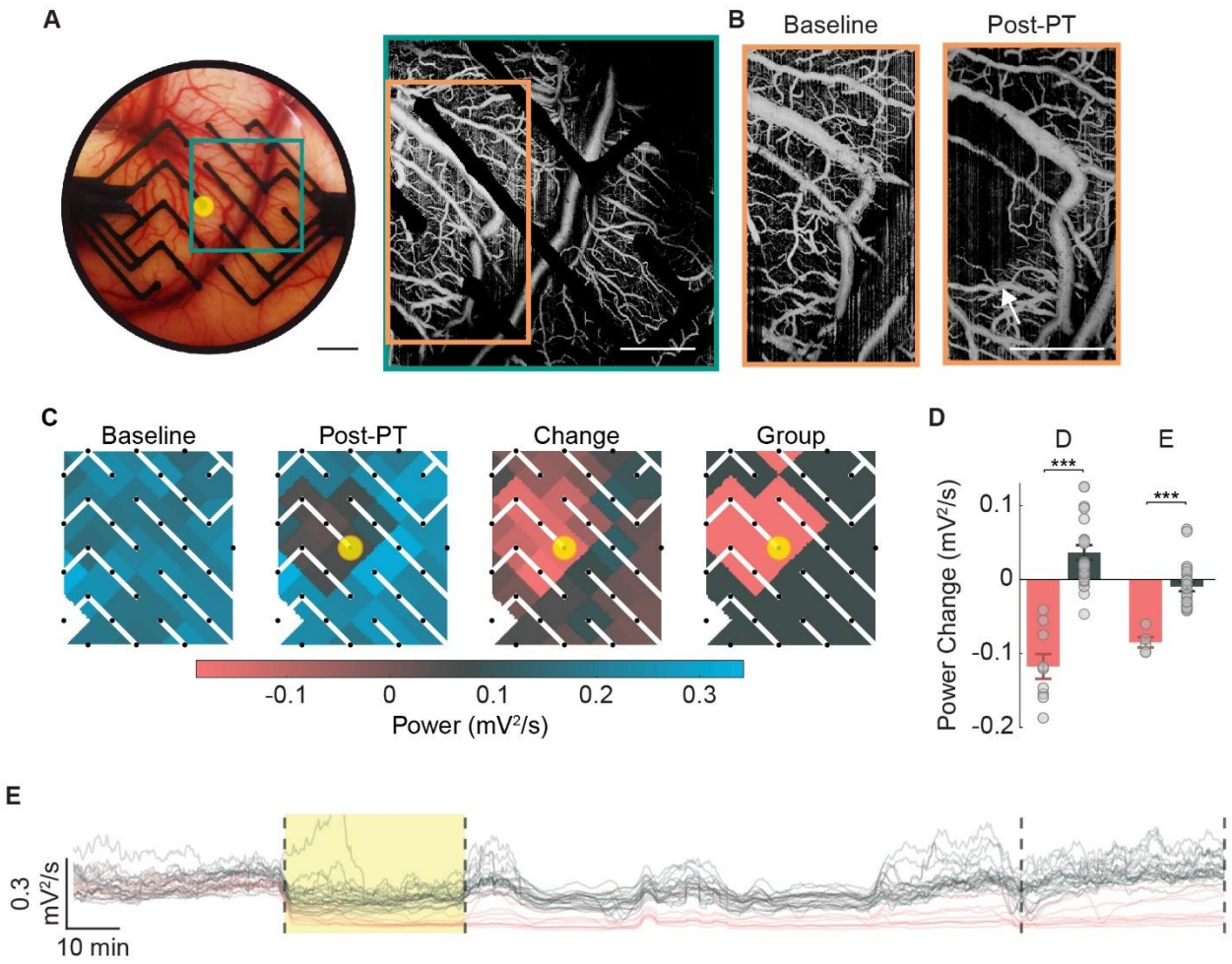

Figure 6. Large-scale electrocorticographic (ECoG) recording of neural activity before, during, and after photothrombotic lesion induction. (A)**,** The transparency of the array enabled OCTA imaging through the array. An example shown here where the area denoted by the green square was imaged in monkey D. Scale bar is 3 mm in the right panel and 2 mm in the left panel. (B)**,** Baseline and 3 hours post-photothrombosis OCTA images demonstrating lesion induction. The lesioned area is indicated by the white arrow. The imaged areas shown are denoted by the orange rectangle in (A). Scale bar is 2 mm. (C) Gamma band power (30-59 Hz) was calculated from 30 minutes of ECoG recording before and 2.5 hours post-photothrombosis for each channel across the array. The change in power was then calculated for each channel. Channels with statistically significant reductions in gamma power were identified (in pink, paired left-tailed t-test, family-wise error rate ≤ 0.001). Yellow circle indicates the location and extent of the aperture for photothrombotic lesion induction. (D) The average change in power for the lesioned group versus the non-lesioned group (error bars denote ± standard error of the mean, SEM; one-way ANOVA, monkey D: p = 5.2e-9, monkey E: p = 1.0e-5). (E) Example of neural recording (gamma power) in monkey D through our ECoG array as the lesions were induced. Illumination period is shown in yellow. The traces are color-coded according to (D) to show the difference between the lesioned and non-lesioned areas.

Electrical Stimulation Enables Modulation of Perilesional Neural Activity

The ability to stimulate neural activity in the same paradigm that allows for cortical lesioning is critical for the development of stimulation-based interventions. Similar to monkeys D and E,

monkeys F and G underwent unilateral photothrombotic lesioning through a 1.5 mm diameter aperture with ECoG recording of activity. We then stimulated through a single perilesional channel in the ECoG array one hour following illumination for a duration of about one hour, after which we continued recording for approximately one hour. Stimulation occurred in six 10-minute blocks separated by 2-minute recording blocks (Figure 7A). To monitor network dynamics following photothrombotic lesioning and during stimulation, we calculated the change in power with respect to baseline in high gamma (60-150 Hz) and theta (4-7 Hz) bands. Here, high gamma and theta bands are used to demonstrate a range of potential frequency bands of interest. Similar to gamma band, high gamma signals are thought to reflect local circuit activity and are associated with movement in sensorimotor cortex (Aoki et al.; Bouyer et al., 1981; Buzsáki and Wang, 2012; MacKay and Mendoncc ą, 1995). We observed an overall decrease in high gamma power across the array throughout stimulation in monkeys F and G. This contrasts with what we observed in non-stimulated monkeys D and E, in which some channels were increasing in high gamma power at equivalent time points (Figure 7B-D). In both stimulated and unstimulated animals, we observed an overall decrease in theta power across the array (Figure 7B-D). Importantly, we demonstrated the ability to electrically stimulate neural activity in the context of our toolbox along with the ability to monitor subsequent effects on network neural dynamics.

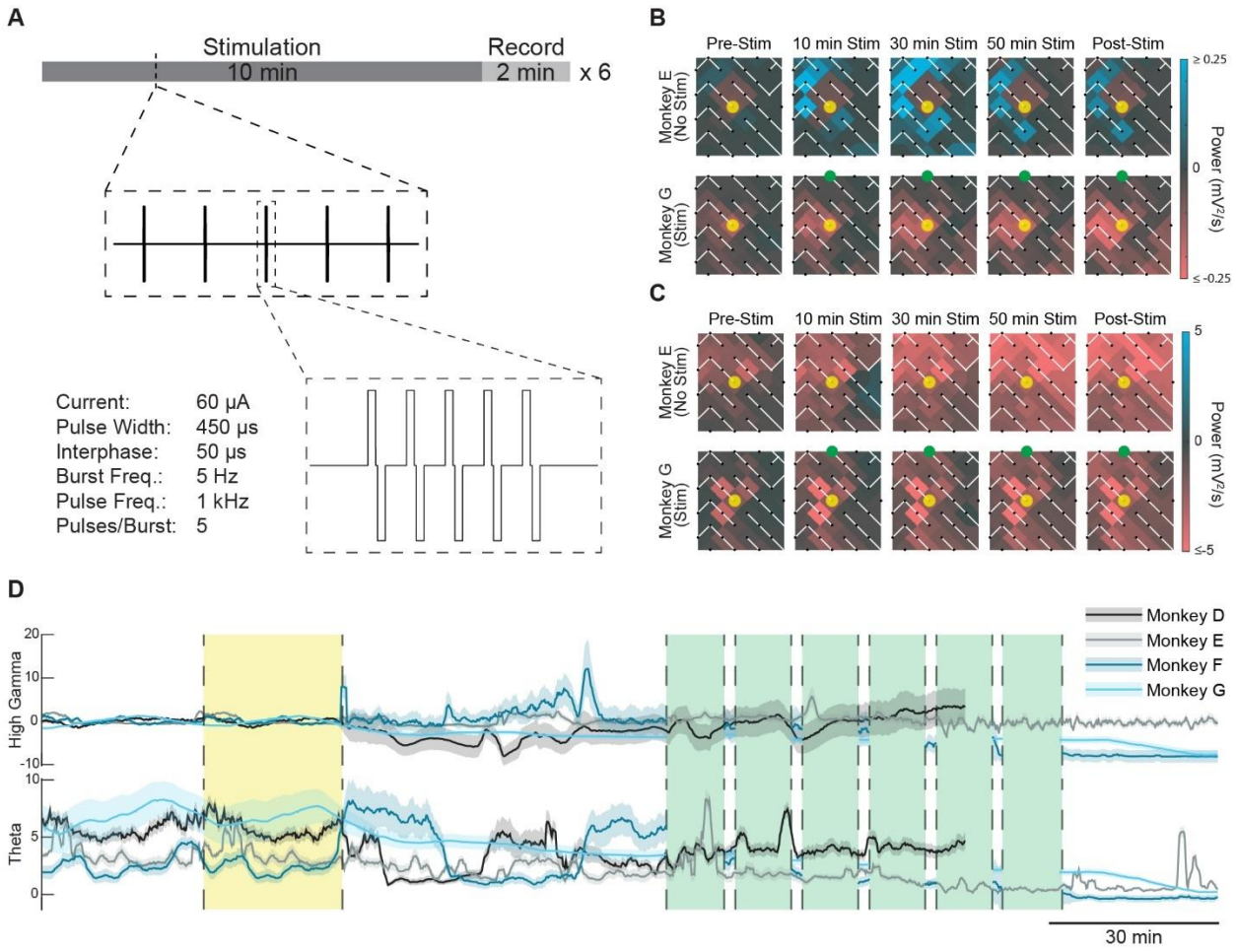

Figure 7. Electrical stimulation enables modulation of peri-lesional neural activity. (A) Stimulation protocol used in this study about one hour after illumination period. Six 10-minute blocks of stimulation were interspaced with 2 min of recording blocks. (B,C) Heat maps of change in high gamma band (B) and theta band (C) power across the ECoG array following blocks of stimulation with respect to baseline for monkeys E (no stimulation) and monkey G (stimulation). Yellow circle indicates the illuminated area and the stimulated channel is indicated by the green node. (D) Average time course of high gamma and theta band power for monkeys D-G. The yellow shaded area indicates the illumination period, while the green shaded areas indicate stimulation blocks for monkeys F and G. Power is normalized to baseline, and the mean power ± 2 x SEM is shown for each animal.

Discussion

The presented toolbox offers significant advantages for investigating critical questions regarding cortical physiology. Here, we demonstrate the photothrombotic technique for inducing focal ischemic lesions in NHP cortex. The extent of subsequent neuronal cell loss was later confirmed histologically. Moreover, we developed a quantitative model for predicting photothrombotic lesion sizes based on illumination parameters. Through this model, lesions can be designed in accordance with experimental needs. We also present OCTA imaging as a tool for observing vascular dynamics

and validating lesion induction *in vivo*. Additionally, our ECoG array allows for the investigation of neural dynamics before, during, and after lesion formation. Critical for developing therapeutic interventions, we also establish the ability to test stimulation-based strategies with our ECoG array. Although not demonstrated here, the toolbox allows for experimentation at clinically relevant time scales when employed in NHPs in contrast to rodent studies.

The photothrombotic technique allows for the induction of targeted focal ischemic lesions in any cortical region of interest. The spatial control of photothrombotic lesion induction is an improvement over other commonly employed models such as middle cerebral artery occlusion models (Sommer, 2017). In addition, the ability to induce consistent smaller, targeted lesions can allow for the induction of lesions to impact specific cortical functions without risking serious injury or mortality compared to middle cerebral artery occlusion (Wu et al., 2016). This capability has been validated in rodents as the photothrombotic technique has enabled the study of local cortical remapping in sensorimotor cortex (Harrison et al., 2013). Larger lesions can also be induced with areas as large as the applied cranial window. Moreover, middle cerebral artery occlusion (Maeda et al., 2005), electrocoagulation (Friel et al., 2007; Nudo et al., 1996; Xerri et al., 1998), and aspiration methods (Padberg et al., 2010) of cortical lesioning require complex surgical intervention and are performed in an invasive manner. In contrast, photothrombotic lesioning only requires optical access to cortex. With the aid of our predictive computational model, lesions can be designed based on experimental needs. However, as is typical with optical techniques, photothrombotic lesion induction with minimal invasiveness is limited to optically accessible regions. To access subcortical areas, more invasive approaches can be used, such as the use of penetrating optical fibers.

Here, we demonstrated the use of OCTA to image large-scale cortical vascular dynamics and to validate the presence of lesions *in vivo* prior to post-mortem histological analysis. The ability to validate lesion induction *in vivo* is critical for long-term NHP studies. We observed strong correlations between OCTA-measured lesion diameters and histologically measured lesion sizes, positioning OCTA as a promising method for reliably measuring lesion sizes *in vivo* without animal sacrifice. Unlike MRI, OCTA imaging enables monitoring of vascular dynamics with greater spatial resolution and without the need for contrast agents, though with limited depth penetration. Moreover, the optical access afforded by our toolbox allows for the use of other optical lesion validation methods, including laser doppler flowmetry (Jiang et al., 2006).

Not all illuminated regions resulted in lesions detected via OCTA imaging or histology. This may be due to the coincidence of those regions with large blood vessels, in which light penetration through smooth muscle and endothelial cell layers and large lumen diameters prevented the complete occlusion of the vessel. Conversely, successful occlusion of a large vessel may induce a larger lesion than expected due to the greater extent of downstream or upstream regions. For example, illumination of a larger vessel resulted in the widest lesion observed across our experiments despite the small aperture of 0.5 mm (Figure 4A, monkey C left hemisphere, Supplementary Figure 4). Therefore, illumination of large vessels should be avoided to ensure successful and predictable lesion induction. Moreover, there was one instance in which a lesion was observed via OCTA imaging but was undetected through histology (Figure 4A, monkey B left hemisphere). This may be due to the superficial nature of the lesion such that it was difficult to detect histologically. In addition, the small size of the lesion may have enabled collateral blood flow to mitigate damage, a phenomenon which has been previously reported in rodent parietal cortex following photothrombotic lesioning of surface vasculature (Schaffer et al., 2006).

We demonstrated the ability to monitor underlying neurophysiological dynamics with the ECoG array before and during the development of a lesion for up to three hours. The combination of OCTA imaging and the semi-transparent ECoG array allows for the induction and validation of photothrombotic lesions, the identification of electrodes corresponding with ischemic areas, and the investigation of network physiology and dynamics. Additionally, OCTA imaging and ECoG recording can be used to investigate neurovascular coupling at higher spatial and temporal resolution than functional MRI (fMRI). However, unlike fMRI which allows for online monitoring of neurovascular coupling, OCTA imaging requires *post hoc* offline analysis. The successful implementation of photothrombotic lesioning and OCTA imaging here, permitted by the transparency of the array, provides evidence for the ability to incorporate other optical techniques such as optogenetics and calcium imaging. Simultaneous ECoG recording and optical coherence tomography in combination with optogenetic stimulation has been previously accomplished in mice (Chin-Hao Chen et al., 2020). The advantageous combination of both techniques is further augmented here by the addition of neurophysiological techniques. We also demonstrated the ability to test electrical stimulation-based interventions as presented here and in a previous publication (Griggs et al., 2021a), in extension of prior post-lesion stimulation studies (Nudo and Milliken, 1996; Nudo et al., 1996). While we demonstrated the use of this toolbox during acute lesioning, these same tools can be implemented for long-term studies in combination with a chronically implanted cranial

window such as our previously published optogenetic interface (Griggs et al., 2019; Khateeb et al., 2019a; Ojemann et al., 2020; Yazdan-Shahmorad et al., 2015, 2016), which exhibits the same spatial scale. In such studies, new lesions can be created or later enlarged without the need for additional surgical intervention, as would be required with the commonly employed electrocoagulation and cortical aspiration methods of focal cortical lesioning.

We also developed a computational model to predict the shape and scale of photothrombotic lesions. Our regression results and Monte Carlo simulation-based results together allow for planning of precise lesions with a variety of illumination parameters, informed by previous literature and validated against our experimental results. Importantly, through our grid search, we identified the optimal optical properties of cortical tissue to accurately predict lesion sizes. It is important to note, in our experiments we did not vary illumination time across different lesions, with an illumination time based on previous photothrombotic studies (Gulati et al., 2015). Therefore, our computational model was constructed based on lesions induced with consistent illumination times. However, our model may be modified in future studies to predict lesions induced with different illumination times to account for differences in total energy that would be delivered to induce Rose Bengal photoactivation. There are also notable assumptions which are applied to our model. First, we assume a consistent gray matter depth at 2.5 mm, whereas in reality, the depth of gray matter is variable across cerebral cortex, which can affect lesion depth predictions. Moreover, the final step of our model involves scaling the profiles from probability maps to better reconstruct the profiles of our histologically detected lesions. This was done to account for the topography of the cortical vasculature (Figure 5B-D). The depth-wise upscaling of our model contours is likely due to the perpendicular orientation of penetrating arterioles and venules relative to the cortical surface (Gould et al., 2017). The diameter-wise downscaling can be ascribed to the redistribution of blood flow in vessels downstream of an occluded vessel to preserve perfusion in these downstream regions (Schaffer et al., 2006), thus potentially reducing the extent of ischemic damage.

Together, these tools can be used to answer critical questions in neuroscience and drive studies of cortical physiology and related disorders such as stroke and traumatic brain injury. Importantly, our toolbox enables the perturbation of the brain and simultaneous monitoring of physiological dynamics over time. The combination of the presented tools can be used to evaluate vascular dynamics, neural dynamics, and neurovascular coupling in the context of either cortical lesioning, stimulation, or both. Like any toolbox, the mutual compatibility of the tools allows for the exclusion

or inclusion of any of the tools described here, depending on the research questions. One main advantage of this toolbox lies in the adaptability and mutual compatibility of this family of tools with each other and other conventional tools in the field. Although our toolbox is demonstrated here in an acute setting, the same tools are capable of implementation in chronic experiments. Previous studies have demonstrated the long-term safety and efficacy of optical windows utilizing an artificial dura for optogenetics, calcium imaging, and other optical tools across various cortical regions (Bollimunta et al., 2021; Chen et al., 2002; Ju et al., 2018; Trautmann et al., 2021; Yazdan-Shahmorad et al., 2016, 2018a). The increasingly widespread use of these optical interfaces makes the presented tools easily integrable with established cranial windows. Such a capability would allow for the monitoring of the behavioral and physiological effects of lesioning and subsequent recovery over time, in combination with testing stimulation-based interventions. Furthermore, the compatibility of our toolbox with optical tools such as optogenetics can enable the comparison of temporary and permanent cortical lesioning techniques. The tools described here can also be adapted for use in smaller organisms such as marmosets and rodents, expanding the utility of this toolbox beyond research groups with access to large NHP animal models. Importantly, long-term studies employing our toolbox can address key questions regarding cortical functions and drive the development of future rehabilitative therapies for stroke, traumatic brain injury, and other relevant neurological disorders.

Limitations of Study

While the presented tools offer great advantages for investigating physiological dynamics in the context of a cortical lesion, there are limitations that can be addressed in later studies. As discussed earlier, the reliance on optical access for lesion induction limits potential regions of interest to superficial brain structures such as cerebral cortex without compromising neural tissue with penetrating optical probes. Additionally, while we developed a model to accurately predict lesion sizes and shapes based on illumination parameters, variations in the induced lesions are likely a result of differences in local optical properties in addition to vascular topographies. Moreover, the ECoG array presented here exhibits limited spatial resolution with 32 opaque electrodes across an area of approximately 314 mm^2 and an electrode pitch on the order of millimeters. With an array with more electrodes in a more compact arrangement, greater spatial resolution can be achieved. Additionally, while the medium in which the electrodes are embedded is transparent, the electrodes themselves are opaque, which can occlude optical penetration of cortical tissue for OCTA imaging

and photothrombotic lesion induction. Such a concern can be addressed through the use of transparent indium tin oxide electrodes (Ledochowitsch et al., 2015). While our current ECoG array limits use to LFP recordings, smaller electrodes would allow for the recording of multi-unit activity as has been previously demonstrated (Khodagholy et al., 2015). Furthermore, the potential to induce chronic post-lesion behavioral effects is not addressed in this study. However, the successes of previous macaque studies (Murata et al., 2008; Padberg et al., 2010) with focal lesions of sizes similar to those reported here provide encouraging evidence of the potential to induce behavioral deficits with the photothrombotic technique. For example, focal lesioning of digit representations in macaque primary motor cortex resulted in impairment of dexterity during grasping tasks. Monkeys that received no post-lesion training moderately recovered after several months (Murata et al., 2008).

Methods

Experimental Model and Subject Details

All experiments were performed in accordance with the Guide for the Care and Use of Laboratory Animals and exceeded the minimum requirements recommended by the Institute of Laboratory Animal Resources and the Association and Accreditation of Laboratory Animal Care International. All animal procedures were approved by the University of Washington Institutional Animal Care and Use Committee. The animals in this study (monkey A: *Macaca mulatta*, 18.45 kg, 14 years, male; monkey B: *Macaca mulatta*, 10.75 kg, 16 years, male; monkey C: *Macaca mulatta*, 10.3 kg, 16 years, female; monkey D: *Macaca nemestrina*, 12.8 kg, 14 years, female; monkey E: *Macaca nemestrina*, 13.10 kg, 14 years, female; monkey F: *Macaca nemestrina*, 13.8 kg, 14 years, female; monkey G: *Macaca nemestrina*, 14.6 kg, 7 years, male) were obtained through the Washington National Primate Research Center (WaNPRC), which is accredited by the American Association for Assessment of Laboratory Care (AAALAC). Animals were housed and maintained in accordance with the guidelines set by the Guide for Care and Use of Laboratory Animals (National Research Council Committee, 2011). Monkeys were fed twice daily with a nutritionally balanced diet of monkey biscuits. The monkeys also participated in the WaNPRC Environmental Enhancement Plan and were provided enrichment items daily. The research in this study was also conducted in accordance with the American Society of Primatologists Principles for the Ethical Treatment of Nonhuman Primates. Animals were housed indoors on a 12-hr light cycle where most monkeys were housed in two-tiered stainless-steel cages in compliance with Animal Welfare Act USDA standards for NHPs based on animal weight. All animal cages were equipped with perches.

Method Details

Surgical Procedure and Photothrombotic Technique

Three adult *Macaca mulatta* (monkeys A, B, and C) were anesthetized with isoflurane and placed in a stereotaxic frame. Throughout the procedure we used standard aseptic technique, and the animals' body temperature, heart rate, electrocardiographic responses, oxygen saturation, and CO_2 end-tidal pressure were monitored. A sagittal or coronal incision was made to expose underlying soft tissue in the right hemisphere of monkey A and bilaterally in monkeys B and C. After removing the soft tissue to reveal the skull, a 25 mm diameter craniotomy targeting the sensorimotor cortex was made based on the macaque brain atlas (Paxinos et al., 2009) with a center 17.5 mm from the midline and 11.55 mm from the interaural line using a trephine in the right hemisphere of monkey A and bilaterally in monkeys B and C. To allow for optical access to the cortical surface, we performed a durotomy to excise the opaque native dura and replaced it with a transparent silicone artificial dura (10:1 Shin-Etsu KE1300-T and CAT-1300) of 0.5 mm thickness and 25 mm diameter. More detailed information on artificial dura fabrication can be found in our previous publications (Griggs et al., 2019; Yazdan-Shahmorad et al., 2016). We acquired baseline OCTA images of the exposed cortical surface through the artificial dura as described later in a later section. Light exposure was limited across the cortical surface by placing on the artificial dura an opaque silicone mask with circular apertures with diameters of 0.5, 1.0, and 2.0 mm distributed across the mask (Figure 1A). We then intravenously injected 20 mg/kg of Rose Bengal solution (40 mg/mL concentration) through the saphenous vein over the course of 5 minutes and began illumination through the mask with a cold white light source for 30 minutes (Figure 1B). To prevent further light exposure following illumination, the cranial window was optically shielded until OCTA images were acquired 3 hours post-illumination. Following post-illumination OCTA imaging, we perfused the animal with 6 L of 4% paraformaldehyde then extracted and immersed the brain in 4% paraformaldehyde solution for 24–48 hours at 4 °C.

Electrocorticographic Recording, Stimulation, and Power Analysis

Electrocorticographic Recording

Four adult *Macaca nemestrina* (monkeys D, E, F, and G) underwent a surgical procedure similar to that of monkeys A, B, and C. Briefly, bilateral craniotomies and durotomies were performed targeting the sensorimotor cortex following sedation and stereotaxic positioning. After baseline OCTA images were acquired through the transparent silicone artificial dura (monkeys D-E), the artificial dura was removed and replaced with a semi-transparent ECoG array of 32 electrodes (Figure 4A).

Approximately 30 minutes prior to the beginning of baseline recording, animals were transitioned from isoflurane to urethane anesthesia to enable for recording of neural activity. To correlate electrode location with lesion location, OCTA images were acquired prior to photothrombosis through the array for monkey D (Figure 4A). We placed an opaque mask similar to that of monkeys A through C but with a single aperture located in the center with a diameter of 1.5 mm on the ipsilesional hemisphere (monkeys D, F, and G: left hemisphere; monkey E: right hemisphere). In the contralesional hemisphere we placed a mask without any apertures. A skull screw located anterior and medial to the ipsilesional cranial window was used as a ground for ECoG recordings. Prior to Rose Bengal infusion and illumination as described previously, baseline ECoG recordings were collected bilaterally for 30 minutes. We also recorded LFPs during illumination and for 3 hours following illumination. We then acquired OCTA images in both hemispheres (monkeys D-E), perfused the animals, and stored the extracted brain as described previously.

Electrocorticographic Stimulation

One hour following illumination, we stimulated perilesionally through one channel for a duration of about one hour in monkeys F and G. Stimulation (60 μA, 5 biphasic pulses per burst at 1 kHz, 450 μs pulse width, 50 μs interphase interval, 5 Hz burst frequency) occurred in six ten-minute blocks interspaced with 2-minute recording blocks. Post-stimulation recording was then continued for another 30-60 minutes.

Power Analysis

LFPs were recorded at a rate of 30 kHz and downsampled to 1 kHz in MATLAB for power analysis. Signals were notch filtered at 60, 120, 180, and 240 Hz, and were bandpass filtered to isolate theta (4-7 Hz), gamma (30-59 Hz), and high gamma (60-150 Hz) bands. After filtering, artifacts were removed from the signal by normalizing the discrete time series of each signal, and samples with an amplitude exceeding 25 standard deviations were identified and excluded from analysis. Similarly, channels with power spectral densities that did not exhibit the expected $1/f^{\alpha}$ curve were also excluded from analysis. Thus, one channel was excluded from analysis in monkey D, three channels were excluded from analysis for monkey E, and 11 channels were excluded from analysis for monkey F. No channels were excluded for monkey G. The signal power for each frequency band was calculated for each electrode over the course of the baseline and the final 30 minutes of post-illumination recording periods. Signal power was calculated by squaring the filtered signal and dividing by the elapsed time. Change in signal power was calculated by subtracting mean baseline power from the mean post-illumination power. To isolate channels with decreasing power, we

performed a left-tailed paired t-test between the 30 minutes of baseline power and the final 30 minutes of post-illumination power calculated at 60 s intervals (family-wise error rate ≤ 0.001 to account for multiple comparisons). Thus, we categorized channels in a lesioned group (decreasing power), and a non-lesioned group (failed to show a decrease in power). A one-way ANOVA was used to compare average change in power of channels across the two groups at a significance level of 0.05. The time-varying signal power across all recording periods was calculated in 10 s intervals and smoothed (smoothing factor of 0.4-0.5). To observe the effects of electrical stimulation over time, the power time-course for each individual channel was normalized to baseline mean and standard deviation.

Histology and Immunohistochemistry

After 24-48 hours of post-fixation in 4% paraformaldehyde brains of all animals were dissected into a single 25 mm thick coronal block containing the region of interest using a custom matrix and stored in 30% sucrose in PBS solution at 4 °C for a minimum of one week. The block was then frozen and sectioned into 50 µm coronal sections using a cryostat (Microm, Thermo Fisher) or a sliding microtome (Leica). Cut sections were stored in PBS solution with 0.02% sodium azide at 4 °C. To evaluate the extent of ischemic damage to the neuronal population we first performed Nissl staining on mounted serial coronal sections with a rostrocaudal separation of approximately 0.45 mm using Cresyl Violet (monkeys A and B) or Thionin acetate (monkeys C, D, and E). Due to inadequate storage conditions resulting in loss of tissue, not all putative lesions were confirmed histologically for monkey A. Therefore, data from monkey A was excluded from the rest of our analysis. To additionally confirm the neuronal cell loss in the illuminated regions, we immunostained adjacent sections for a selective neuronal marker NeuN. Sections were further trimmed to include the mediodorsal part of the hemisphere with putative lesion sites; these were first incubated in 50% alcohol for 20 min to permeabilize, then rinsed in PBS and incubated in 10% normal donkey serum in PBS containing 0.1% triton-X100 at 4 °C for 1-2 hours, and then incubated with a mouse anti-NeuN primary antibody (1:500, Millipore Sigma; MAB377, RRID: AB_2298772) at 4 °C for 48 hours. Sections were then rinsed in PBS, incubated in 2% normal donkey serum followed by the secondary donkey anti-mouse antibody conjugated to AlexaFluor 488 (1:300, Millipore) for 4-6 hours at room temperature. Sections were rinsed and mounted using VectaShield mounting media (Vector) containing DAPI and imaged using Nikon 6D widefield automated microscope system (Nikon imaging Center at UCSF).

Lesion Reconstruction and Size Measurement

All Nissl-stained slices for monkeys B through E were imaged and co-registered in MATLAB (MATLAB R2020a, MathWorks) without resizing. The registered images were then edited in Adobe Photoshop to enhance boundaries between infarct and non-infarcted regions, after which each slice was smoothed with an edge-preserving filter, binarized, and underwent edge-detection to identify slice boundaries with and without the infarcted regions in MATLAB (Figure 2D,E). Lesion boundaries were obtained by subtracting boundaries with the lesions from boundaries that excluded the lesions. These boundaries were then visualized as surfaces in three-dimensional space with linear interpolation of the approximately 0.45 mm rostrocaudal separation between slices. The average diameter and maximum depth from representative coronal slices of each lesion were then calculated based on image resolution.

Optical Coherence Tomography Angiography Imaging

For *in vivo* validation of disrupted blood flow in cortical vasculature, we acquired OCTA images for monkeys B through E. OCTA was acquired from a custom-built prototype OCT system, using a 200 kHz vertical cavity surface-emitting swept source (SL1310V1-10048, Thorlabs Inc., Newton, NJ) with a central wavelength of 1310 nm, and a sweeping bandwidth of 100 nm, giving an axial resolution of ~8 μm in tissue (~11 μm in air). The prototype was similar to the device reported in a previous publication (Deegan et al., 2018b, 2021; Xu et al., 2017). Briefly, the imaging probe was a hand-held piece in which a paired X-Y galvo scanner and sample optics assembly were housed. To facilitate scanning, a monitoring screen was integrated with the hand-held probe where the OCT and OCTA cross-sectional images are displayed in real time to aid the operator during imaging. In this study, the probe was mounted on an articulated arm to maintain a consistent distance between the objective lens and the imaging target. A 5X objective lens within the hand-held probe focused the 1310 nm light source into a beam spot on the brain surface with an incident power of 5 mW, similar to that of a common laser pointer. Alongside the imaging light was a visible laser beam, which was used to guide OCTA imaging, which also provided an opportunity to position and orientate the beam spot over the same tissue region for each scan session, producing reliable and repeatable scans over different time points.

OCTA was performed in repeated raster-scan. The scanning beam was directed into the cortical tissue through a transparent silicone artificial dura, prior to photothrombosis and 3 hours post-illumination with a lateral FOV of approximately 9 mm x 9 mm. At each position on the raster scan, one full A-scan approximately 8 mm deep (1408-sampling-pixel) was acquired. Each B-frame

contained 1000 A-line scans and was repeated 8 times, then moved to the next B-frame. This process was repeated to form a volume of 1408 x 1000 A-lines x 8 repeat x 1000 B-frames. The optimal resolution in the axial direction (into the tissue) was 5.5 μm and the lateral resolution was 24 μm. The volume scan was repeated at different regions within the cranial window, then processed to form a 3D OCTA data set. For visualization, the 3D OCTA was color-coded with the depth associated with each vessel into a 2D-en-face (top-down) projection.

The 2D-en-face projections at different regions were then stitched together to form a larger FOV as in Figure 3 using the Hugin software (Hugin-2019.2.0). Stitched OCTA images were then aligned with images of the cortical surface via control point registration in MATLAB. To estimate the diameters of the lesions, images were first smoothed with a Gaussian filter and binarized. Lesion boundaries of each detected lesion were fitted with ellipses and the major and minor axis lengths were recorded. The major axis lengths were then defined as OCTA-measured lesion diameters. Illuminated regions outside the FOV excluded from analysis.

Light Intensity Measurements

Due to the uncollimated nature of the illuminating light beam, the power density of the light through each aperture was assumed to differ based on the location and diameter of each aperture. We measured the light intensity (535 nm) through each aperture (10-20 times) and through the mask without any apertures using a photodetector (Thorlabs PM100D Power Meter and S121C Sensor).

Lesion Size and Illumination Parameter Analysis

The relationship between OCTA-measured lesion diameter and histologically measured lesion diameter was assessed by fitting an ordinary least squares linear regression in MATLAB (fitlm function). Similarly, the relationships between OCTA-measured diameter and histological lesion depth, as well as histological depth and diameter were analyzed by ordinary least squares regression. We also computed the partial correlation coefficients between the illumination parameters (aperture diameter and log-transformed light intensity) and each lesion size metric (OCTA-measured diameter, histological diameter, and histological depth) separately in MATLAB (partialcorri function). We computed partial correlation instead of Pearson's correlation to separate the individual contributions of the illumination variables. We log-transformed the light intensity values before calculating the correlations in accordance with the Beer-Lambert law (Bouguer, 1729), which relates optical path length to the logarithm of light intensity.

Light Simulation

Our computational model of light penetration and subsequent lesion in the brain consisted of a Monte Carlo simulation of photons propagating through brain tissue, extraction of a light intensity contour, and scaling of the contour. A virtual volume was constructed which mimicked the experimental setup and had the relevant optical properties of brain tissue. Photons were virtually propagated through this volume to obtain a probability distribution of photon fluence, or light energy passing through a given area. Optical parameters were informed by published literature regarding primate cortical optical properties and then refined to maximally match our experimental results obtained through histology. The Monte Carlo simulations were designed using the Monte Carlo eXtreme (MCX) software (Fang and Boas, 2009) and run on discrete graphics cards (Nvidia GTX 1080Ti and Nvidia GTX 2060).

The virtual volume consisted of a light source and mask, an artificial dura, and gray and white matter (Figure 5A). The entire volume was 8 mm x 8 mm x 5.6 mm (width x width x height), with voxel resolution of 0.01 mm^3. We specified the light source as a disk parallel to the surface of the brain with collimated light exiting the side of the disk facing the brain, and then passing through a thin highly scattering disk which uncollimated the light. We set the diameters of both disks to be equal to the aperture diameter of the mask of the corresponding *in vivo* experiment. We specified the volume peripheral to the disks as a highly absorbing and highly scattering medium to mimic the opacity of the non-aperture part of the mask (Supplementary Table 1). The diameter used in our simulations were 0.5 mm, 1 mm, 1.5 mm, and 2 mm, corresponding with the apertures tested in our *in vivo* experiments. After specifying the volumes, we ran simulations of 1 million photons through the volume. The simulations yielded voxel-wise fluence values, or values of radiant energy received per unit area. The fluence results were imported into MATLAB and analyzed with custom code.

Research on the optical properties of gray matter is often contradictory, and values of index of refraction, anisotropy coefficient, and absorption and scattering coefficients vary by orders of magnitude in published research. We defined a grid search boundary of optical properties by using the values reported in previous literature (Gottschalk, 1992; Yaroslavsky et al., 2002) as upper and lower bounds of the properties. As the absorption spectrum for Rose Bengal peaks at 559 nm, we used the optical properties reported for this wavelength by interpolating from nearest reported wavelengths. The range of the grid was [0.03, 0.76] mm^{-1} for gray matter absorption, [9.9, 53.6] mm^{-1} for gray matter scattering, [0.09, 0.36] mm^{-1} for white matter absorption, and [41.9, 78.4] mm^{-1} for

white matter scattering. For anisotropy coefficients the two publications reported similar values, therefore we averaged the values between the publications to obtain an anisotropy coefficient of 0.92 for gray matter and 0.8 for white matter. The refractive index was set as 1.36 for gray matter and 1.38 for white matter (Yaroslavsky et al., 2002). From the optical property ranges we constructed a 5 x 5 x 4 x 4 size grid with 5 values for the gray matter absorption and scattering coefficients and 4 values for the white matter absorption and scattering coefficients. For each of the 400 combinations of parameters, four simulations were run, corresponding with the four aperture sizes tested in our experiments. Each simulation yielded a volumetric fluence distribution. We further obtained representative 2D central slices to compare with histologically obtained lesions.

For each photon intensity distribution corresponding to an optical property combination, we identified the light intensity threshold which yielded contours most closely matching those obtained from central slices of lesions obtained from histology. By treating the maximum depth and average width of an individual contour as the prediction of maximum depth and average width of the corresponding lesion, we quantified the predictive power of the simulation. Denote by SSR_d the residual sum of squares of prediction of maximum depth of a lesion, SST_d the total sum of squares of maximum depth of a lesion, SSR_w the residual sum of squares of prediction of average width of a lesion, and SST_w the total sum of squares of average width of a lesion. The objective function used to find the best light intensity threshold was:

$$\min_{\text{thresh}}\left(\frac{{SSR_d}^2}{{SST_d}^2}+\frac{{SSR_w}^2}{{SST_w}^2}\right). \qquad (1)$$

This is equivalent to maximizing the (squared or unsquared) Euclidean norm of the r-squared values of depth and width predictions less 1. Denote by r_d^2 the r-squared value of the simulation-based prediction of maximum depth of a lesion, and r_w^2 the r-squared value of the simulation-based prediction of average width of a lesion. Then the equation above can be rewritten as:

$$\max_{\text{thresh}}\left((r_d^2-1)^2+(r_w^2-1)^2\right). \qquad (2)$$

We solved this objective function individually for each optical property combination using Bayesian optimization. We then identified the simulation yielding the minimum value of this objective function as that most closely matching our histology data and used the results of that simulation for all later parts of the analysis. The optical properties of this best simulation were gray matter absorption

coefficient of 0.395 mm^{-1}, gray matter scattering coefficient of 53.6 mm^{-1}, white matter absorption coefficient of 0.09 mm^{-1}, white matter scattering coefficient of 54.066 mm^{-1}, and a light intensity threshold for lesion induction of 19.9 $\mu W/mm^2$.

We then identified a transformation to accurately scale the profiles of the light simulation contours to that of the lesions obtained from histology (Figure 5C,D). We opted to do this by independently scaling the width and depth of the contours. Our first approach was to fit a univariate linear regression from the simulation depths and widths to the lesion depths and widths, respectively. In this linear regression we did not allow an intercept term. Based on the results of our linear regressions, we further evaluated the need for non-linear transformations. Once these scaling factors were set, we treated them as the final stage of our modeling platform, whereby light intensity contours from the Monte Carlo would be stretched and shrunk accordingly to transform from the light profile to the lesion profile.

Supplemental Information

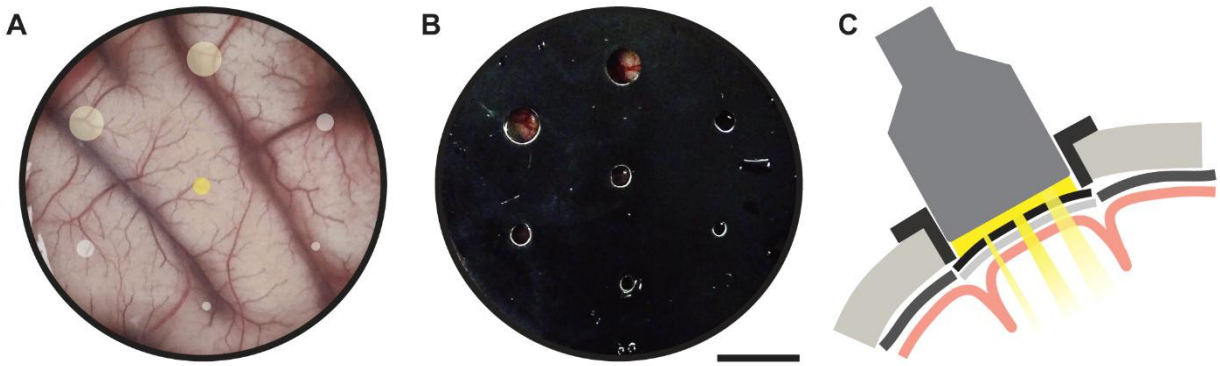

Supplementary Figure 1. Schematic of illumination using a multi-apertured mask used for monkeys A, B, and C. Related to Figure 1. (A) A cranial window through an artificial dura with projected areas of illumination shown in yellow. (B) Multi-apertured mask is placed on top of the artificial dura. (C) Coronal schematic of illumination through the apertured mask. This setup enables testing different illumination intensities and aperture diameters.

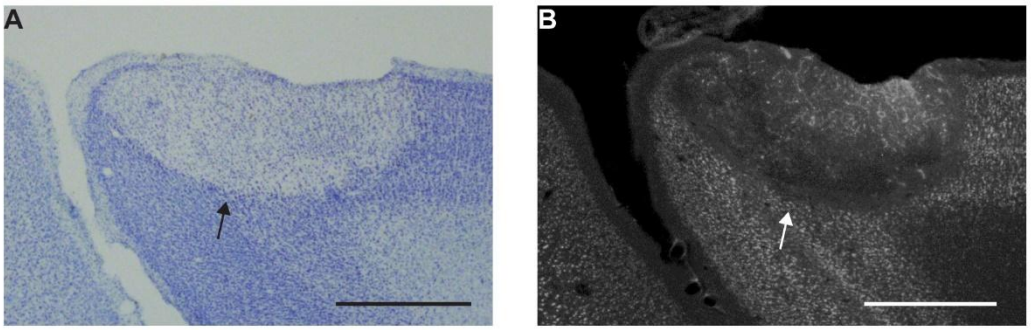

Supplementary Figure 2. Validation of neuronal cell loss with NeuN staining. Related to Figure 2. (A) Nissl staining demonstrating cell loss indicated by the black arrow in a representative coronal slice from monkey C. (B) NeuN staining of an adjacent slice demonstrating neuronal cell loss in the same lesion indicated by the white arrow. Scale bars are 1 mm.

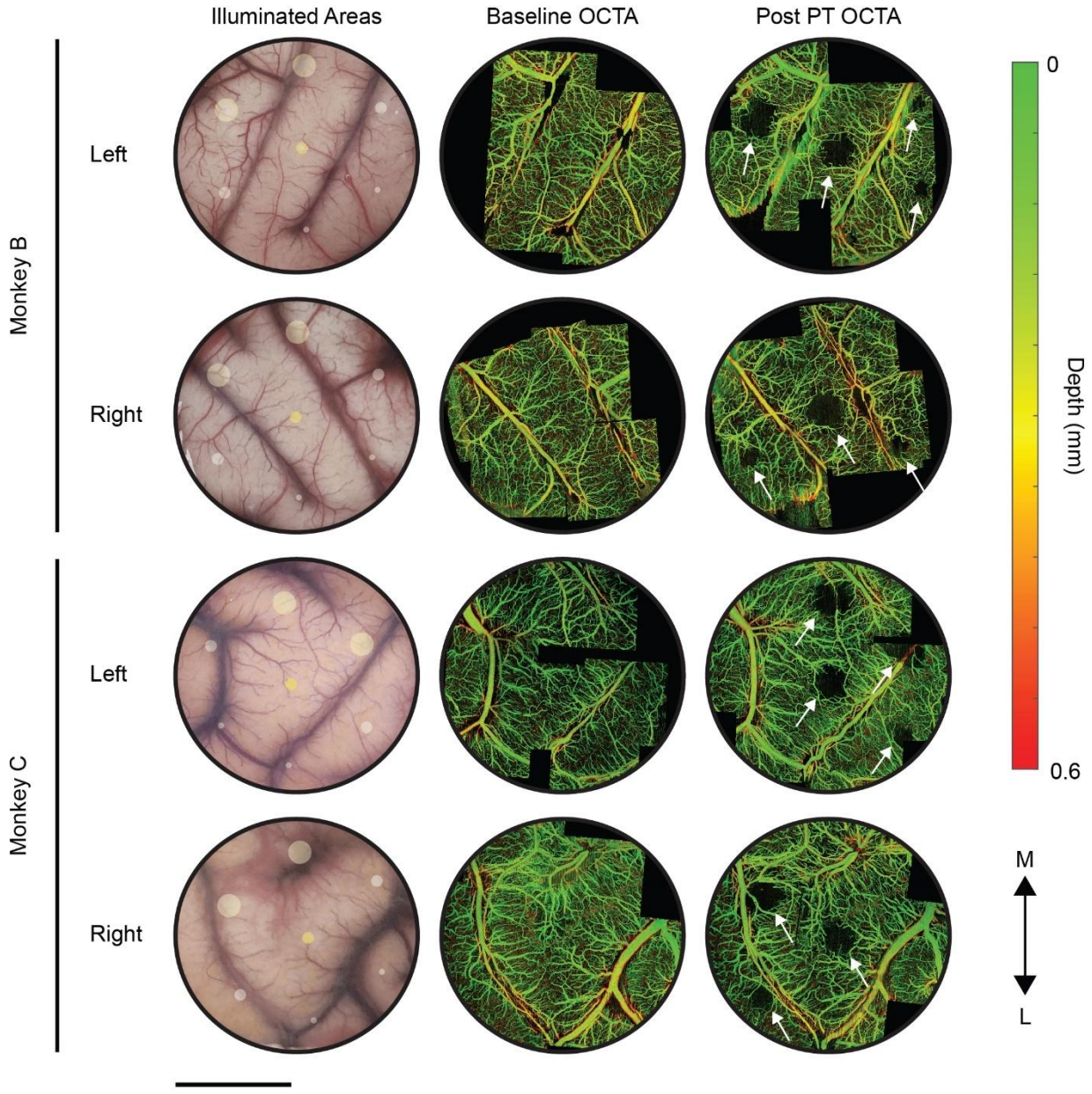

Supplementary Figure 3. Optical coherence tomography angiography (OCTA) imaging was used to validate lesion induction *in vivo*. Related to Figure 3. Stitched baseline and post-photothrombosis OCTA images are shown for both hemispheres of monkeys B and C, with vasculature color indicating cortical depth. In the left column, yellow circles indicate the illuminated regions for photothrombosis, with the diameters corresponding with the aperture diameters. Shading of the yellow circles in the left column indicate relative intensity of illumination. Baseline OCTA images are shown in the middle column. In the right column, dark regions indicated by white arrows in OCTA images taken 3 hours after photothrombosis indicate successful lesion induction due to the occlusion of the illuminated microvasculature. Scale bar is 1 cm.

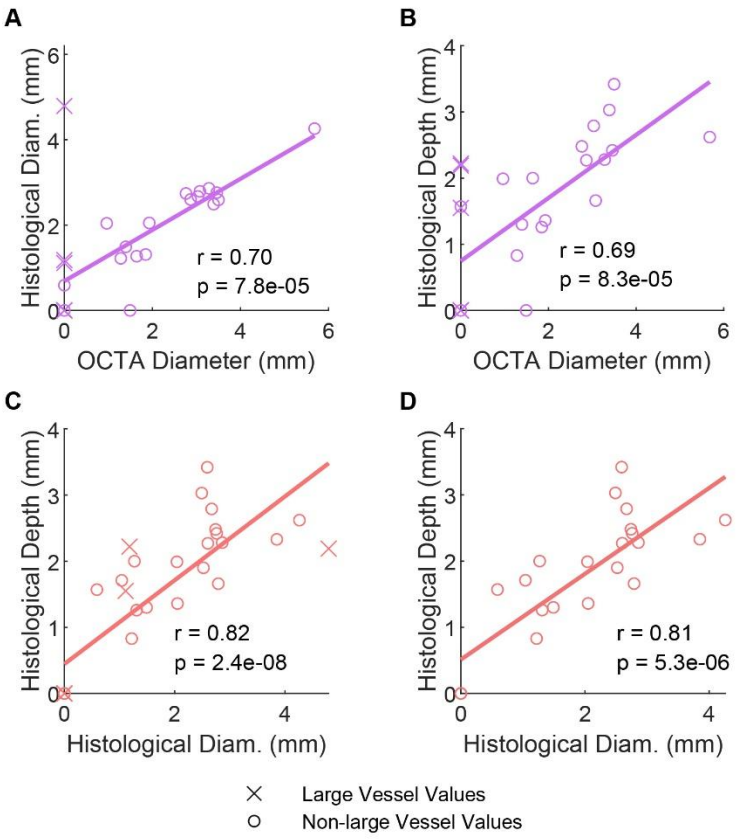

Supplementary Figure 4. OCTA predictions of histologically measured lesion size with large vessel values included. Related to Figure 4. (A) Correlation between OCTA- and histologically measured lesion diameters (r = 0.70, p = 7.8e-5). (B) Correlation between OCTA-measured lesion diameters and histologically measured lesion depths (r = 0.69, p = 8.3e-5). (C,D) Correlation between histologically measured lesion diameters and depths with large vessel values included (C, r = 0.82, p = 2.4e-8), and excluded (D, r = 0.81, p = 5.3e-6).

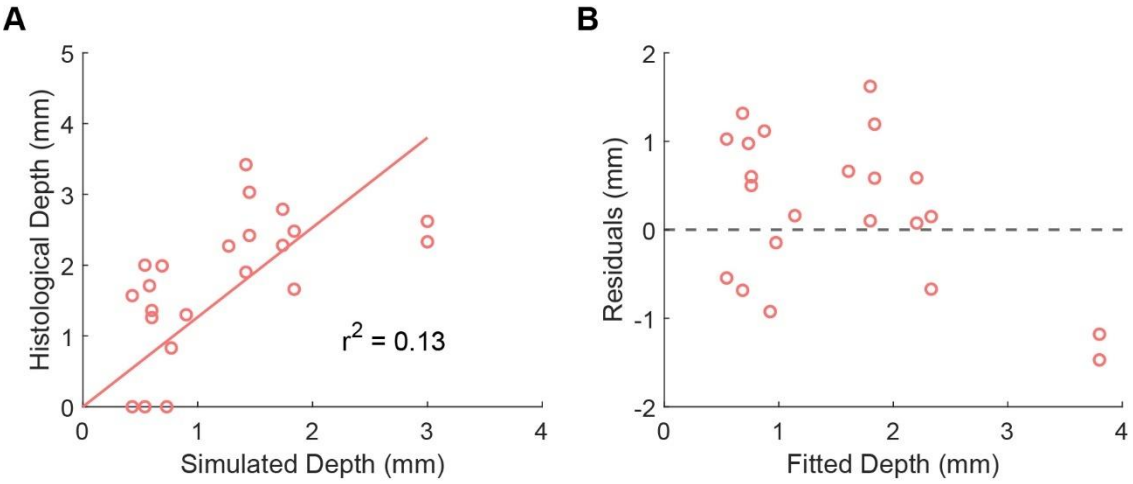

Supplementary Figure 5. Transformation of simulated depths in second stage of modeling photothrombotic lesions. Related to Figure 5. (A) Histological depths vs linearly transformed simulated

depths. (B) Residuals of histological depths vs linearly transformed simulated depths plotted against fitted values from (A).

	μ_a (mm^{-1})	μ_s (mm^{-1})	g (anisotropy)	n (index of refraction)	Thickness (mm)
Scattering disk	0	100	0.86	1.44	0.1
Mask (opaque)	1000	1000	1	1.3	0.1
Artificial dura	0.01	0.01	0.86	1.43	0.5
Gray matter	0.395	53.6	0.91	1.36	2.5
White matter	0.09	54.066	0.8	1.38	2.5

Supplementary Table 1. Table of optical properties and thicknesses of virtual media used in the Monte Carlo simulation. Related to Figure 5.

Chapter 3: Homeostatic priming facilitates Hebbian-based network functional connectivity change in non-human primate cortex

Karam Khateeb, Felix Schwock, Noah Stanis, Jasmine Zhou, Tiphaine Belloir, Azadeh Yazdan-Shahmorad

Abstract

The ability to alter the connections between the neurons in our brains is fundamental for our survival. When injuries or disorders of the nervous system result in disrupted connectivity, one clinical approach is to restructure neural connectivity to restore any lost behaviors or functions of the nervous system. The most common strategies utilize principles of Hebbian plasticity, wherein the coactivation of neurons results in a strengthening of the connections between them. Hebbian-based approaches, however, suffer from a lack of efficacy *in vivo*. Homeostatic metaplasticity is a mechanism by which the recent activity of neurons determines their likelihood to strengthen or weaken their connections. Metaplasticity mechanisms constantly operate in tandem with Hebbian plasticity mechanisms and are often overlooked in developing plasticity-based treatments. We hypothesized that homeostatic priming of cortical neurons by suppressing neuronal activity will lead to greater strengthening of connectivity when followed by Hebbian-informed paired stimulation compared to paired stimulation alone. We tested this in posterior parietal cortex of two macaques by repeatedly suppressing neural activity optogenetically for a period of 10 minutes then conducted a Hebbian-informed paired electrical stimulation protocol between two cortical sites. Homeostatic priming prior to Hebbian-informed paired stimulation resulted in an increase in functional connectivity between stimulation pairs and across the network. Functional connectivity changes also became less predictable and less reliant on the underlying network. Finally, graphical diffusion autoregressive (GDAR) flow analysis showed that paired stimulation alone facilitated a preferential increase in information flow around each stimulation site in the direction of the opposing paired stimulation site. Homeostatic priming prior to stimulation promoted orientation-independent changes in information flow between stimulation sites and neighboring regions, representing a potential mechanism by which overall network functional connectivity changes can occur. Together, these results demonstrate the potential for integrating homeostatic metaplasticity and Hebbian plasticity principles in designing stimulation-based therapies that aim to rewire cortical circuitry for neurorehabilitative applications.

Introduction

Neurological disorders such as stroke, traumatic brain injury, and epilepsy often result in the disruption of neural connections that can cause serious cognitive and behavioral deficits. Fortunately, neurons possess the remarkable ability to alter their connectivity, a process that is crucial for human development and survival and is thought to underly memory formation and learning. We explored an approach towards treating neurological disorders such as stroke that utilizes these innate mechanisms of synaptic plasticity to reinforce existing connections to drive functional recovery (Cramer, 2018; Edwardson et al., 2013; Grefkes and Ward, 2014).

The predominant mechanism of synaptic plasticity targeted in neural rewiring strategies is Hebbian plasticity, which hypothesizes that repeated coincidental activity between two neurons results in their strengthened connectivity (Hebb, 1949). One mechanism of Hebbian plasticity, first demonstrated *in vitro* and *ex vivo* (Bi and Poo, 1998; Markram et al., 1997), is spike timing-dependent plasticity (STDP). According to the now canonical STDP principles, repeated firing of a presynaptic neuron that is immediately followed by the firing of a postsynaptic neuron will strengthen the synapses between them (long-term potentiation, LTP) (Bi and Poo, 1998; Feldman, 2012). One advantage of STDP-based approaches is the ability to direct plastic connectivity changes through paired stimulation of two neurons or groups of neurons. Groundbreaking work in NHPs demonstrated the validity of STDP principles *in vivo* through activity-dependent and paired neural stimulation, highlighting the potential for clinical translation (Edwardson et al., 2013, 2014; Jackson et al., 2006; Lucas and Fetz, 2013; Seeman et al., 2017; Yazdan-Shahmorad et al., 2018a). However, there remain significant flaws with these approaches that have contributed to their limited efficacy (Bloch et al., 2019; Feldman, 2012; Seeman et al., 2017; Ting et al., 2020). Namely, paired stimulation paradigms fail to consider other factors shaping synaptic plasticity *in vivo* (Feldman, 2012). Recent studies have demonstrated that the underlying network holds greater influence on functional connectivity change compared to stimulation protocols (Bloch et al., 2022, 2019). The role of the spike-timing aspect of plasticity is only a small part among a multitude of other important factors (Bloch et al., 2022, 2019; Feldman, 2012).

One feature often overlooked in STDP-based approaches is the homeostatic tendency of neurons to maintain consistent levels of activity by altering synaptic strengths and modifying the threshold for LTP induction. This is unlike Hebbian plasticity, in which correlated activity results in LTP, leading to further correlated activity and subsequent LTP. Additionally, increased synaptic potentiation and

postsynaptic excitatory drive facilitates potentiation of other previously weaker synapses, obfuscating the input specificity of synaptic inputs encoded by the diversity of synaptic strengths. Such positive feedback loops can therefore lead to circuit instability (Turrigiano and Nelson, 2000). Consequently, both Hebbian and homeostatic plasticity mechanisms are continuously ongoing processes in cortical circuits. Therefore, in developing Hebbian-based stimulation therapies for the treatment of neurological disorders, homeostatic plasticity mechanisms must also be considered to improve treatment efficacy. In this study, we explored one strategy with which both Hebbian and homeostatic plasticity mechanisms may be reconciled and leveraged to improve the efficacy of stimulation-based therapies. One proposed mechanism of homeostatic plasticity is the sliding threshold mechanism, also termed homeostatic metaplasticity (Bear et al., 1987; Bienenstock et al., 1982; Cooper and Bear, 2012; Lee and Kirkwood, 2019). According to this hypothesis, recent neuronal activity levels alter the threshold for LTP induction. Neurons with decreased activity exhibit a decreased threshold for LTP induction, while neurons with increased activity have an increased threshold for LTP induction. This model of homeostatic plasticity has been previously demonstrated *ex vivo* in pharmacological inhibition studies and *in vivo* in studies where sensory deprivation results in upscaling of synaptic weights (Kirkwood et al., 1995, 1996; Kotak et al., 2005; O'Brien et al., 1998). However, not all sensory deprivation studies have been successful at demonstrating reduced thresholds for LTP following neuronal inhibition (Lee and Kirkwood, 2019; Whitt et al., 2014). Different sensory deprivation techniques *in vivo* yield different results likely due to differences in the mechanisms of sensory deprivation and their efficacy of neuronal inhibition (Lee and Kirkwood, 2019; Whitt et al., 2014). Thus, whether attempts to engage metaplastic mechanisms *in vivo* or in a clinical setting can be effective has been uncertain. In this study, we set out to explore whether homeostatic priming periods of pan-neuronal inhibition can aid in the facilitation of Hebbian functional connectivity change in the clinically relevant NHP animal model.

A series of investigations in motor cortex provide evidence of homeostatic metaplasticity expression in humans, some even demonstrating promising effects of homeostatic priming on motor learning and excitability (Edwardson et al., 2013; Iyer et al., 2003; Karabanov et al., 2015; Lang et al., 2004; Müller et al., 2007; Pötter-Nerger et al., 2009; Siebner et al., 2004). However, the demonstration of effective stimulation-induced corticocortical connectivity change has yet to be convincing in human studies (Doeltgen and Ridding, 2011; Fricke et al., 2011). Due to the technological limitations of research in humans, the methods used in these studies (i.e., repetitive transcranial magnetic stimulation, transcranial direct current stimulation, median nerve stimulation) lack the

spatiotemporal specificity of neuronal manipulation and recording needed to effectively assess such an approach. Specifically, while these approaches have demonstrated the success of homeostatic priming in raising excitability in corticospinal circuits, such efficacy in corticocortical connections has remained elusive (Doeltgen and Ridding, 2011; Fricke et al., 2011; Karabanov et al., 2015; Lang et al., 2004; Siebner et al., 2004). With recent developments in large-scale optogenetic neural interfaces in NHPs, we were able to investigate the simultaneous engagement of metaplastic and Hebbian mechanisms at the level of local corticocortical circuits. We hypothesized that homeostatic priming via neuronal inhibition preceding periods of Hebbian-inspired paired stimulation would correspond with greater functional connectivity changes compared to non-primed paired stimulation periods.

Results

We investigated the effects of periods of pan-neuronal optogenetic-mediated inhibition on succeeding periods of Hebbian-informed paired electrical stimulation in the posterior parietal cortex. We utilized an optogenetic interface previously developed and implanted in posterior parietal cortex of two adult male rhesus macaques (monkey H, age 10; monkey L, age 10-11) (Griggs et al., 2024). The interface consisted of a chronically implanted semi-transparent 32-channel electrocorticographic (ECoG) array that spans a 25 mm diameter cranial window (Figure 1A). Previously, the animals were injected with AAV8-hSyn-Jaws-GFP to pan-neuronally express the red-shifted inhibitory opsin Jaws. Epifluorescence imaging of the GFP tag within the cranial window allowed for validation of expression and the identification of expressing regions (Figure 1A). The animals were head-fixed in a primate chair throughout data collection. Within each experimental block, the initial 10 min period consisted of spontaneous recordings of surface local field potentials (LFPs) obtained through the ECoG array. The second 10 min period was characterized by a sham priming period or a priming period in which red light was pulsed through a micro-LED array for 900 ms pulses at a 50% duty cycle. The following 10 min period consisted of Hebbian-informed paired electrical stimulation of two randomly selected cortical sites within expressing regions at 5 Hz burst frequency with a 10 ms delay between stimulation sites. We also tested blocks with sham stimulation during this period. The final 10 min period of each block entailed recording spontaneous surface LFPs for later comparisons with the initial baseline period (Figure 1B). Overall, four experimental conditions were tested across both animals: unconditioned (30 blocks), priming only

(44 blocks), paired stimulation only (35 blocks), and a combined priming and paired stimulation condition (48 blocks).

Illumination during priming periods resulted in increased evoked responses network-wide

To assess opsin functionality during each experimental block containing a priming period, we analyzed the evoked responses as a result of illumination. Illumination throughout the cranial window resulted in photo-induced artifacts that were also visible in saline testing. We used principal component analysis (PCA) to obtain principal components associated with photo-induced artifacts obtained from saline testing. After projecting our *in vivo* data onto these saline-obtained bases, we reconstructed the neural signal without photo-induced artifacts (Figure 1C). To obtain the evoked response after each 900 ms pulse, we calculated the average of broadband power during the pulse and divided it by the average broadband power for the 500 ms prior to illumination. Consistent with previous reports, we observed increases in overall broadband power especially in higher frequency bands (Figure 1D) (Griggs et al., 2024). Similar to previous observations, we attributed this increase in power to the silencing of more superficial cortical layers which are known to consist of a significantly higher proportion of inhibitory neurons. Previous studies have demonstrated that inhibitory stimulation in neocortical layers 2/3 can result in increased activity in deeper layers, which reflect high frequency oscillations recorded in LFP signals (Pierce et al., 2025; Yazdan-Shahmorad et al., 2011, 2013). Across the network, we observed that the calculated evoked responses were greater than sham evoked responses obtained from the baseline period preceding the priming period of each block (paired sample t-test, $p = 4.3099e-05$), suggesting that optical illumination during the priming period resulted in network-wide inhibitory effects (Figure 1E).

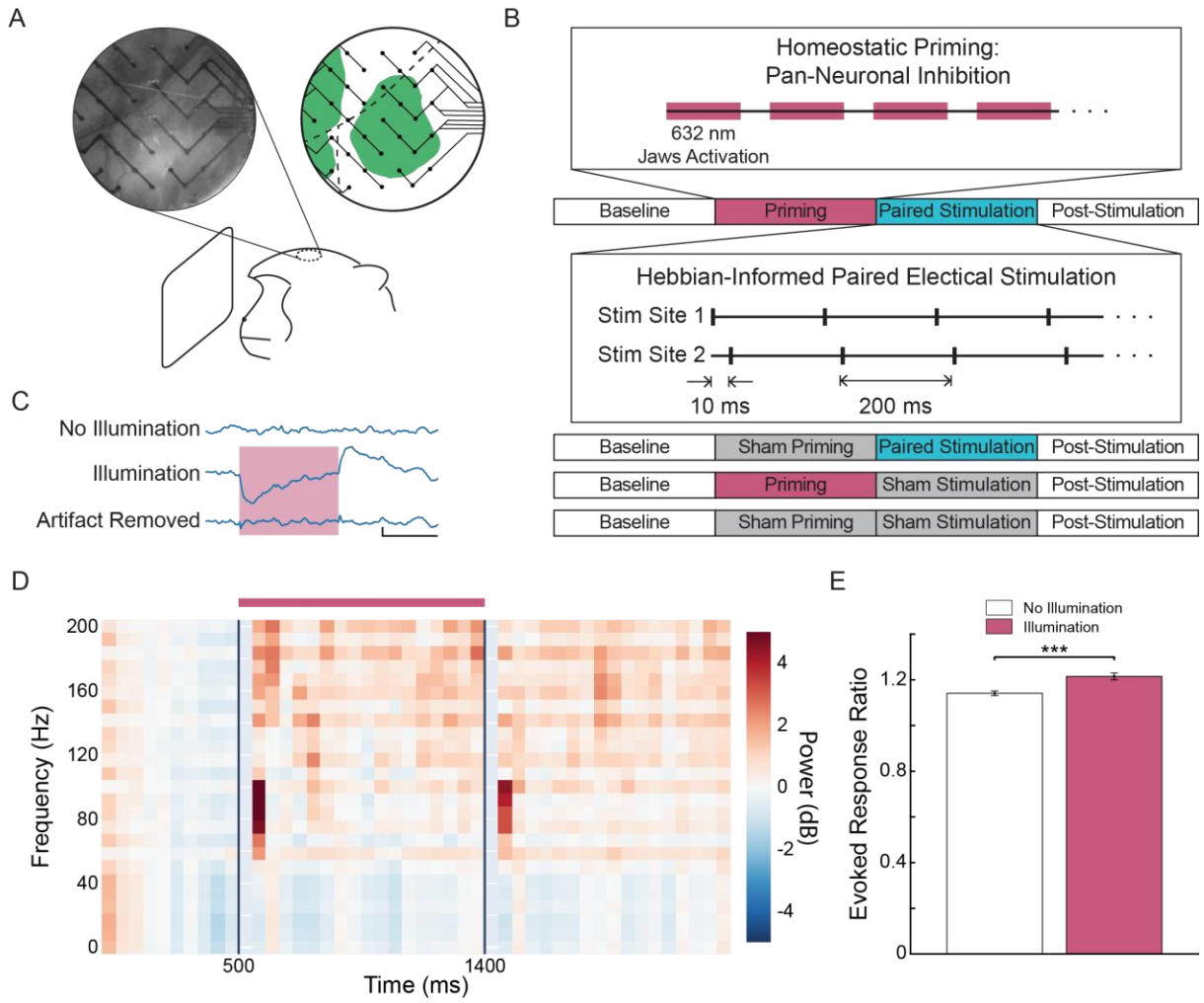

Figure 1. Experimental design and opsin expression validation. A) Cranial window in monkey L with implanted 32-electrode electrocorticographic (ECoG) array (left panel) and epifluorescence imaging demonstrating underlying pan-neuronal expression of Jaws-GFP (right panel). Throughout the experiment, monkeys were head-fixed while placed in front of a monitor. B) Schematic of recording blocks for each experimental condition. Each of the four periods within each block are 10 min in length. C) Example LFP traces without illumination, during illumination with illumination artifacts, and during illumination with the illumination artifacts removed. Vertical scale bar is 250 μV, horizontal scale bar is 500 ms. D) Example spectrogram before, during and after illumination of the same LFP trace shown in (C). Power values within each frequency are normalized to the 500 ms prior to illumination and the log base 10 of those values are shown in the spectrogram. The pink bar indicates the illumination time which lasted 900 ms. E) Mean network evoked responses calculated as the ratio of the broadband spectrogram values during and before illumination ($p = 4.3099e-05$, paired sample t-test).

Homeostatic priming prior to Hebbian-informed stimulation facilitates targeted and network-wide functional connectivity increases

Previous work has demonstrated the capability for Hebbian-informed paired stimulation to induce changes in functional connectivity across an entire recorded network (Bloch et al., 2022, 2019;

Rebesco and Miller, 2011; Rebesco et al., 2010; Seeman et al., 2017; Yazdan-Shahmorad et al., 2018a). To assess the local changes in functional connectivity, we calculated high gamma band (60-150 Hz) multivariate Granger causality (GC) across all possible pairs of electrodes across the ECoG array during the baseline and post-stimulation periods of each experimental block (Figure 2A-B). We hypothesized that the GC from the first stimulation site to the second stimulation site would increase for blocks in which a priming period preceded Hebbian-informed paired electrical stimulation. Indeed, we found that GC significantly increased in blocks conditioned with priming and paired electrical stimulation (one-sample t-test, $p = 0.047$) (Figure 2C). This was not the case in the unconditioned control blocks and blocks conditioned with either a priming period or paired stimulation period alone (one-sample t-tests; unconditioned: $p = 0.124$; stimulation only condition: $p = 0.645$; priming only condition: $p = 0.277$). From the second stimulation site to the first stimulation site, however, we did not observe any significant changes in GC in any of the conditions (one-sample t-test; unconditioned: $p = 0.0537$; stimulation only: $p = 0.192$; priming only: $p = 0.522$; priming with stimulation: $p = 0.072$; Figure 2C).

We next assessed the effect of priming the network prior to Hebbian-informed stimulation on functional connectivity changes throughout the entire recorded network (Figure 2B,D). We found that blocks conditioned with a priming period prior to Hebbian-informed stimulation exhibited significantly greater increases in GC across all connections in the recorded network compared with control conditions (one-sample t-tests for comparisons within each group; one-way ANOVA and two-sample t-tests for across group comparisons with Bonferroni corrections for multiple comparisons; Figure 2D). Unexpectedly, we found that in the unconditioned blocks, the overall network GC decreased significantly (one-sample t-test; $p = 8.92e\text{-}29$). We also observed significant decreases in GC in both singly conditioned blocks (one-sample t-test; stimulation only: $p = 9.13e\text{-}4$; priming only: $p = 9.76e\text{-}08$). The decreases in GC under these two conditions were significantly smaller in magnitude compared to the decreases observed in the unconditioned blocks (two-sample t-tests with Bonferroni corrections for multiple comparisons; unconditioned-stimulation only: $p = 2.077e\text{-}10$; unconditioned-priming only: $p = 3.13e\text{-}14$). These data suggest that the relative increases observed in the singly conditioned blocks may compound in the doubly conditioned blocks to facilitate greater increases in functional connectivity across the network. Together, these results align with our initial hypothesis that the pre-stimulation network state can be homeostatically primed to facilitate both targeted and network-wide changes in functional connectivity.

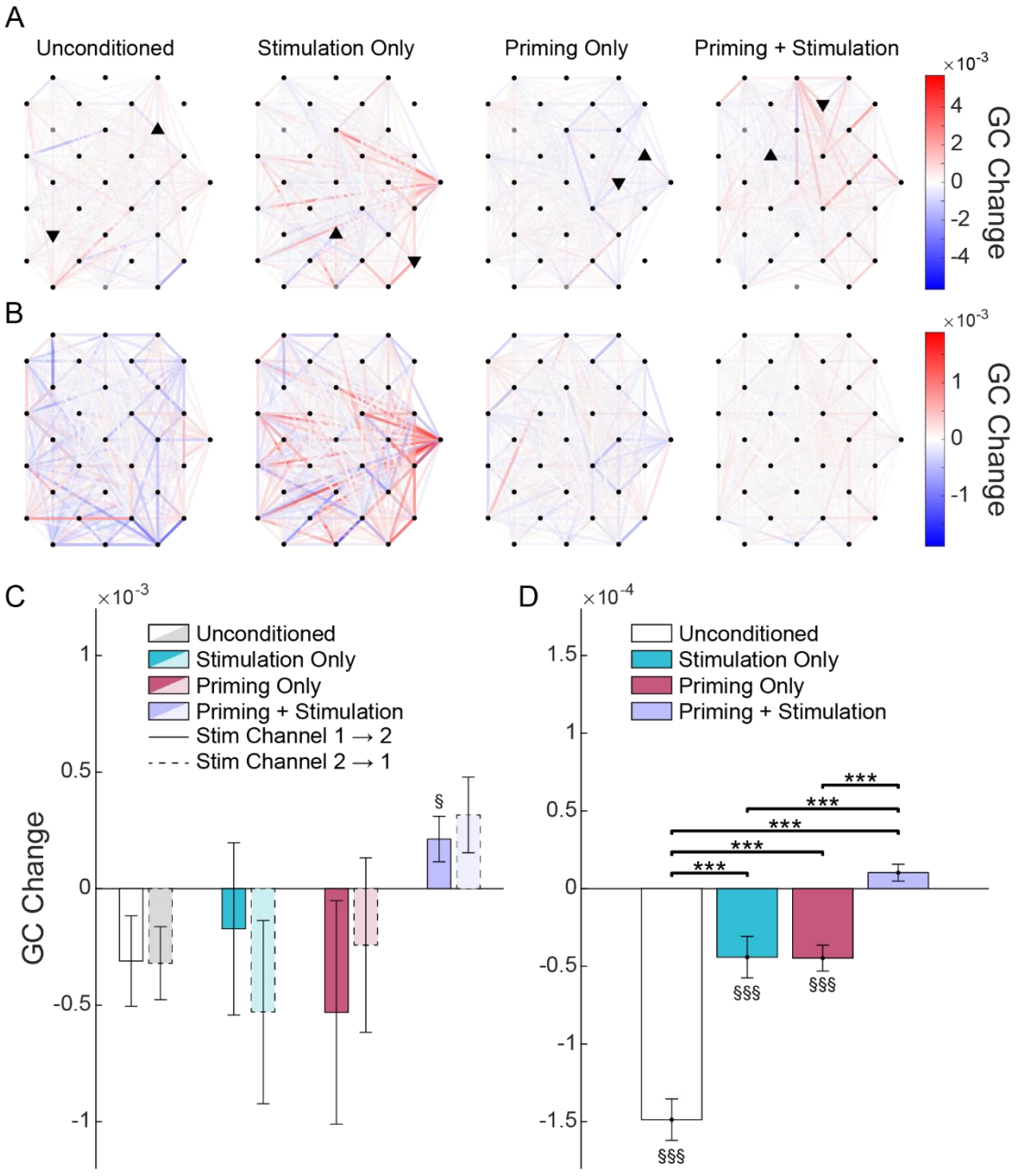

Figure 2. Local and network-wide changes in GC. A) Example node and edge plots depicting the change in GC from the baseline to the post-stimulation period for each experimental condition. Each node represents an electrode in the ECoG array. Upward pointing triangular nodes depict the first stimulation site within that block. Downward pointing triangles denote the second stimulation site for the shown block. The color of each edge represents the change in GC from baseline to the post-stimulation period. B) Average changes in GC across all blocks for each experimental condition. C) GC changes between both stimulation sites. Solid bars represent GC changes from the first stimulation site to the second stimulation site for each condition. Dashed bars represent GC change from the second stimulation site to the first stimulation site. D) Network-wide GC changes for each condition. In both (C) and (D), one-sampled t-tests were used to detect significant changes

in GC within each condition (§ denotes $p < 0.05$, §§§ denotes $p < 0.001$) and one-way ANOVA followed by pairwise two-sample t-tests with Bonferroni corrections for multiple comparisons to compare across groups (*** indicates $p < 0.001$).

Functional connectivity change becomes less predictable and less reliant on the underlying network

Previous stimulation studies have demonstrated the strong importance of the underlying network in determining post-stimulation changes in functional connectivity (Bloch et al., 2022, 2019). In fact, features of the underlying network played a bigger role in influencing functional connectivity change compared to stimulation protocols, including Hebbian-informed paired optogenetic stimulation in NHP sensorimotor cortex (Bloch et al., 2022). Here, we similarly assessed the role of both network and protocol features in determining functional connectivity change as a result of each experimental condition by running 50 iterations of a random forest model consisting of 100 decision trees. Protocol features included: the animal subject, the experimental condition, order of the block, distance between electrodes of each connection, distances between stimulation sites, distances between electrodes of a given connection and the stimulation sites, illumination-evoked response ratios at each site of a given connection, illumination-evoked response ratios at each of the stimulation sites, and the extent of illumination throughout the cranial window. Network features included: the baseline GC of each connection, the baseline GC of the sites within a connection with respect to the stimulation sites, the baseline GC of the sites with respect to the rest of the network, and the baseline GC of the stimulation with the rest of the network. For subsequent cross validation, 30% of the data were randomly held out during each run. Feature importance was determined based on the loss in prediction accuracy after randomly permuting each feature then scaling the scores from 0 to 1, where a score of 1 was assigned to the most important and 0 to the least important of the considered features.

On average, the random forest model accounted for approximately 60.4% of the variance of the held-out test set with a 95% confidence interval (CI) from 59.6% to 61.1%. Among the protocol features, the distance between sites and the distance between stimulation sites were the most important predictors of GC change (Figure 3A). Consistent with previous findings, network features played a more significant role in determining GC change across all conditions in comparison with protocol features overall. The most important network feature across all conditions was the pair baseline GC. Notably, the importance of the pair baseline GC for blocks conditioned with both priming and stimulation was the lowest (95% CI: 0.44 ± 0.024) compared to the other conditions (unconditioned

95% CI: 0.88 ± 0.033; stimulation only 95% CI: 1.0 ± 0.025; priming only 95% CI: 0.67 ± 0.025; Figure 3A). Within the unconditioned blocks, the mean baseline GC from the network to any given pair of sites was also a significant predictor of GC change for that pair of sites (95% CI: 0.71 ± 0.049). We also assessed the prediction accuracy of the random forest model for each of the experimental conditions. The most predictable of the four experimental groups was the unconditioned group with an R^2 value of 0.73 ± 0.0096 (95% CI; Figure 3B). The singly conditioned groups were nearly equally predictable with R^2 values of 0.55 ± 0.015 (stimulation only condition 95% CI; Figure 3C) and 0.54 ± 0.014 (priming only condition 95% CI; Figure 3D). The combination of both priming and stimulation was the least predictable of the conditions with an R^2 value of 0.48 ± 0.019 (Figure 3E). These results indicate that while the underlying network remained a more prominent determinant of functional connectivity change compared to the stimulation protocol, the combination of priming and stimulation may have reduced the influence of the underlying network on functional connectivity change. This reduced network influence corresponded with reduced predictability of functional connectivity change when homeostatically priming the network prior to Hebbian-informed paired stimulation.

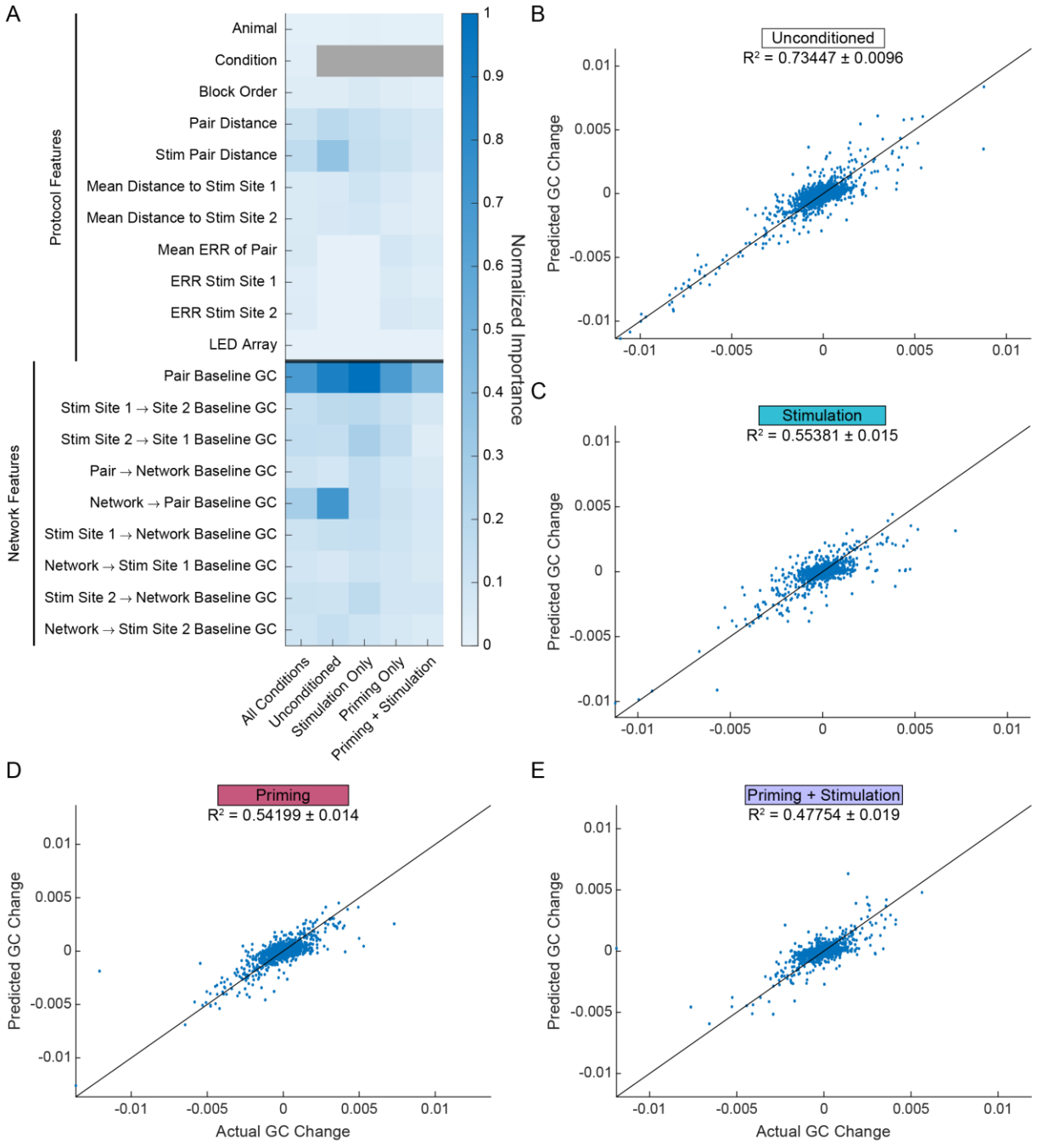

Figure 3. Random forest modeling to predict functional connectivity change. A) Heat map of mean feature importance scores for each experimental condition. Feature importance is scaled from 0 to 1, where 1 is the most important of the assessed features and 0 is the least important. (B-E) Model-predicted GC changes compared to calculated GC change from held out test sets from example random forest model runs for each experimental condition. R^2 values are reported as 95% confidence intervals across all 50 random forest trials. Solid diagonal lines represent y = x.

Homeostatic priming prior to Hebbian-informed paired stimulation non-preferentially distributes stimulation site communication

Functional connectivity and communication are two highly interdependent yet unidentical features of neural circuits. While metrics such as GC provide valuable insight into the functional connectivity between neural regions, they do not directly address the extent of actual neural communication. Here, we explored the degree to which neural communication is altered as a result of each experimental condition throughout the recorded network. We employed graphical diffusion autoregressive (GDAR) modeling of the signals (see Methods for model details) recorded during each of the conditions to infer changes in information flow (Schwock et al., 2024).

We calculated the change in GDAR flow magnitude from the baseline to the post-stimulation period of each block. Across all unconditioned blocks and blocks conditioned with only a priming period, we observed no discernible patterns of information flow change (Figure 4A-B). For blocks that contained a period of paired electrical stimulation, however, we observed a substantial proportion of blocks exhibiting stark changes in flow magnitude around both stimulation sites (Figure 4A-B). This was confirmed by conducting PCA on the changes in GDAR flow magnitudes and re-constructing those flow changes using the first principal component to visualize dominant flow fields throughout the recorded network (Figure 4B). We found that blocks conditioned with stimulation only and priming prior to stimulation displayed significantly greater changes in GDAR flow around the stimulation sites compared to unconditioned and priming only conditioned blocks (one-way ANOVA followed by pairwise two-sample t-tests across groups with Bonferroni corrections for multiple comparisons; family-wise error rate of 0.05; Figure 4C). Additionally, blocks conditioned with only a stimulation period displayed slightly greater flow magnitude change compared to doubly conditioned blocks ($p = 0.021$; two-sample t-test with Bonferroni corrections for multiple comparisons; Figure 4C).

We further investigated how the orientation of each connection with respect to the opposing paired stimulation site may contribute to whether the flow of any given stimulation site's connection increases or decreases. For example, we expected to see increases in flow magnitude for connections oriented in the direction of the opposing paired stimulation site. Conversely, for connections oriented away from the opposing paired stimulation site, we expected to observe decreases in flow magnitude. Thus, we hypothesized that information flow aligned with the axis of the paired stimulation sites would increase in blocks conditioned with a stimulation period.

Surprisingly, this was the case for blocks conditioned with only a stimulation period, but not for blocks conditioned with both priming and stimulation periods (Figure 4D). Within the stimulation only condition, connections oriented towards the opposing paired stimulation site exhibited a significantly greater change in flow compared to those oriented away from the opposing paired stimulation site ($p = 1.6e-5$; two-sample t-test with Bonferroni correction for multiple comparisons). For blocks conditioned with both priming and stimulation, connections oriented towards the opposing paired stimulation site did not significantly differ from those oriented away ($p = 0.075$; two-sample t-test with Bonferroni correction for multiple comparisons). These results indicate that paired electrical stimulation increased the amount of information flow between the stimulation sites and adjacent regions. Paired electrical stimulation was more effective at orienting information flow between the two stimulation sites. In contrast, priming prior to paired stimulation non-preferentially elicited changes in flow across all orientations around the stimulation sites.

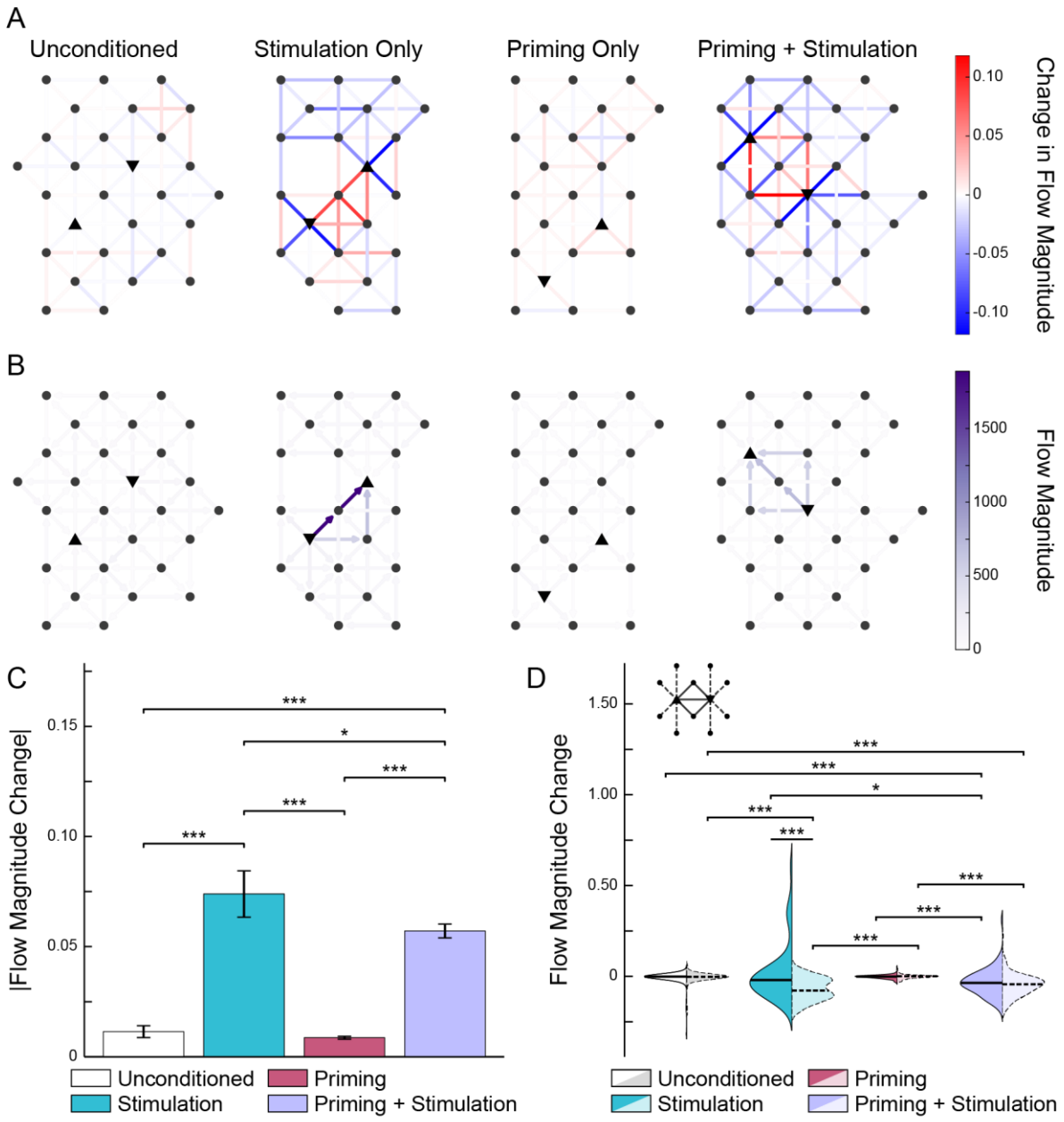

Figure 4. Evaluation of changes in information flow with respect to the stimulation sites. A) Node and edge maps from example blocks from each of the four conditions demonstrating the change in GDAR flow across the array. Each node represents an electrode in the array, while edges and their color represent the change in information flow between the nodes. B) PCA reconstruction of the changes in GDAR flow magnitude to highlight dominant flow fields. In both (A) and (B), upward pointing triangles indicate the first stimulation site, while downward pointing triangles indicate the second stimulation site. C) Absolute value of the GDAR flow magnitude for stimulation site connections across all conditions. D) Split violin plots showing GDAR flow magnitude changes for stimulation site connections oriented toward (left halves) and away (right halves) from the opposing paired stimulation site. Horizontal lines within each distribution indicate the median change in GDAR flow. For (C) and (D), comparisons across groups are one-way ANOVA followed by pairwise two-sample t-tests with Bonferroni corrections for multiple comparisons. For (D), comparisons between towards and away

distributions were performed within each group via two-sample t-tests with Bonferroni corrections for multiple comparisons. In (C) and (D), * indicates $p < 0.05$, ** indicates $p < 0.01$, and *** indicates $p < 0.001$.

Discussion

In this study, we tested whether short-term homeostatic priming through pan-neuronal inhibition immediately prior to a Hebbian-informed paired stimulation period could achieve greater functional connectivity increases than paired stimulation alone. We hypothesized that the inhibition of pan-neuronal activity could initiate homeostatic metaplastic mechanisms to facilitate stimulation-induced Hebbian corticocortical functional connectivity change. We tested this hypothesis using four experimental conditions, in which blocks were either unconditioned, conditioned with either a priming period or a paired stimulation period, or both (Figure 1B). We observed that illumination throughout the cranial window during priming periods induced greater evoked responses measured through surface ECoG recordings compared to baseline controls (Figure 1C-E). Blocks conditioned with combined priming and stimulation periods exhibited significant increases in GC from the first to the second stimulation site, but not in the reverse direction or in any of the other control conditions (Figure 2C). We also observed that doubly conditioned blocks had greater increases in network functional connectivity compared to singly conditioned and unconditioned blocks (Figure 2D). We then demonstrated through random forest analysis a reduced influence of the underlying network on subsequent functional connectivity change in doubly conditioned blocks (Figure 3A). We also found functional connectivity change to be less predictable when blocks were conditioned with both priming and stimulation periods (Figure 3E). Additionally, paired electrical stimulation was sufficient to drive changes in information flow between stimulation sites and their neighboring regions (Figure 4C). While stimulation alone facilitated increased information flow oriented towards opposing paired stimulation sites, priming prior to stimulation yielded information flow changes agnostic of orientation (Figure 4D).

Spectral effects of the homeostatic priming period

Consistent with previous results, we showed that illumination-induced activation of the inhibitory opsin Jaws triggered increased broadband and high frequency band signal power as measured through surface ECoG recordings (Griggs et al., 2024). This power increase was likely due to the higher proportion of inhibitory neurons in layer 2/3 which project down to deeper cortical layers (Kooijmans et al., 2020; Meyer et al., 2011). Because layer 2/3 is closer in proximity to the light source, the inhibition of these superficial layers can result in increased layer 5 activity. In our spectrograms, we observed increases in higher frequency power during illumination (Figure 1D), aligning with

previous observations that activity in deeper layers strongly accounts for higher frequency ECoG signals (Baratham et al., 2022; Griggs et al., 2024; Thio and Grill, 2023; Yazdan-Shahmorad et al., 2013).

Timing of the homeostatic priming period

The timing of the priming periods is a critical determinant of the efficacy of the approach explored here. Here, we only tested 10 min priming periods. Homeostatic metaplasticity mechanisms have been shown to operate on timescales of minutes to days (Abraham, 2008; Christie and Abraham, 1992; Clarkson et al., 2010; Huang et al., 1992; Yee et al., 2017; Zenke and Gerstner, 2017). In human studies, non-invasive homeostatic priming periods have been tested with 10 minute (Iyer et al., 2003; Müller et al., 2007; Siebner et al., 2004; Todd et al., 2009) and even 5 minute periods (Fricke et al., 2011). For this study, we elected to maintain priming periods to the shortest time scale at which homeostatic changes have been observed experimentally to maximize the number of experimental blocks recorded. The results of this study can lead to further exploration of longer and more sustained priming periods (e.g. through chemogenetic-based approaches) which may lead to more robust changes in functional connectivity. *In vivo*, metaplastic mechanisms have frequently been reported in sensory deprivation studies, primarily in the visual cortex, but also in auditory and somatosensory cortex (Lee and Kirkwood, 2019; Whitt et al., 2014). In such studies, the deprivation of sensory inputs can lead to overall reduction in activity of excitatory and inhibitory neurons within the sensory cortices (Feldman, 2009; Foeller et al., 2005; Hensch, 2005; Levelt and Ḧubener, 2012). We aimed to mirror these effects by utilizing the pan-neuronal human synapsin promoter to drive expression of the inhibitory opsin Jaws and did not limit expression solely to excitatory neurons. This simultaneous reduction in inhibitory activity can also aid in raising the excitability of excitatory neurons, particularly in layers 2/3 and 5.

We suggest that the homeostatic priming periods in this study promoted a downward shift in modification threshold for subsequent LTP induction. The interrogation of threshold shifts is typically accomplished through a combination of pharmacological, molecular, and single cell-level electrophysiology (Bridi et al., 2018; Lee and Kirkwood, 2019; Whitt et al., 2014). While we are limited in our ability to incorporate these approaches in large animals such as NHPs, it is critical for the question of threshold shifts to be explored more thoroughly in future studies. Moreover, it is possible that rather than shifting the LTP modification thresholds of layer 2/3 neurons, the priming periods in this study increased the excitability of excitatory neurons in layer 5. This increase in excitability as

discussed above and as evident in the illumination-evoked responses (Figure 1D-E) may have facilitated increased connectivity through layer 5 corticocortical connectivity. This would be supported by the increased high gamma band changes in GC that we observed in doubly conditioned blocks (Figures 2C-D). However, local corticocortical connections are thought to predominantly occur through layer 2/3 projections rather than through layer 5, which typically engage with more distant regions or within their individual cortical columns (Douglas and Martin, 2004; Thomson and Lamy, 2007). Thus, we hypothesize that the priming periods within this study facilitated in the downward shift in LTP modification threshold to help drive Hebbian functional connectivity change through layer 2/3 corticocortical connections.

Translational correlates

The interactions between homeostatic and Hebbian plasticity mechanisms have been heavily discussed in literature (Bridi et al., 2018; Turrigiano and Nelson, 2000; Vitureira and Goda, 2013). Hebbian-informed stimulation paradigms have been the primary target approach for inducing corticocortical connectivity changes (Bloch et al., 2022, 2019; Jackson et al., 2006; Lucas and Fetz, 2013; Seeman et al., 2017; Yazdan-Shahmorad et al., 2018a). Other groups have explored ways to implement homeostatic priming periods prior to Hebbian-based stimulation to facilitate or depress excitability along the corticospinal pathway using a combination non-invasive cortical stimulation techniques. In such studies, inhibitory stimulation prior to excitatory stimulation facilitated "LTP-like" increases in cortical excitability; conversely, excitatory stimulation prior to inhibitory stimulation facilitated "LTD-like" decreases in cortical excitability (Fricke et al., 2011; Iyer et al., 2003; Karabanov et al., 2015; Lang et al., 2004; Müller et al., 2007; Nitsche et al., 2007; Siebner et al., 2004; Takeuchi and Izumi, 2015; Todd et al., 2009). These studies focused exclusively on primary motor cortex excitability, wherein cortical excitability was measured by motor-evoked potentials. In contrast, similar approaches to reproduce these effects for intracortical connections did not yield the same results (Doeltgen and Ridding, 2011; Fricke et al., 2011). Karabanov and colleagues have suggested that this lack of reproducibility in intracortical circuits may be due to a smaller effect size within the complexly wired neocortex that would be difficult to detect through motor evoked potentials (Karabanov et al., 2015). Our reliance on spontaneous LFPs obtained through ECoG recordings in this study has allowed us to detect the hypothesized homeostatic priming effects in corticocortical connections. Moreover, previous studies have been mainly restricted to motor circuits with a few studies in somatosensory and visual cortex (Bliem et al., 2008; Gatica Tossi et al., 2013). It has since

remained uncertain whether these findings generalize to other cortical areas. In the present study, we provide evidence that this effect also manifests in the PPC, thereby extending its applicability beyond motor regions.

We demonstrated that a brief homeostatic priming period of activity suppression prior to Hebbian-informed paired electrical stimulation in NHP PPC helped promote subsequent Hebbian changes in both local and network corticocortical functional connectivity. We accomplished this by combining optogenetic inhibition with ECoG recording and stimulation. This work was enabled by our large-scale optogenetic interface. Through the spatial specificity of our interface, we were able to test multiple different stimulation sites across 157 blocks within a 25 mm diameter cranial window. Along with the temporal resolution of our ECoG recordings, we were able to detect changes in functional connectivity within the complex milieu of the *in vivo* NHP PPC, an achievement that is elusive in human studies that rely solely on non-invasive techniques. The previous successes in human studies using similar approaches, however, offer compelling support for the potential clinical translatability of this integrated strategy. It is vital that we continue to explore these approaches in a variety of neocortical regions, such as PPC, which is often associated with hemispatial neglect after stroke (Vandenberghe and Gillebert, 2009; Whitlock, 2017). Naturally, it is also crucial that these approaches are explored in diseased contexts, such as stroke. In particular, the exploration of these approaches in clinically relevant animal models such as NHPs has become increasingly more feasible with recent developments that allow for the integration of large-scale optical and neurophysiological tools (Griggs et al., 2022, 2024; Khateeb et al., 2020, 2022; Stanis et al., 2023; Yazdan-Shahmorad et al., 2016). Further exploration of this integrated metaplastic-Hebbian approach could lead to the development of effective treatments to restore the capabilities of lost or damaged neocortical regions in patients suffering from stroke and other neural injuries.

Methods

Two adult male rhesus macaques (monkey H, age 10; monkey L, age 10-11) were used in this study. Water was available to the animals ad libitum in their home cage with no special feeding restrictions. All procedures were performed under the approval of the University of Washington's Office of Animal Welfare and Institutional Animal Care and Use Committee and were compliant with the Guide for the Care and Use of Laboratory Animals.

Optogenetic Neural Interface

In this study, we utilized an optogenetic neural interface previously developed in our lab (Griggs et al., 2021a, 2019, 2022, 2024). Briefly, the interface consisted of a 25 mm diameter cranial window encapsulated with a custom titanium chamber providing access to the left posterior parietal cortex of both monkeys H and L. The exposed cortical regions were injected with AAV8-hSyn-Jaws-GFP (5.4 x 10^{12} viral particles/mL; University of North Carolina Vector Core) to pan-neuronally express the inhibitory opsin Jaws via convection enhanced delivery, a method our lab has previously demonstrated to achieve high levels of large-scale opsin expression in NHPs (Griggs et al., 2024; Khateeb et al., 2019a; Yazdan-Shahmorad et al., 2016). Jaws activation in the NHP frontal eye field has previously been shown to induce behavioral deficits in NHPs (Acker et al., 2016). Optogenetic expression was confirmed weeks later via epifluorescence imaging of the GFP tag and persisted for at least two years after injection (Figure 1A). In monkey H, data was collected approximately 22 months after viral injection. In monkey L, data was collected 18 months after injection, then 6 months after a subsequent injection procedure. The interface also consisted of a semi-transparent ECoG array with the capability to record LFPs and electrically stimulate the underlying areas (Figure 1A). Opsin expression and function were also verified by light-evoked responses measured by LFP signal power during Jaws activation under 632 nm light illumination (Figure 1C-E). Jaws-mediated inactivation in these animals has also been verified behaviorally in a center-out-reach task by our lab in previous studies (Griggs et al., 2024).

Experimental Block Structure

To test whether homeostatic priming prior to Hebbian-informed paired stimulation impacts any changes in stimulation-induced functional connectivity, each recording block consisted of the following periods: 10 minutes of recording baseline neural activity, 10 minutes of Jaws-mediated pan-neuronal inhibition (homeostatic priming period), 10 minutes of Hebbian-informed paired stimulation, and 10 minutes of recording post-stimulation neural activity (Figure 1B). In short, one experimental block consisted of a baseline, priming, stimulation, and a post-stimulation period. In total, we recorded 48 such blocks. We also recorded control blocks with a sham priming period (stimulation only condition; 35 blocks), a sham paired stimulation period (priming only condition; 44 blocks), and a combined sham priming and sham stimulation period (unconditioned; 30 blocks). Each day of experimentation consisted of up to 7 blocks of recordings. Throughout each session,

animals were head-fixed in a primate chair while watching television programs and received a random amount of juice reward at random intervals to maintain alertness and engagement.

Electrocorticographic Recording

ECoG signal recording and stimulation was conducted using a 32-channel ECoG array as described previously (Griggs et al., 2021a, 2024). In brief, the ECoG array (Ripple Neuro) consisted of 32 platinum electrode contacts with a 500 µm diameter and a 2 mm pitch embedded in a medical grade transparent insulating polymer. For stable chronic recordings, the flexible array was embedded in an artificial dura (Griggs et al., 2019). The array was then connected to a Ripple Neuro Grapevine Nomad device to acquire LFP signals at a sampling rate of 1 kHz. Signals were high-pass filtered above 0.1 Hz and comb-filtered at 60, 120, and 180 Hz to remove line noise. Prior to each recording session, electrode impedance measurements were obtained to exclude electrodes with abnormally high impedance (greater than 1 MΩ) from subsequent analysis.

Illumination for Jaws-Mediated Optogenetic Inhibition

During the priming period, 632 nm light pulses were delivered for 900 ms through a 4 x 4 or 3 x 5 miniature LED array spanning the cranial window, followed by a 900 ms off period. Light pulses were delivered for the entirety of the homeostatic priming period and were controlled through custom MATLAB code in communication with the Ripple Neuro Grapevine Nomad device. In 5 of the recorded blocks, illumination was delivered through all 16 LEDs of the 4 x 4 LED array. In the remaining blocks, illumination was delivered through only two LEDs overlying the targeted electrical stimulation sites via the 3 x 5 LED array. In each case, the illumination power density per individual LED was set to at least 1 mW/mm^2 as measured by a power meter (Thorlabs PM100D Power Meter and S121C Sensor) to ensure sufficient illumination of the underlying regions.

Hebbian-Informed Paired Electrical Stimulation

During the Hebbian-informed paired electrical stimulation period, two channels within the opsin-expressing regions were selected for each block. The stimulation pair was altered between consecutive blocks. Stimulation was delivered through the two selected channels with a 5 Hz burst frequency of 1 kHz biphasic pulses and a current amplitude of 5 µA. Each individual pulse was comprised of a 200 µs cathodic phase, a 33.3 µs interphase interval, followed by a 200 µs anodic phase. In accordance with canonical Hebbian spike-timing-dependent plasticity principles, stimulation trains between each pair of stimulation channels were offset by 10 ms.

Signal Pre-Processing

The LFP signals were analyzed in MATLAB (MathWorks, 2024b). We plotted the power spectral densities to identify and exclude channels with poor connections and recording quality. Channels with power spectral densities that did not exhibit the canonical 1/frequency^n curve were excluded from further analysis. To identify signal artifacts, we bandpass filtered the signals to obtain low gamma band signals (30-59 Hz). We then applied a threshold-based artifact detection and rejection algorithm to extract any movement artifacts from the signals. Briefly, the signal from each channel was normalized over time. Samples that exceeded 10 times the standard deviation of the signal were identified and excluded from analysis. Additionally, samples before and after the threshold was crossed that extended 10 times the length of the amount of time beyond the threshold were also excluded.

Evoked Response Testing

To evaluate the inhibitory effects of illumination on neural activity within the cranial window, we measured the evoked responses of each pulse recorded across the array during the homeostatic priming periods as described previously (Griggs et al., 2024). First, photo-induced artifacts were removed by recording photo-induced artifacts in saline and extracting the first three principal components via PCA. We then isolated *in vivo* recordings from each 900 ms pulse, including 500 ms before, and 900 ms after each pulse. The isolated *in vivo* pulse data was then projected onto the saline-based artifact models and the resulting estimated photo-induced artifact was regressed out of the *in vivo* recordings via linear regression (Figure 1C).

We generated multi-tapered spectrograms with 50 ms non-overlapping windows, five tapers, and 128-sample length fast Fourier transform between 1-200 Hz. The spectrograms were then normalized to the mean and standard deviation of the 500 ms period prior to each pulse within each frequency bin. The evoked response values were obtained by calculating the average broadband ratio of normalized power to the pre-stimulation period. The same procedure is also applied to data recorded within the baseline period with sham illumination periods to obtain evoked response ratios without illumination. A two-sample t-test was then performed to compare evoked responses during illumination and sham illumination across all channels and blocks that had a priming period (Figure 1E). Finally, the normalized power values were converted to decibels by taking the log base 10 of the power ratio and multiplying that value by 10 (Figure 1D).

Granger Causality Analysis

Signals from each block were divided into the four periods within a block (baseline, priming, stimulation, and post-stimulation). We calculated the multivariate Granger causality (GC) with a model order of 20 (determined empirically via the Akaike information Criterion) in 10-second sliding windows with a window overlap twice the model order (Barnett and Seth, 2014). Within each 10-second window, if an artifact had been previously identified within that window, then the GC value was not calculated. For each connection within each period within each block, the average GC value of all 10-second windows was calculated as the final GC value for that connection and period. To assess changes in local network functional connectivity we focused our analysis on high gamma band activity (60-150 Hz), although other frequency bands were also assessed (delta: 1-3 Hz; theta 4-7 Hz; alpha 8-11 Hz; beta 12-29 Hz; low gamma 30-59 Hz). The average GC values for each period were averaged across blocks within the same experimental condition and a paired sample t-test was used to assess the changes GC between the post-stimulation and baseline periods with Bonferroni corrections for multiple comparisons (family-wise error rate of 0.05). To map the changes in GC across the array, we first calculated the change in GC by subtracting baseline GC values from the post-stimulation GC values. Next, we averaged the GC values for each connection in both directions to obtain a single value for each connection that could be mapped onto 2-dimensional node and edge plots for visualization (Figure 2A-B). To assess the change in GC across the entire network for each experimental condition, the change in GC was averaged across all connections and blocks and compared to zero via a one-sample t-test with post-hoc Bonferroni corrections for multiple comparisons (family-wise error rate of 0.05). Similarly, the change in GC values was compared across groups via two-sample t-tests with Bonferroni corrections for multiple comparisons (family-wise error rate of 0.05; Figure 2D). The same approach was taken to assess the changes in GC between stimulated channels (Figure 2C).

Random Forest Analysis

We implemented random forest analysis to predict high gamma GC change across each connection from all blocks and conditions to assess which features may play a role in determining GC change. Among the features, we included features which we can control and features that are inherent in the underlying network and termed these protocol and network features, respectively. Protocol features included the animal (H or L), experimental condition, block order throughout the day, pair distance, distance between stimulation channels, mean distance of the pair to the first stimulation site, mean

distance of the pair to the second stimulation site, mean evoked response ratio of the pair, evoked response ratio of the first stimulation site, evoked response ratio of the second stimulation site, and whether the LED array illumination was targeted or across the entire cranial window. Network features included the baseline GC of the pair, baseline GC of the first stimulation site to the second stimulation site, baseline GC of the second stimulation site to the first stimulation site, the mean baseline GC of the pair to the rest of the network, the mean baseline GC from the network to the pair, the mean baseline GC from the first stimulation site to the rest of the network, the mean baseline GC from the network to the first stimulation site, the mean baseline GC from the second stimulation site to the rest of the network, and the mean baseline GC from the network to the second stimulation site.

To avoid the bias of utilizing the same baseline GC values that are used in calculating GC change for the random forest prediction, we classified every other 10-second window used to calculate the mean baseline GC for each connection as either a "feature" or "response" GC value. The mean of each of the feature and response GC values was obtained and used either as a feature or as a part of the GC change calculation used in the random forest model. We ran the random forest model in 50 iterations to account for biases of random permutations. Prior to implementing each random forest iteration, 30% of the data were randomly held out for later cross validation. Each iteration was trained using the fitrensemble function in MATLAB with 100 learning cycles. The mean R-squared value of all iterations was then calculated for the entire model and for each experimental condition individually. Next, the importance of each feature was assessed using the permutationImportance function in MATLAB, which computed importance by randomly permuting each feature and calculated the loss in prediction accuracy as a result. The importance score for each feature was then recorded as the difference between the average permuted error and the baseline error. We averaged and scaled the importance scores for each feature within each experimental condition across all random forest iterations between 0 and 1 by subtracting the minimum of all importance scores from each score and dividing by the maximum score.

Graphical Diffusion Autoregressive Flow Analysis

We assessed how information flow was altered after each experimental condition. We previously developed a GDAR model to estimate the extent of information flow at each recording site with its nearest neighboring sites (Schwock et al., 2024). In brief, the time series signal at each i^{th} recording site, $s_i[t]$, was modeled as a function of a combination of its previous time points through a memory

term, m_i, and the edge weights with adjacent neighbors, w_i. The flow between two adjacent nodes could thus be estimated as the product of the corresponding edge weight and the potential gradient (e.g. $s_1[t] - s_2[t]$). To include entire recorded network with N number of channels and E number of edges, the recorded potential at each node at each time t could be estimated as:

$$s[t] = (M - BWB^T)s[t-1],$$

where $M = diag(m)\ \epsilon\ \mathbb{R}^{N\times N}$ contained the memory terms at each node; $W = diag(w)\ \epsilon\ \mathbb{R}^{E\times E}$ contained the edge weights for each edge; $B\ \epsilon\ \mathbb{R}^{N\times E}$ described the topology of the recorded sites and contained values of 0, 1, and -1 to denote nodes containing edges and the arbitrary direction of the each edge. The values in M and W were obtained through linear regression. Since the potential gradient could then be calculated by $B^T s[t-1]$, The flow at each time t could then be estimated as:

$$f[t] = WB^T s[t-1].$$

When scaled up to the K^{th} model order, the potential estimate could be regarded as:

$$s[t] = \sum_{k=1}^{K}(M_k - BW_kB^T)s[t-k],$$

and the flow could be calculated as:

$$f[t] = \sum_{k=1}^{K} W_kB^T s[t-k].$$

We computed GDAR flow time series based on a model order of 10 and calculated the average GDAR flow values across all adjacent electrodes for each baseline and post-stimulation period for each of the conditions. The change in GDAR flow was obtained by subtracting the mean baseline values from the mean post-stimulation values. To assess the changes in GDAR flow with respect to the stimulation sites, we pooled all GDAR flow change values associated with each stimulation site within each experimental condition. The absolute value of the GDAR flow change relative to each stimulation site was compared across experimental conditions through one-way ANOVA followed by pairwise two-sample t-tests with Bonferroni corrections for multiple comparisons. Edges associated with each stimulation site were classified as either oriented towards or away from the opposing stimulation site by obtaining the dot product of the position vector between both stimulation sites and between the stimulation site and its adjacent nodes. If the dot product was negative, then that edge was classified as being oriented away from the opposing stimulation site, while a positive dot product classified the edge as being oriented towards the opposing stimulation site. Dot products of zero were classified as being oriented away from the opposing stimulation site. One-way ANOVA tests followed by pairwise two-sample t-tests with Bonferroni corrections for multiple comparisons

were conducted to compare similarly oriented GDAR flow changes across experimental conditions. Pairwise two-sample t-tests with Bonferroni corrections for multiple comparisons were also conducted to compare GDAR flow changes across both orientations within each group. For all pairwise two-sample t-tests with Bonferroni corrections for multiple comparisons, the family-wise error rate was held at 0.05.

Chapter 4: Disinhibition facilitates Hebbian-based functional connectivity change in rat primary somatosensory cortex

Karam Khateeb, Sophia Shan, Sergio Montalvo Vargo, Daria Gileva, Ali Alattar, Andre Cabrera, Maysam Chamanzar, Azadeh Yazdan-Shahmorad

Abstract

Neurons adapt their connectivity in response to experience, a process known as synaptic plasticity that is central to learning and memory. Many have hypothesized that these plasticity mechanisms can be engineered to restore any lost functions or behaviors as a result of neural injury such as stroke. Hebbian and homeostatic plasticity are two key classes of mechanisms by which the nervous system regulates and adapts synaptic strength. While most stimulation-based treatment strategies have attempted to engage Hebbian plasticity mechanisms, few attempts have been made to simultaneously engage mechanisms of homeostatic plasticity. Hebbian principles dictate that repeated coincidental neuronal activity results in the strengthening of neural connections. Homeostatic plasticity mechanisms, however, work to maintain consistent levels of communication between neurons, and are often considered as oppositional to Hebbian plasticity mechanisms. One way in which homeostatic plasticity mechanisms can mitigate Hebbian plasticity is by altering the amount of excitation and inhibition within the network. We hypothesized that chemogenetic-mediated reduction of inhibitory activity during Hebbian-informed paired stimulation could achieve greater strengthening of neural connections compared to Hebbian-informed paired stimulation alone. In rat primary somatosensory cortex, we found that simultaneous disinhibition and Hebbian-informed stimulation significantly increased functional connectivity between targeted regions. This treatment also increased functional connectivity across the entire recorded network. Additionally, simultaneous disinhibition and Hebbian-informed paired stimulation significantly increased network excitability. The results of this study highlight the potential for stimulation-based approaches that simultaneously engage disinhibitory and Hebbian mechanisms of plasticity to more effectively rewire cortical circuitry towards treating neurological disorders.

Introduction

Our memories and behaviors are encoded in the trillions of synapses connecting the neurons in our brains. The plastic nature of these synapses, the ability to strengthen and weaken connections,

enables us to acquire new skills and information, and is essential for our development and survival. Neurological disorders such as stroke often result in aberrant neural connectivity that causes debilitating deficits in cognition and behavior. One approach to treating these disorders is to harness the brain's natural mechanisms of plasticity to restore lost function following injury (Cramer, 2018; Edwardson et al., 2013; Grefkes and Ward, 2014). Hebbian and homeostatic plasticity represent two fundamental mechanisms underlying neural plasticity (Turrigiano, 2012; Turrigiano and Nelson, 2000; Vitureira and Goda, 2013). According to Hebbian principles, repeated coincidental firing of a postsynaptic and a presynaptic neuron results in a strengthening of connections between the two neurons (Hebb, 1949) (long-term potentiation, LTP). However, this could initiate a positive feedback loop that can lead to circuit instability. For example, correlated activity resulting in LTP can lead to further correlated activity and subsequent LTP in a continuous loop (Turrigiano and Nelson, 2000). Thus, homeostatic plasticity is hypothesized to stabilize neural circuits by maintaining consistent levels of activity at physiologically relevant levels across short and long timescales. In developing plasticity-based treatments for neurological disorders, Hebbian plasticity mechanisms are often employed, in which LTP can be induced in a targeted manner by stimulating postsynaptic neurons shortly after presynaptic neurons (Bi and Poo, 1998; Edwardson et al., 2013; Jackson et al., 2006; Nishimura et al., 2013; Seeman et al., 2017). However, the limited efficacy of stimulation paradigms to induce corticocortical LTP *in vivo* (Bloch et al., 2022, 2019; Seeman et al., 2017; Yazdan-Shahmorad et al., 2018a) suggests that, among other factors, homeostatic plasticity mechanisms may play a critical role in affecting outcomes of stimulation-induced LTP (Feldman, 2012; Ting et al., 2020). For example, studies suggest that homeostatic mechanisms regulate LTP by modifying excitatory/inhibitory (E/I) ratio (Peters et al., 2017; Wilmes et al., 2016).

In this homeostatic paradigm, increased neuronal activity that results from strengthened excitatory synapses may also lead to strengthened inhibitory synapses (Andrei et al., 2023; Rannals and Kapur, 2011; Turrigiano and Nelson, 2000). These changes can occur by increasing postsynaptic receptor numbers and brain-derived neurotrophic factor secretion to restore network E/I ratio in opposition to changes in neural activity (Feldman, 2002; Turrigiano, 2012; Turrigiano and Nelson, 2000; Turrigiano et al., 1998). Additionally, it has been shown that in response to increased activity of excitatory neurons (for example, as a result of stimulation), excitatory inputs onto inhibitory neurons and inhibitory inputs onto excitatory neurons are both strengthened to maintain network E/I ratio (Andrei et al., 2023; Chang et al., 2011; Rannals and Kapur, 2011; Rutherford et al., 1998; Whitt et al., 2014). In fact, it has been demonstrated that this strengthening of inhibitory synapses can regulate the

potentiation of excitatory synapses by eliminating back-propagating action potentials (Wilmes et al., 2016), which are crucial for coincidence detection during Hebbian plasticity (Bi and Poo, 1998; Feldman, 2012; Markram et al., 1997). Therefore, reduction of inhibitory inputs onto excitatory neurons during learning could increase their excitability and tune synaptic plasticity towards potentiation. In rat primary somatosensory cortex (S1), spontaneous disinhibition of excitatory neurons has been shown to occur in layer 2/3 (L2/3) following whisker deprivation to maintain spiking rates (Li et al., 2014) and promote plasticity (Gambino and Holtmaat, 2012). In primary motor cortex (M1), an *ex vivo* rat slice preparation study demonstrated that corticocortical stimulation-induced LTP could only be induced when stimulation was combined with local pharmacological blocking of inhibitory synapse neurotransmission (Hess and Donoghue, 1994). In a separate study in which mice were trained to perform a lever press task, longitudinal structural two-photon imaging revealed decreases in inhibitory synaptic inputs onto excitatory neurons (Chen et al., 2015). Interestingly, these decreases only occurred at synapses with inhibitory neurons of the somatostatin subtype (Chen et al., 2015). Moreover, disruption of this naturally induced disinhibition by optogenetic activation or deactivation of somatostatin inhibitory neurons during natural motor learning resulted in destabilization and hyperstabilization of dendritic spines, respectively (Chen et al., 2015). Importantly, both manipulations of somatostatin inhibitory neuronal activity resulted in impaired motor learning (Chen et al., 2015). In another study, disinhibition of excitatory neurons during rotarod motor learning by vasoactive intestinal peptide-expressing neurons was also shown to play a critical role in motor learning (Donato et al., 2013). Therefore, disinhibition of excitatory neurons during stimulation-induced plasticity may be critical for increasing the efficacy of LTP induction *in vivo*, mimicking natural cortical circuit-wide mechanisms of learning. However, studies demonstrate that disinhibition is a delicately tuned process (Dobrzanski et al., 2022; Peters et al., 2017). For example, the reduction of inhibition must be approached cautiously, to avoid the induction of seizure-like activity (Goldenberg et al., 2023).

In this study, we suppressed the activity of inhibitory neurons during Hebbian-informed paired electrical stimulation in rat S1. We examined whether disinhibition during paired whisker stimulation could strengthen functional connectivity between stimulation sites. The rat S1 forms an ideal testbed for this approach. Studies have shown that cortical columns within rat S1 are highly interconnected through horizontal corticocortical projections via L2/3 excitatory neurons (Adesnik and Scanziani, 2010; Feldmeyer, 2012). Many studies have also demonstrated the capability to induce plastic changes within S1 of adult rodents (Cheng et al., 2014, 2021; Dobrzanski et al., 2022; Feldman, 2000;

Han et al., 2015; Jacob et al., 2007; Li et al., 2014). We therefore hypothesized that chemogenetic-mediated disinhibition of S1 during Hebbian-informed paired electrical stimulation could induce greater strengthening of functional connectivity compared to disinhibition or paired electrical stimulation alone. We demonstrated that chemogenetic suppression of inhibitory neurons in S1 increased overall network excitability. We then found that disinhibition combined with paired electrical stimulation yielded a significant increase in functional connectivity between stimulation sites. Stimulation-induced functional connectivity changes were also significantly increased across the network compared to disinhibition or paired stimulation alone. Additionally, the combination of paired stimulation and disinhibition in S1 greatly increased network excitability. These results suggest that stimulation-based approaches to rewire cortical circuitry can be more robust when engaging multiple mechanisms of plasticity.

Results

We tested the effects of disinhibition during Hebbian-informed paired electrical stimulation on functional connectivity changes in rat S1 (Figure 1A-B). A total of 23 adult Sprague Dawley rats (11 male and 12 female) were divided among four treatment groups: untreated, disinhibition only, paired stimulation only, or combined disinhibition and paired stimulation. Rats were injected with AAV1-hDlx-hM4Di-P2A-dTomato (Dimidschstein et al., 2016) in S1 to express the inhibitory DREADD (designer receptor exclusively activated by designer drugs), hM4Di, in inhibitory neurons (Figure 1A). Approximately, 4 to 5 weeks later, rats were implanted with a 32-channel micro-electrocorticographic (μECoG) array to record and stimulate cortical activity (Vargo et al., 2025). Under urethane anesthesia, we recorded 10 minutes of spontaneous baseline surface local field potentials (LFPs). Next, animals were injected intraperitoneally (IP) with 0.5 mg/kg deschloroclozapine dihydrochloride (DCZ) to activate the expressing hM4Di receptors in S1 inhibitory neurons, thus initiating the disinhibition period (Nagai et al., 2020). DCZ was chosen for its minimal off-target effects *in vivo*, offering a more selective alternative to traditional chemogenetic compounds like clozapine-N-oxide (Nagai et al., 2020). Animals in the untreated or stimulation only treatment groups were instead administered with an equivalent volume of saline. Within the disinhibition period, animals received six 10 min blocks of Hebbian-informed paired electrical stimulation or sham stimulation, depending on their treatment group. Untreated and disinhibition only treatment groups received sham stimulation. These six stimulation blocks were interspersed with 5 min blocks of LFP recordings to allow for the measurement of neurophysiological changes over

time. Finally, a 10 min post-stimulation period was recorded for subsequent comparisons with the baseline period to assess changes in functional connectivity (Figure 1C).

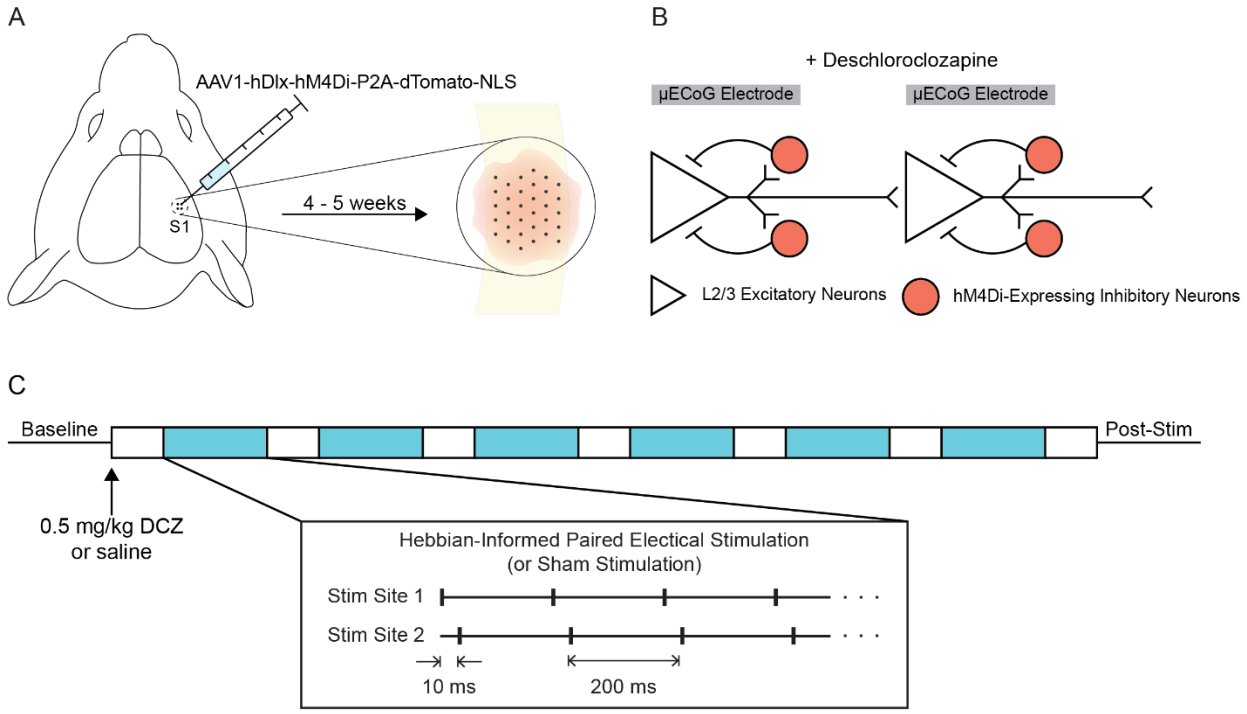

Figure 1. Schematic of experimental design. A) Surgical procedures schematic. Animals were injected in four different locations with a viral vector to express the inhibitory DREADD in inhibitory neurons via the hDlx enhancer in S1. Approximately four to five weeks later, a 32-channel μECoG array was implanted in a 5 mm diameter cranial window overlying S1 regions expressing the viral construct (shown in red). B) Conceptual schematic of hypothesized mechanism of action. Inhibitory neurons expressing hM4Di were activated by IP DCZ injection. We hypothesized that this disinhibition of L2/3 excitatory neurons would facilitate functional connectivity change after Hebbian-informed paired stimulation. C) Timeline of each recording session. An initial 10 min baseline period was recorded, followed by a disinhibition/stimulation period. Animals were either injected with 0.5 mg/kg DCZ or saline. During this period, animals received six 10 min blocks of Hebbian-informed paired stimulation or sham stimulation. Stimulation blocks were interspersed with 5 min blocks of recordings to track changes over time. A final 10 min period of post-stimulation activity was also recorded.

Inhibitory DREADD expression in inhibitory neurons in primary somatosensory cortex

We first assessed whether the construct was expressed in inhibitory neurons and within L2/3 of S1. We co-stained free-floating coronal slices to visualize the dTomato fluorescent marker expression, along with parvalbumin (PV) and DAPI (4',6-diamidino-2-phenylindole, nuclear stain). As expected, we observed strong dTomato expression throughout cortex in the injected region (Figure 2A) that was not present in the contralateral hemisphere. Strong dTomato expression was observed within L2/3, confirming that injection locations and depth yielded the expected localization (Figure 2A). Co-

staining for PV markers also demonstrated that construct expression coincided with PV interneurons. However, not all cells that expressed PV also expressed dTomato. Likewise, not all dTomato-positive cells were positive for PV. PV interneurons are only one subclass of inhibitory interneurons within neocortex, and co-staining for additional interneuronal subtypes can further confirm the extent to which the construct was expressed within each interneuron subtype. Conversely, co-staining against excitatory neuronal markers could confirm a lack of expression in excitatory neurons. These results confirm that the construct was expressed within inhibitory neurons.

Designer drug administration increases cortical excitability

We set out to measure the effect of DCZ administration on network excitability. We plotted multi-tapered spectrograms of signals obtained from animals injected with saline and DCZ to assess the effect of DCZ injection on the spectral nature of the μECoG signals. In saline-injected animals from the untreated group, we found that the spectral features were unaltered after saline injection and remained relatively uniform throughout the entirety of the 115 minutes of recording (Figure 2B). In contrast, we observed a stark increase in lower frequency power from signals recorded in DCZ-treated animals within minutes after IP DCZ injection (Figure 2B). This increase in low frequency power persisted throughout the remainder of the recordings.

One method of evaluating changes in structured network excitability is by analyzing phase-amplitude coupling (PAC). Throughout cortex, slower theta oscillations (4-7 Hz) are thought to be responsible for globally modulating excitability of local networks. In particular, peaks in excitability are known to correspond with the troughs of theta oscillations within local circuits (Buzsáki and Draguhn, 2004; Buzsáki and Wang, 2012; Canolty and Knight, 2010; Chrobak and Buzsáki, 1998; Lin et al., 2006). We therefore analyzed PAC throughout the network to assess how lower frequency oscillations modulated local activity as represented by higher frequency oscillations (Figure 2C). In animals injected with DCZ, we observed a significant increase in theta phase modulation index (MI) of both beta (10-30 Hz; two-sample t-tests with Bonferroni corrections for multiple comparisons; saline-baseline: $p = 0.008$, DCZ-baseline: $p = 2.62e\text{-}4$; DCZ-saline: $p = 4.31e\text{-}16$) and low gamma (30-60 Hz; saline: $p = 0.045$; DCZ: $p = 4.40e\text{-}5$; DCZ-saline: $p = 7.74e\text{-}17$) band amplitudes (Figure 2C-E). These differences were also reflected in comodulograms, which visualize MI values across all analyzed phase and amplitude frequencies (Figure 2C-D).

We also assessed the phase preferences for amplitude modulation of each treatment group during the baseline period and after saline or DCZ injection. In DCZ-injected animals, for which we anticipated greater excitability, we expected to observe phase preferences more closely aligned with the troughs of theta phases near ±180°. Animals injected with DCZ exhibited a strong preference for coupling to occur near troughs of theta oscillations in both beta and low gamma bands (Figure 2F). For theta-beta coupling, the mean preferred phases during baseline were -17.60° (99.9% confidence interval (CI): -25.99° to -9.21°) in saline and -2.41° (99.9% CI: -17.04° to 12.21°) in DCZ-injected animals (Figure 2F). After saline injections, the mean preferred phase was relatively unshifted (mean: -17.47°, 99.9% CI: -19.40° to -13.54°). After DCZ injection, the mean preferred phase significantly shifted towards the troughs (mean: -150.43°, 99.9% CI: -156.32° to -144.54°). For theta-low gamma coupling, the preferred mean phases at baseline were -5.26° (99.9% CI: -11.69° to 1.18°) in saline and -8.32° (99.9% CI: -20.22° to 3.59°) in DCZ-injected animals. The mean phase preference was relatively unshifted in saline-injected animals (mean: -2.10°, 99.9% CI: -5.32° to 1.13°). As expected, the mean phase preference was shifted significantly towards theta troughs in DCZ-injected animals (mean: -143.27°, 99.9% CI: -149.91° to -136.63°). Thus, not only did we observe a significant increase in PAC after DCZ injection, the phases during which there was increased coupling shifted towards the troughs, indicating an increase in structured excitability.

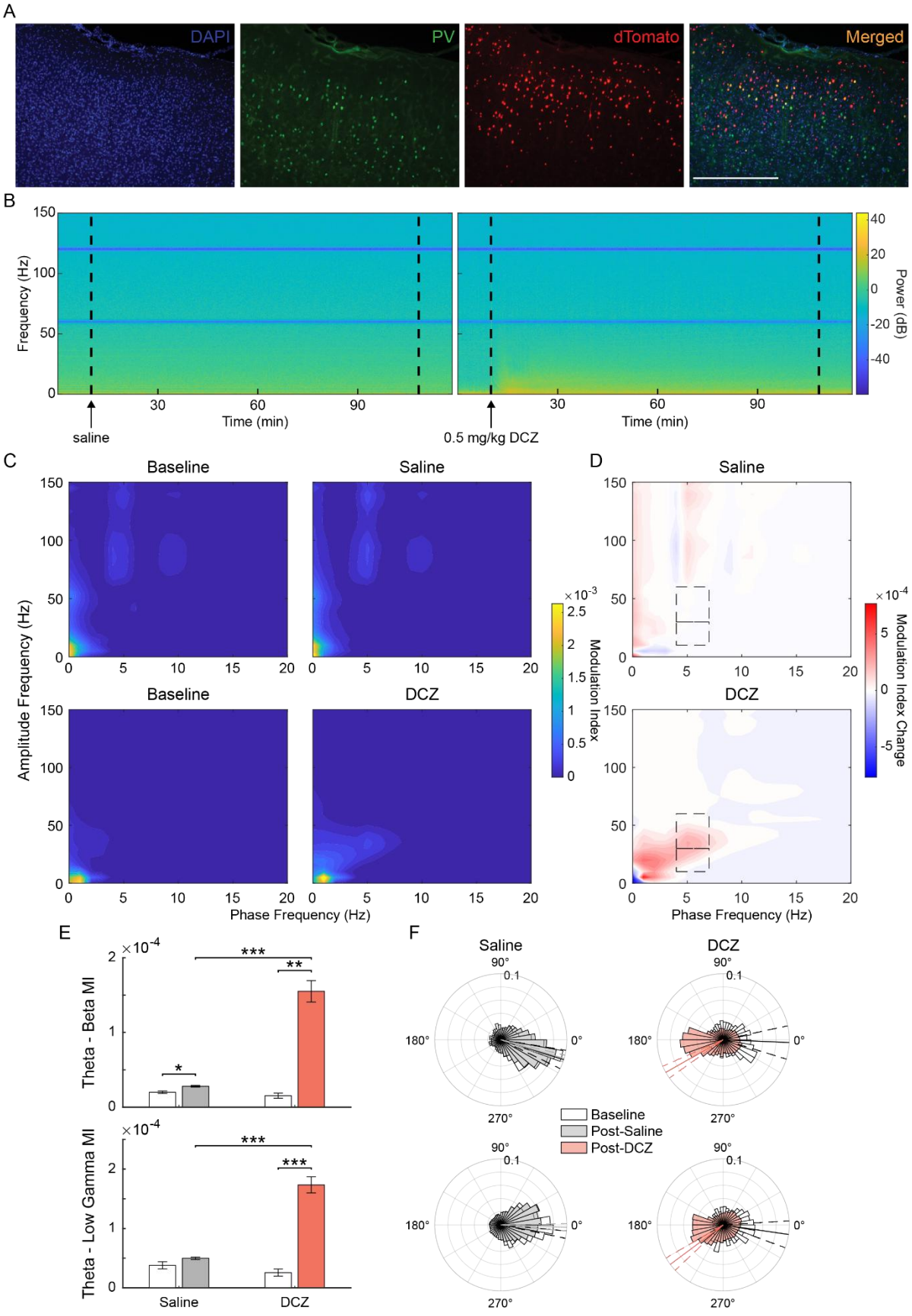
A
DAPI
PV
dTomato
Merged
B
Frequency (Hz)
Time (min)
saline
0.5 mg/kg DCZ
Power (dB)
C
Baseline
Saline
Baseline
DCZ
Amplitude Frequency (Hz)
Phase Frequency (Hz)
Modulation Index
D
Saline
DCZ
Phase Frequency (Hz)
Modulation Index Change
E
Theta - Beta MI
Theta - Low Gamma MI
Saline
DCZ
F
Saline
DCZ
Baseline
Post-Saline
Post-DCZ

Figure 2. Construct expression and validation of function. A) Immunohistochemistry (IHC) staining confirming expression of dTomato in inhibitory neurons. Scale bar is 500 μm. B) Example spectrograms comparing the spectral effects of saline and DCZ injection in two different animals. In the right spectrogram, saline was injected IP after ten minutes of recording. In the left panel, DCZ was injected IP. C) Average comodulograms during baseline (left panels) and after injection of saline (top right) and DCZ (bottom right). Plotted comodulograms are averaged across all channels within each treatment group. Top two comodulograms are the average of all channels and animals in the untreated group. Bottom two comodulograms are the average of all channels and animals in the disinhibition only group. D) Change in MI across all phase and amplitude frequencies plotted as a comodulogram. Top comodulogram is from saline-injected (untreated) animals, bottom comodulogram is from DCZ-injected animals (disinhibition only treatment group). The statistical differences for the frequency windows are assessed in (E). E) Mean MI values for theta-beta and theta-low gamma coupling for the frequency windows highlighted in (D). Two-sample t-tests were conducted with Bonferroni corrections for multiple comparisons (*: $p < 0.05$; **: $p < 0.01$; ***: $p < 0.001$). F) Polar histograms showing the distributions of the preferred phases for PAC. Top row shows the distributions for theta-beta PAC in saline (left) and DCZ-injected (right) animals. Bottom row shows the distributions for theta-low gamma PAC. Solid and dashed lines denote the mean and 99.9% confidence intervals of the preferred phases.

Disinhibition facilitates stimulation-induced Hebbian functional connectivity change

We calculated high gamma (60-150 Hz) multivariate Granger causality (GC) to investigate changes in functional connectivity of the regions underlying the μECoG array. We analyzed high gamma band signals due to their known representation of localized activity (Buzsáki and Wang, 2012). High gamma GC was calculated across all possible pairs of electrodes during the baseline and post-stimulation periods of each animal (Figure 3A-B). We hypothesized that GC from the first stimulation site to the second stimulation site would increase in animals treated with both disinhibition and Hebbian-informed paired electrical stimulation. Indeed, we found that animals in this treatment group exhibited a significant increase in GC from the first stimulation site to the second stimulation site (Figure 3C; paired sample t-test; $p = 0.037$). This was not the case for the GC change from the second to the first stimulation site ($p = 0.76$). Similarly, the GC between stimulation sites did not change significantly in the other treatment groups.

We also considered how GC changed across the entirety of the network. We found that GC increased significantly across all electrode pairs in animals that received Hebbian-informed paired stimulation after DCZ injection (Figure 3D; one-sample t-tests for comparisons within each treatment group; one-way ANOVA and two-sample t-tests for comparisons across groups with Bonferroni corrections for multiple comparisons). As expected, there was no significant change in GC across the network in untreated animals ($p = 0.96$). We also observed significant decreases in network GC in animals in the disinhibition only ($p = 1.28e\text{-}9$) and stimulation only ($p = 9.45e\text{-}5$) treatment groups. Together, these

results support our hypothesis that disinhibition during Hebbian-informed paired stimulation can facilitate Hebbian functional connectivity changes between targeted sites and across the network.

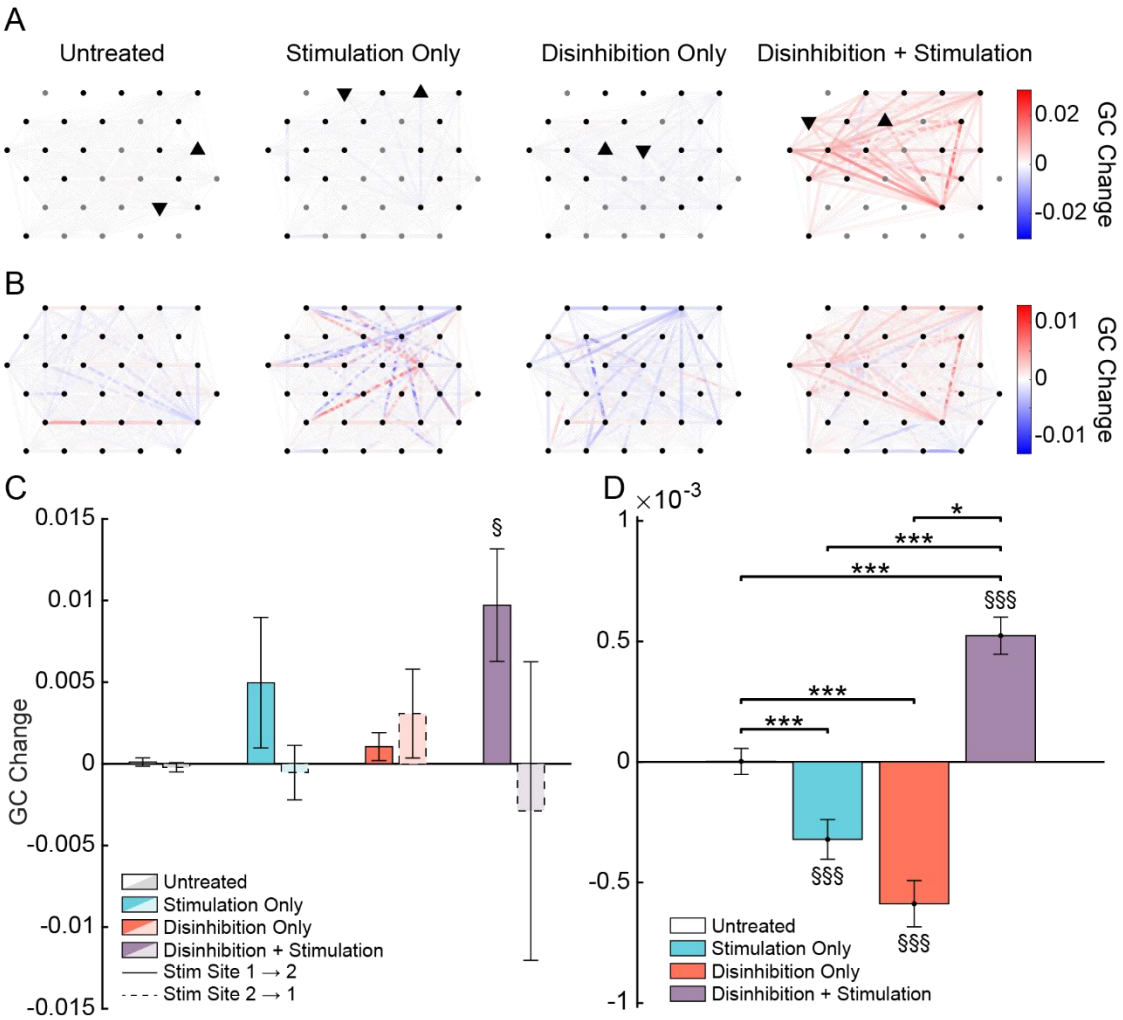

Figure 3. Changes in GC across the network and between stimulation sites. A) Example node and edge maps from each treatment group showing the changes in GC between the baseline and post-stimulation periods. The color of each edge represents the change in GC for that connection. GC change values are plotted as the average of GC changes in both directions. Upward pointing triangles represent the first stimulation site; downward pointing triangles represent the second stimulation site. B) Average node and edge maps for each treatment group. C) GC changes between stimulation sites in each treatment group. Solid bars represent GC changes from the first stimulation site to the second stimulation site. Dashed bars represent GC changes from the second stimulation site to the first stimulation site. D) Network-wide GC changes in each treatment group. In (C) and (D), one-sample t-tests were conducted to assess changes in GC within each treatment group (§ denotes $p < 0.05$, §§§ denotes $p < 0.001$), and one-way ANOVA followed by pairwise two-sample t-tests with Bonferroni corrections for multiple comparisons were conducted to compare across groups (* denotes $p < 0.05$, *** denotes $p < 0.001$).

Hebbian-informed stimulation during disinhibition increases structured network excitability

Previously, we demonstrated that disinhibition by injecting DCZ IP increases structured network excitability as evidenced by increased theta-beta and theta-low gamma PAC (Figure 2C-E). These increases in PAC corresponded with an increase in gamma activity preference for the troughs of the slower theta oscillations (Figure 2F). We next investigated the effects of each treatment on network excitability during and beyond the stimulation periods (Figure 4). In comparison with other treatment groups, the combined disinhibition and paired stimulation treatment group exhibited PAC that was orders of magnitude greater (Figure 4A-B). This was consistent for delta (0-3 Hz) phase and theta phase modulation of beta and low gamma amplitudes. For the untreated, disinhibition only, and stimulation only treatment groups, delta phase modulation was not significantly increased after DCZ injection and into the post-stimulation period. When assessing theta phase modulation, the disinhibition only treatment group exhibited a sharp increase in modulation of beta and low gamma amplitudes then gradually decreased over time. In contrast, paired stimulation during disinhibition caused theta phase modulation to remain sharply increased over time and through the post-stimulation period (Figure 4B). In the stimulation only treatment group, PAC increased slightly and only after four stimulation blocks. Animals in the untreated group exhibited minimal fluctuations in PAC over time.

Next, we investigated the PAC phase preferences during the baseline and post-stimulation periods to probe whether the increases in PAC corresponded with increased network excitability. As expected, theta phase preference remained unshifted from the baseline to the post-stimulation period in untreated animals during theta-beta and theta-low gamma PAC (Figure 4C-D). Paired stimulation alone minimally shifted theta phase preference during beta (baseline 99.9% CI: -25.46° to -14.10°; post-stimulation 99.9% CI: -0.90° to 14.20°) and low gamma (baseline 99.9% CI: -6.40° to 6.62°; post-stimulation 99.9% CI: 6.93° to 18.17°) amplitude modulation. In contrast, disinhibition and disinhibition with paired stimulation yielded stark reversals in phase preferences. Disinhibition alone shifted the mean phase preference from -2.41° (-17.04° to 12.21° 99.9% CI) during theta-beta baseline PAC to -172.62° (-192.88° to -152.37 99.9% CI) during the post-stimulation period. During theta-low gamma coupling, disinhibition shifted the mean phase preference from -8.32° (-20.22° to 3.59° 99.9% CI) during baseline to -153.8° (-170.69° to -136.91° 99.9% CI) during the post-stimulation period. Similarly, mean theta phase preference for beta amplitude modulation was shifted from

32.22° (11.69° to 52.75° 99.9% CI) during baseline to 163.43° (135.79° to 191.07° 99.9% CI) during the post-stimulation period in animals that received paired stimulation after DCZ injection. In the same group of animals, the mean theta phase preference for low gamma amplitude modulation shifted from 17.05° (5.98° to 28.12° 99.9% CI) during baseline to 142.73° (116.02° to 169.44° 99.9% CI) during the post-stimulation period. Together, these results demonstrate that Hebbian-informed paired stimulation during disinhibition significantly increased PAC and structured network excitability compared to disinhibition alone, stimulation alone, or no treatment.

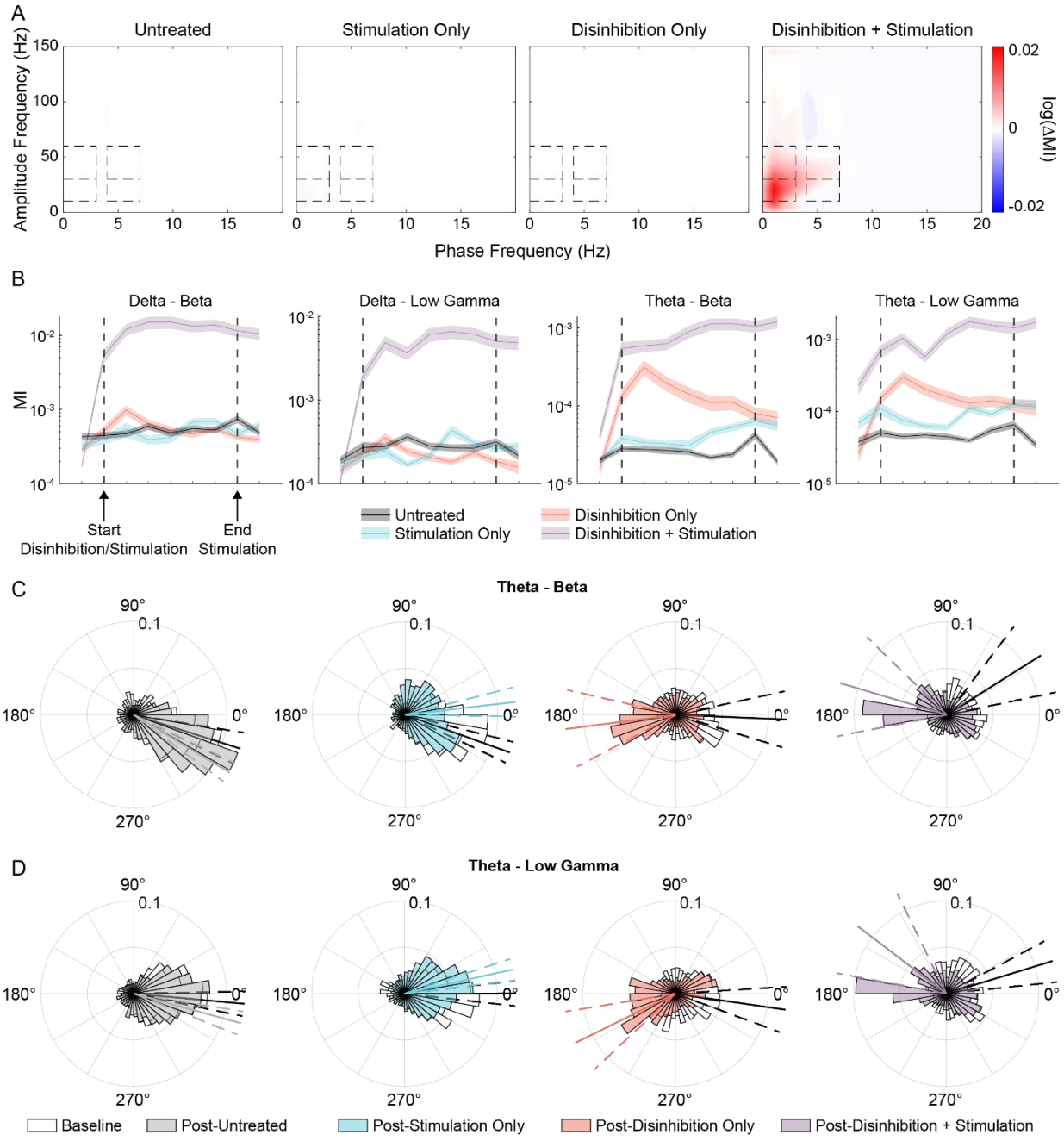

Figure 4. Hebbian-informed paired stimulation during disinhibition increases structured network excitability. A) Comodulograms showing the average change in MI for each phase and amplitude frequency across all four treatment groups. The log of the change in MI values are plotted to account for the multiple orders of magnitude difference in MI between the combined disinhibition and paired stimulation treatment group and the control treatment groups. Dashed boxes highlight the delta-beta, delta-low gamma, theta-beta, and theta-low gamma frequency windows over which there are the greatest changes in MI. B) Mean MI index for each treatment group within each of the highlighted frequency windows from (A). Plots are showing the mean and standard error of the MI on a log scale over time. Vertical dashed lines represent the point at which DCZ or saline was injected and the end of the stimulation period. C-D) Distributions of the phase preferences for theta-beta (C) and theta-low gamma (D) PAC during the baseline and post-stimulation periods. Solid lines

represent the mean theta phase preference for modulation and the dashed lines represent the limits of the 99.9% confidence intervals.

Discussion

In this study, we tested the effect of disinhibition during Hebbian-informed stimulation on stimulation-induced corticocortical changes in functional connectivity. We hypothesized that a degree of suppression of inhibitory activity could aid in the facilitation of stimulation-induced Hebbian functional connectivity change. We expressed the inhibitory DREADD, hM4Di, in inhibitory neurons. Drug-mediated activation of hM4Di resulted in an increase in network excitability within minutes of administration (Figure 2B-F, Figure 4), consistent with previously reported DCZ pharmacokinetics (Nagai et al., 2020). When applying Hebbian-informed paired stimulation, we observed a significant increase in functional connectivity from the first stimulation site to the second stimulation site (Figure 3C), as would be predicted by canonical Hebbian STDP principles (Bi and Poo, 1998; Feldman, 2012; Markram et al., 1997). The functional connectivity in the reverse direction, however, did not change significantly (Figure 3C). During paired electrical stimulation, the canonical STDP hypothesis proposes a decrease in connectivity from the second stimulation site to the first stimulation site (Bi and Poo, 1998; Feldman, 2012; Markram et al., 1997). In the case of this study, it is likely that the increased excitability throughout the network played a role in counteracting any LTD-like changes in functional connectivity. Network functional connectivity also increased as result of combined disinhibition and Hebbian-informed paired stimulation (Figure 3D). In contrast, network disinhibition alone and stimulation alone elicited decreases in network functional connectivity. This suggests that both perturbations, while facilitatory in nature, must be combined to drive Hebbian functional connectivity changes. We also showed that the combination of disinhibition and paired stimulation increased network PAC and excitability to a far greater degree than disinhibition alone (Figure 4).

Targeted changes in functional connectivity

The canonical Hebbian STDP principles would predict that repeated causal co-activation of neurons would result in an increase in functional connectivity from the “pre-synaptic” to “post-synaptic” neurons (Bi and Poo, 1998; Feldman, 2000, 2012; Markram et al., 1997). Stimulation-based attempts at inducing such corticocortical Hebbian functional connectivity changes have had limited success (Bloch et al., 2019; Seeman et al., 2017). In one non-human primate study, paired electrical stimulation was capable of inducing STDP-like changes in functional connectivity (Seeman et al., 2017). However, only two out of 15 pairs of stimulation sites exhibited such a relationship. This study

and others contribute to a body of evidence that suggest spike timing alone should not be the sole consideration for stimulation-induced functional connectivity change (Bloch et al., 2022, 2019; Feldman, 2012; Yazdan-Shahmorad et al., 2018a). Here, we demonstrated one such additional factor that should be considered when attempting targeted stimulation-induced corticocortical functional connectivity changes. Inhibitory inputs onto excitatory neurons are known to play a major role in mediating LTP (Andrei et al., 2023; Li et al., 2014; Rannals and Kapur, 2011; Vogels et al., 2011). Conceptually, increased inhibitory inputs onto excitatory neurons during periods increased activity stabilizes excitatory neuron firing rates and can counteract the coincidence detection mechanisms that are crucial for LTP (Rannals and Kapur, 2011; Vogels et al., 2011; Wilmes et al., 2016). Recently, Andrei and colleagues demonstrated that rapid homeostatic responses of inhibitory neuron plasticity in response to repeated optogenetic stimulation of excitatory neurons in macaque visual cortex to compensate for increased activity of excitatory neurons (Andrei et al., 2023). In L2/3 of rodent S1, rapid disinhibition during whisker deprivation increased L2/3 excitability and maintained whisker-evoked spiking activity (Li et al., 2014). We demonstrated that this concept of disinhibition can be applied towards facilitating targeted stimulation-induced functional connectivity change.

Stimulation-induced changes in network functional connectivity

Many studies have shown that electrical stimulation-induced functional connectivity changes can extend beyond the targeted sites of stimulation across rodent, non-human primate, and human studies (Bloch et al., 2022, 2019; Huang et al., 2019; Keller et al., 2018; Rebesco and Miller, 2011; Rebesco et al., 2010; Seeman et al., 2017; Yazdan-Shahmorad et al., 2018a). These changes have frequently been attributed to increases in excitability in the underlying cortical regions. Electrical stimulation of the cortex generates electric fields that can influence widespread cortical regions, both directly through volume conduction and indirectly via activation of structurally connected pathways (Komarov et al., 2019; McIntyre and Grill, 1999; Wongsarnpigoon and Grill, 2008). Thus, the widespread connectivity changes observed in previous stimulation studies were attributed to increased excitability propagating through neural tissue. In our study, however, Hebbian-informed stimulation alone did not increase functional connectivity throughout the network (Figure 3D), nor did it increase excitability in a sustained manner (Figure 4). In fact, paired stimulation alone decreased network functional connectivity. We attributed this to inhibitory (Andrei et al., 2023; Rannals and Kapur, 2011; Vogels et al., 2011; Wilmes et al., 2016) and metaplastic (Bienenstock et al., 1982; Turrigiano and Nelson, 2000) homeostatic responses to sustained increased activation.

Notably, the degree of disinhibition achieved by DCZ injection alone was not sufficient to achieve broad increases in functional connectivity. It is important to note that we did not test for potential off-target effects of DCZ injection alone in animals injected with a viral vector lacking hM4Di. The large increase in excitability due to simultaneous disinhibition and paired stimulation suggests that increased excitability must be beyond that of chemogenetic or stimulation-induced excitability alone to increase network functional connectivity. We suggest that the combination of increased excitability and Hebbian-informed stimulation was necessary to increase network functional connectivity.

One potential reason for the decrease in network functional connectivity when we only treated animals with paired stimulation is that our experiments were conducted under urethane anesthesia, whereas earlier studies (Bloch et al., 2022, 2019; Rebesco and Miller, 2011; Rebesco et al., 2010; Seeman et al., 2017; Yazdan-Shahmorad et al., 2018a) involved awake animals. Urethane anesthesia, while preserving some intrinsic oscillatory dynamics, may alter cortical excitability through enhanced inhibition and reduced neuromodulatory tone (Clement et al., 2008; Hara and Harris, 2002; Sceniak and MacIver, 2006). The extension of our approach to the non-anesthetized state may therefore yield stronger functional connectivity changes.

Granger causality as a functional connectivity metric

We opted to utilize high gamma band GC as a metric of functional connectivity across the recorded cortical regions. However, there are a plethora of alternative functional connectivity metrics that could have been used in this study, namely coherence and corticocortical-evoked potentials (CCEPs). A comparison of different approaches of inferring functional connectivity has been thoroughly discussed elsewhere (Bastos and Schoffelen, 2016; Hebbink et al., 2019). GC as a functional connectivity metric enables for the inference of directed connectivity from spontaneously recorded signals, in which the connectivity from a region A to a region B is not necessarily the same as from B to A. This approach allowed us to disambiguate connectivity changes originating from the first stimulation site to the second, and those in the reverse direction. Such a distinction is not possible when utilizing common non-directed metrics such as coherence (Bastos and Schoffelen, 2016). Moreover, GC allows for the consideration of signals from all electrodes and mitigates the confounding effects of common inputs that could result in the overestimation of weak connections.

CCEPs, wherein the response to stimulation is measured across recording sites, have been utilized extensively to estimate functional connectivity in rodents, non-human primates (NHPs), and humans

(Gronlier et al., 2021; Hebbink et al., 2019; Huang et al., 2019; Keller et al., 2018; Levinson et al., 2024; Seeman et al., 2017; Tavildar et al., 2019). CCEPs and sensory-evoked potentials could provide a more direct measure of functional connectivity that maintains directional specificity. In the rat barrel cortex within S1, for example, whisker-evoked responses measured in non-corresponding barrel fields could be a useful measure of connectivity between barrel fields. Such active stimulation-based methods of measuring functional connectivity could prove useful when testing similar approaches in future studies. One concern of employing active stimulation-based techniques is the potential for stimulation to alter network connectivity. As an alternative, however, GC allows for continuous measurement of connectivity without requiring external stimulation, making it ideal for studies with large numbers of electrodes.

Potential for translation

The approach tested here requires additional validation in other cortical regions and species prior to implementation in human studies. To our knowledge, no such approach has been tested in a pre-clinical or clinical setting. Great caution should be taken when reducing GABAergic activity, specifically to minimize the risk of epileptiform activity. Chemogenetic disinhibition has recently been used as a model for studying epilepsy in mice (Goldenberg et al., 2023). Throughout our study, we did not observe any such epileptiform activity. This may be due to the dosage used, the administration of DCZ under anesthesia, or the localized hM4Di expression. Alternatively, non-invasive methods of broadly increasing excitability may be effective alternatives, such as transcranial magnetic stimulation. However, such an approach would not directly address the rapid homeostatic responses of inhibitory neurons and may counteract or exacerbate these responses. Thus, there is value in exploring alternative approaches of cautious disinhibition, through localized or mild pharmacological administration.

In this proof-of-concept study, we demonstrated that the chemogenetic reduction of inhibitory activity during Hebbian-informed stimulation can induce both targeted and network-wide increases in functional connectivity. By integrating insights from both homeostatic and Hebbian plasticity mechanisms, we achieved more pronounced and widespread changes in functional connectivity. The approach presented here highlights the value of considering multiple mechanisms of plasticity in stimulation-based approaches aimed at rewiring cortical circuitry. Continued exploration of this approach can advance the development of targeted stimulation-based interventions for functional recovery after neurological insults such as stroke.

Methods

Animal Subjects

All animal procedures were approved by the University of Washington Institutional Animal Care and Use Committee and the Office of Animal Welfare. A total of 23 adult Sprague Dawley rats (males: ≥300 g; females: ≥ 250 g) were used for this study (11 male and 12 female), each of which were pre-assigned to one of four treatment groups such that roughly equal numbers of male and females were used for each treatment group. Treatment groups included: untreated (2 male, 3 female), disinhibition only (3 male, 3 female), paired stimulation only (3 male, 3 female), or disinhibition with paired stimulation (3 male, 3 female). Animals were housed with *ad libitum* access to food and water and on a 12-hour light/dark cycle.

Viral Vector Delivery

To achieve targeted inhibition of inhibitory neurons, we injected AAV1-hDlx-hM4Di-P2A-NLS-dTomato into S1 of adult Sprague Dawley rats. The viral vector used encodes for the expression of hM4Di driven by the hDlx enhancer element and has been previously used in NHPs (Dimidschstein et al., 2016). Animals were subcutaneously administered with slow-release Buprenorphine (1 mg/kg) 1-2 hours prior to surgery. All surgical procedures were conducted using standard sterile aseptic technique. Throughout each surgical procedure, vitals such as respiratory rate, temperature, heart rate, and oxygen saturation levels were continuously monitored to aid in the maintenance of appropriate anesthetic depth. Rats were anesthetized under 5% isoflurane and placed in a stereotaxic frame. Dexamethasone (0.5 mg/kg) was administered subcutaneously, and bupivacaine (2 mg/kg) and lidocaine (2 mg/kg) were administered subcutaneously local to the incision site. Throughout the procedure, animals were also administered with 1 mL/100 g of body weight of saline every 1-2 hours to maintain hydration levels. Under 1-2.5% isoflurane, an incision approximately 2 cm in length along the midline was made to expose the underlying skull. Four 0.5 mm diameter burr holes in the right hemisphere were made at approximately the following stereotaxic coordinates to target S1 based on stereotaxic coordinates from the rat brain atlas (Paxinos and Watson, 2007) (relative to Bregma): 4.2 mm posterior, 5.3 mm lateral; 2.8 mm posterior, 5.3 mm lateral; 2.8 mm posterior, 4.2 mm lateral; 4.2 mm posterior, 4.2 mm lateral. An injection 1 µL of viral vector (2.3×10^{13} vg/mL) in each burr hole was made at a depth of 1.2 mm at a rate of 0.1 µL/min followed by a 5 min wait period prior to needle extraction to avoid reflux of the virus. Approximately 30 minutes prior to

the end of procedure, rats were injected with 1 mg/kg meloxicam. The incision was then sutured, and the animals were allowed to recover. Sutures were removed 7-14 days later.

Micro-Electrocorticographic Array Implantation

Approximately 4 to 5 weeks after viral injection, rats were initially anesthetized under 5% isoflurane, placed in a stereotaxic frame and maintained at 2.5% isoflurane. The animals were then gradually transitioned to urethane anesthesia to enable recording of neural activity during the procedure. To transition, rats were administered 0.65 g/kg urethane (diluted 0.3 g/mL in saline) IP 10 minutes after initial isoflurane anesthetization and isoflurane was reduced to 2%. After 20-30 minutes, two 0.325 g/kg urethane were administered IP 10 minutes apart. Over the course of approximately one hour, isoflurane was gradually reduced from 2% to 0.5-0.75%. A dose of 0.65% urethane was administered IP 1 hr after the previous urethane dose. Additional 0.325 g/kg doses of urethane were administered as needed to maintain proper anesthetic depth throughout the remainder of the procedure. Animals were treated with 0.5 mg/kg dexamethasone subcutaneously approximately 1 hr prior to the initial incision. Saline (1 mL/100 g) was also administered subcutaneously every 1-2 hours to maintain animal hydration throughout the procedure.

The animal was placed in a stereotaxic frame and the skull exposed as before with a 2 cm incision along the midline. We then drilled a 5 mm diameter circular craniotomy with the center at approximately 3.5 mm posterior and 4.75 mm lateral to bregma in the left hemisphere. Next, a 32-channel μECoG array (Vargo et al., 2025) was placed on the exposed cortical surface. The array was secured by a custom 3D printed tray secured to the skull with two skull screws. One of the skull screws was placed a few millimeters posterior to lambda and was also used as a ground screw for recordings.

Signal Acquisition and Experimental Structure

After array implantation, isoflurane was reduced to 0% and animal anesthetic depth was solely maintained with additional 0.325 g/kg urethane doses if needed. The μECoG array was connected to the Ripple Neuro Grapevine Scout to acquire LFPs at a sampling frequency of 1 kHz. Electrode impedances were collected before and after data acquisition to exclude electrodes with high impedance (> 1 MΩ) from subsequent analysis. At least 1 hr after the elimination of isoflurane, signal acquisition was initiated. Each recording session began with 10 minutes of spontaneous baseline LFPs. Next, animals were injected with 0.5 mg/kg DCZ dihydrochloride (diluted 0.13 mg/mL in saline). We selected DCZ because it offers significant pharmacokinetic advantages over CNO, including

superior brain penetrance, rapid onset, high DREADD selectivity, and minimal off-target effects due to the absence of metabolic conversion into active compounds such as clozapine (Nagai et al., 2020). An equivalent volume of saline was administered IP for untreated or stimulation only treatment groups. Immediately afterwards, we recorded alternating blocks of 5 minutes of spontaneous activity and 10 minutes of Hebbian-informed paired electrical stimulation. Six blocks of Hebbian-informed paired stimulation were tested during this period and ended with another 5 min block of spontaneous activity (Figure 1C). Interleaving the paired stimulation blocks with blocks of spontaneous activity allowed us to record and analyze neurophysiological changes before and after each stimulation block. Afterwards, a final period of 10 minutes of spontaneous activity was recorded.

One pair of electrodes was selected for Hebbian-informed paired electrical stimulation for all 6 stimulation blocks for each animal. The electrode pair was selected such that both electrodes exhibited impedance values less than 1 MΩ. The two selected electrodes delivered 5 μA stimulation with 5 Hz burst frequency, 5 pulses per burst, and 1 kHz pulse frequency. In accordance with STDP principles, stimulation from each electrode was offset by 10 ms. Animals that were pre-assigned in the disinhibition only treatment group or the untreated group were given sham stimulation as controls. Signal acquisition and electrical stimulation was controlled by a custom MATLAB script (MathWorks, 2023) that interfaced with the Ripple Neuro Grapevine Scout and the Trellis acquisition software.

Immunohistochemistry

After post-stimulation neural activity and electrode impedances were recorded, animals were euthanized with Euthasol or 1.5 g/kg urethane and transcardially perfused with phosphate buffered saline (PBS) followed by 4% paraformaldehyde (PFA) in 1x PBS. The brains were extracted and placed in 4% PFA for approximately 24 hours at 4 °C then stored in 30% sucrose in PBS at 4 °C. The brains were then frozen and sliced on a sliding microtome (Leica) into 30 μm coronal slices, after which the slices were stored in 0.02% sodium azide in 1x PBS solution at 4 °C. To validate the expression of the construct in S1, free-floating slices were first incubated in blocking buffer (5% normal donkey serum, 0.3% Triton X-100, and 0.2% bovine serum albumin in PBS) for 1 hr at room temperature. The slices were then incubated in primary antibody solution (1:5000 mouse anti-PV, Swant 235; 1:500 rabbit anti-RFP, Rockland 600-401-379) diluted in blocking buffer for 24 hours at 4 °C. Slices were washed five times for 5 minutes in PBS at room temperature then incubated at room temperature for 2 hours

in secondary antibody solution (1:500 donkey anti-mouse alexa-fluor 488, Invitrogen #A-21202 ; 1:500 donkey anti-rabbit #A-10042) in blocking buffer with 2 µL of 300 nm 4',6-diamidino-2-phenylindole (DAPI). After 5 additional washes for 5 minutes in PBS, slices were incubated in 1:1 PBS:glycerol solution for 10 minutes at room temperature. Stained slices were then mounted onto glass slides in DABCO mounting medium (1,4-Diazabicyclo[2.2.2]octane, Sigma #D2522; 9:1 glycerol:PBS). Finally, slides were imaged on a Leica DM5500 B widefield fluorescent microscope.

Signal Pre-Processing

Signals were processed and analyzed in MATLAB (Mathworks, 2024b). We first applied a threshold-based artifact detection method to identify and reject LFP samples that were beyond physiologically plausible levels. We did this by bandpass filtering the signals to the low gamma band (30-59 Hz) and normalized the LFP signals over time. Data points exceeding ten standard deviations from the mean were removed from analysis. To account for potential surrounding artifacts, we also excluded data occurring before and after the threshold crossing for a period ten times longer than the duration of the threshold violation. Next, we plotted the power spectral densities of the signals from each electrode to exclude channels which may have had poor connections from subsequent analysis. Typically, these channels did not exhibit the canonical $1/\text{frequency}^n$ curve. We also plotted multi-tapered spectrograms (10 s windows with 2 s overlap, 5 tapers) using the mtspecgramc function from the Chronux toolbox (Vargo et al., 2025).

Functional Connectivity Analysis

We assessed changes in functional connectivity between regions underlying each electrode through high gamma band (60-150 Hz) GC. The multivariate GC during each period (baseline, post-injection/stimulation, and post-stimulation) was calculated in 10-second sliding windows with overlap between windows that was twice the model order of 15. The model order was determined empirically via the Akaike information criterion. Windows that had any previously identified signal artifacts were excluded from analysis. The final GC value for a given electrode pair and direction was calculated as the average GC value of all 10-second windows (excluding windows with artifacts). GC values were not calculated during the 10 min stimulation blocks but were calculated during the 5 min periods before and after each stimulation block. Changes in GC were calculated by subtracting the baseline GC values from the post-stimulation GC values. To assess overall network changes in GC, the GC change values from each connection were combined across animals. We conducted one-sample t-tests to assess changes in GC within each treatment group and one-way ANOVA followed

two-sample t-tests to compare changes across treatment groups with Bonferroni corrections for multiple comparisons (family-wise error rate of 0.05). We utilized the same approach to assess changes in GC between stimulation pairs. The changes in GC were mapped in node and edge plots by averaging the GC values in either direction. The average GC value was then represented by the color of the edge in the node and edge plot. For example, to visualize the change in GC between electrode A and electrode B, we calculated the average of the GC change from electrode A to B and electrode B to A.

Phase-Amplitude Coupling Analysis

To assess changes in excitability throughout the recorded network, we conducted phase-amplitude coupling analysis based on the approach developed by Tort et. al. (2010). First, Hilbert transforms were calculated to obtain time series of amplitudes and phases of each signal. The Hilbert phase of the signals was obtained from 0 to 20 Hz in 1 Hz steps. The Hilbert amplitude envelope of the signals was obtained for frequencies of 0 to 150 Hz in 5 Hz increments. Within each phase frequency, the phases are divided into 18 bins between 0 and 2π, within which the mean amplitude for each amplitude frequency was calculated and placed. The mean amplitudes were then normalized by the sum of all binned mean amplitudes. Next, the Shannon entropy of the normalized amplitude probability distribution was calculated. The Kullback-Liebler divergence was calculated to compare the distribution against a uniform distribution to obtain the modulation index (MI) (Tort et al., 2010). The MI was calculated for every combination of phase and amplitude frequencies from the signals of each channel. To compare MI values across saline and DCZ-injected groups, the average MI value within relevant frequency windows was calculated during the baseline and across the 7 inter-stimulation blocks. Two-sample t-tests were performed to compare across groups and periods with Bonferroni corrections for multiple comparisons. The phase preferences were obtained from the angle of complex vector mean constructed from the Hilbert amplitude envelopes and phases. Finally, the mean preferred phase and 99.9% confidence intervals were calculated using the Circular Statistics Toolbox (Berens, 2009).

Chapter 5: Future Directions and Challenges

The objective of this thesis is to provide a starting point for the development of stimulation-based strategies that engage multiple mechanisms of plasticity to treat dysfunctions arising from neural injuries such as stroke. Towards this aim, I first presented a toolkit that can allow us to induce reproducible and targeted focal ischemic lesions in cortex, monitor and modulate cortical activity, and examine vascular dynamics in a clinically relevant animal model, non-human primates (NHPs) (Khateeb et al., 2019b, 2022). I then explored two approaches towards leveraging homeostatic and Hebbian plasticity mechanisms in both NHPs and rats. In both instances, I showed that the combined consideration of homeostatic and Hebbian plasticity mechanisms facilitated targeted and network-wide functional connectivity changes. The next major step is to apply the approaches of the previous two chapters and other similar approaches in the context of ischemically lesioned cortex and assess their effect on functional recovery. There are several key challenges that need to be addressed in order to successfully translate these approaches to treat ischemic stroke.

The first major challenge is to identify relevant connections to target in the diseased state. It is important to differentiate that the approaches presented in this dissertation likely do not induce new connections but rather alter pre-existing connection strengths. In animal studies, we have the capability to identify pre-existing relevant and highly connected regions before inducing an ischemic lesion (Smits et al., 1991; Wang et al., 2022; Zeiger et al., 2021), after which those relevant connections can be targeted. In clinical settings, however, we do not have the advantage of being able to identify the relevant connections prior to stroke onset. One approach is to utilize our existing understanding of connectivity throughout the brain to target broadly connected regions. A limitation of such an approach is that the reliance on assumed stereotyped connections may not be directly applicable to each individual patient. Another potential strategy is to employ techniques such as diffusion tensor imaging to map the structural connectivity within the brains of patients to identify target regions (Christidi et al., 2022). In this manner, known existing connections can be targeted in a personalized manner.

Once the relevant connections are identified in the diseased state, the ability to target them in a specific and isolated manner remains a critical hurdle. In this dissertation, stimulation-induced functional connectivity changes occurred not only between the targeted regions, but also broadly across the network. Similar observations have been consistently observed in a multitude of studies (Bloch et al., 2022, 2019; Rebesco and Miller, 2011; Rebesco et al., 2010; Seeman et al., 2017;

Yazdan-Shahmorad et al., 2018a). Whether these broad network functional connectivity changes are beneficial in the diseased state remains to be seen. If such changes are found to be counterproductive towards functional recovery, more precise targeting methods can be explored. In exploratory animal studies, strategies that can isolate individual and even monosynaptic connections can be utilized to target specific relevant connections (Callaway and Luo, 2015; Jin et al., 2024). However, current iterations of these approaches present their own challenges by relying on cytotoxic rabies viral vectors (Chatterjee et al., 2018; Wickersham et al., 2007). Alternative retrograde AAV-based labeling strategies can therefore be co-opted to achieve similar levels of specificity.

Translating the approaches described here, as well as future strategies, into clinical settings remains a significant challenge. One potential non-invasive and targeted strategy could involve the systemic administration of AAVs that could then be delivered to specific regions of the brain through focused-ultrasound blood-brain barrier opening (Alonso et al., 2013; Li et al., 2024; Szablowski et al., 2018). This would allow for the delivery of chemogenetic constructs that could then be used to either homeostatically prime or cautiously disinhibit relevant local circuits. However, while there is increasing evidence that AAV-based therapies can be safe in humans (Maurya et al., 2022), the safety of chemogenetic constructs and ligands is yet to be fully investigated (Song et al., 2022). Alternatively, one viable path toward clinical translation is to transfer the use of invasive approaches into non-invasive methodologies. For example, electrocorticographic (ECoG) recordings can be replaced by electroencephalographic (EEG) recordings. Electrical stimulation can by emulated by transcranial direct current stimulation (tDCS) and transcranial magnetic stimulation (TMS). Moreover, different non-invasive stimulation parameters can have opposing effects on neural activity. Anodal tDCS and high frequency TMS (≥5 Hz) can depolarize neurons and increase their excitability. Cathodal tDCS and low frequency TMS (1 Hz) can hyperpolarize and reduce neuronal excitability (Chen et al., 1997; Karabanov et al., 2015; Nitsche et al., 2008; Takano et al., 2004). Thus, the effects of homeostatic priming as tested in Chapter 3 can be mimicked through cathodal tDCS or low frequency TMS. Similarly, the effects of disinhibition as tested in Chapter 4 may be mimicked through methods that increase excitability, such as high frequency TMS. A disadvantage of existing non-invasive approaches, however, is the loss of spatial and temporal specificity that might otherwise be needed to target specific neural connections. Consequently, the efficacy of these approaches when adapted to non-invasive methodologies is uncertain.

Finally, as discussed in Chapter 1, the processes that govern synaptic plasticity can depend on the synapse type and the overlying context (Egger et al., 1999; Feldman, 2012; Fino et al., 2005, 2007; Lu et al., 2007; Sjöström and Häusser, 2006; Tzounopoulos et al., 2004). Thus, depending on the neuronal composition of the target regions, different stimulation protocols may yield different results. The current approach in the field is to assume broad generalizability of generic synaptic plasticity "rules" such as STDP, metaplasticity, and disinhibition. As we have seen, there is no single rule that dictates how connectivity changes within a single synapse. Likewise, the mechanisms explored in this dissertation are unlikely to account for all relevant processes. The diverse mechanisms of plasticity that exist on the levels of individual synapses, single neurons, microcircuits, and networks all interact and influence one another across timescales. The different plasticity mechanisms that have been identified have generally been extracted and interpreted from idealized and carefully controlled experiments. Thus, it is important to recognize that classifying plasticity mechanisms into distinct categories or "rules" is a human-imposed simplification of an inherently complex system. This does not mean that the mechanisms we have identified are invalid or irrelevant. Nor does this imply that our efforts to induce plasticity through interventions are futile. On the contrary, intellectual and technological limitations necessitate that we first organize plasticity mechanisms into distinct classes (or rules) so that we can attempt to engage them to the best of our ability to treat patients suffering from serious sensorimotor and cognitive impairments.

The tools and approaches introduced in this dissertation are intended to form an initial step towards enhancing our ability to induce targeted changes in functional connectivity to restore lost functions in stroke patients. Although this work has centered on stroke, the proposed approaches may extend to other forms of neural injury, including traumatic brain injury. With the large-scale versatile toolbox discussed in Chapter 2 and the combination of Hebbian and homeostatic mechanisms explored in chapters 3 and 4, we can begin to develop effective treatment methods to promote functional recovery. These integrative strategies, used in conjunction with standard physical and occupational therapies, may enhance functional recovery following stroke and other neural injuries.

References

Abbott, L.F., and Nelson, S.B. (2000). Synaptic plasticity: Taming the beast. Nat. Neurosci. *3*, 1178–1183.

Abraham, W.C. (2008). Metaplasticity: tuning synapses and networks for plasticity. Nat. Rev. Neurosci. 2008 95 *9*, 387–387.

Acker, L., Pino, E.N., Boyden, E.S., and Desimone, R. (2016). FEF inactivation with improved optogenetic methods. Proc. Natl. Acad. Sci. U. S. A. *113*, E7297–E7306.

Adeoye, O., Hornung, R., Khatri, P., and Kleindorfer, D. (2011). Recombinant tissue-type plasminogen activator use for ischemic stroke in the united states: A doubling of treatment rates over the course of 5 years. Stroke *42*, 1952–1955.

Adesnik, H., and Scanziani, M. (2010). Lateral competition for cortical space by layer-specific horizontal circuits. Nature *464*, 1155–1160.

Alonso, A., Reinz, E., Leuchs, B., Kleinschmidt, J., Fatar, M., Geers, B., Lentacker, I., Hennerici, M.G., De Smedt, S.C., and Meairs, S. (2013). Focal delivery of AAV2/1-transgenes into the rat brain by localized ultrasound-induced BBB opening. Mol. Ther.-Nucleic Acids *2*, e73.

Andrei, A.R., Akil, A.E., Kharas, N., Rosenbaum, R., Josić, K., and Dragoi, V. (2023). Rapid compensatory plasticity revealed by dynamic correlated activity in monkeys in vivo. Nat. Neurosci. 2023 2611 *26*, 1960–1969.

Aoki, F., Fetz, E.E., Shupe, L., Lettich, E., and Ojemann, G.A. Increased gamma-range activity in human sensorimotor cortex during performance of visuomotor tasks.

Baran, U., and Wang, R.K. (2016). Review of optical coherence tomography based angiography in neuroscience. Neurophotonics *3*, 010902.

Baratham, V.L., Dougherty, M.E., Hermiz, J., Ledochowitsch, P., Maharbiz, M.M., and Bouchard, K.E. (2022). Columnar Localization and Laminar Origin of Cortical Surface Electrical Potentials. J. Neurosci. *42*, 3733–3748.

Barnett, L., and Seth, A.K. (2014). The MVGC multivariate Granger causality toolbox: A new approach to Granger-causal inference. J. Neurosci. Methods *223*, 50–68.

Barria, A., and Malinow, R. (2005). NMDA receptor subunit composition controls synaptic plasticity by regulating binding to CaMKII. Neuron *48*, 289–301.

Bastos, A.M., and Schoffelen, J.M. (2016). A tutorial review of functional connectivity analysis methods and their interpretational pitfalls. Front. Syst. Neurosci. *9*, 1–23.

Bear, M.F., Cooper, L.N., and Ebner, F.F. (1987). A physiological basis for a theory of synapse modification. Science (80-.). *237*, 42–48.

Berens, P. (2009). CircStat: A MATLAB Toolbox for Circular Statistics. J. Stat. Softw. *31*, 1–21.

Berger, T., Borgdorff, A., Crochet, S., Neubauer, F.B., Lefort, S., Fauvet, B., Ferezou, I., Carleton, A., Lüscher, H.R., and Petersen, C.C.H. (2007). Combined voltage and calcium epifluorescence imaging in vitro and in vivo reveals subthreshold and suprathreshold dynamics of mouse barrel cortex. J. Neurophysiol. *97*, 3751–3762.

Bi, G.Q., and Poo, M.M. (1998). Synaptic modifications in cultured hippocampal neurons: Dependence on spike timing, synaptic strength, and postsynaptic cell type. J. Neurosci. *18*, 10464–10472.

Bienenstock, E.L., Cooper, L.N., and Munro, P.W. (1982). Theory for the development of neuron selectivity: Orientation specificity and binocular interaction in visual cortex. J. Neurosci. *2*, 32–48.

Biernaskie, J., Szymanska, A., Windle, V., and Corbett, D. (2005). Bi-hemispheric contribution to functional motor recovery of the affected forelimb following focal ischemic brain injury in rats. Eur. J. Neurosci. *21*, 989–999.

Bliem, B., Müller-Dahlhaus, J.F.M., Dinse, H.R., and Ziemann, U. (2008). Homeostatic metaplasticity in the human somatosensory cortex. J. Cogn. Neurosci. *20*, 1517–1528.

Bliss, T.V.P., and Lømo, T. (1973). Long-lasting potentiation of synaptic transmission in the dentate area of the unanaesthetized rabbit following stimulation of the perforant path. J. Physiol. *232*, 357–374.

Bloch, J., Greaves-Tunnell, A., Shea-Brown, E., Harchaoui, Z., Shojaie, A., and Yazdan-Shahmorad, A. (2022). Network structure mediates functional reorganization induced by optogenetic stimulation of non-human primate sensorimotor cortex. IScience *25*.

Bloch, J.A., Khateeb, K., Silversmith, D.B., O'Doherty, J.E., Sabes, P.N., and Yazdan-Shahmorad, A. (2019). Cortical Stimulation Induces Network-Wide Coherence Change in Non-Human Primate Somatosensory Cortex∗. Proc. Annu. Int. Conf. IEEE Eng. Med. Biol. Soc. EMBS 6446–6449.

Bollimunta, A., Santacruz, S.R., Eaton, R.W., Moxon, K.A., Carmena, J.M., Correspondence, J.J.N., Xu, P.S., Morrison, J.H., and Nassi, J.J. (2021). Head-mounted microendoscopic calcium imaging in dorsal premotor cortex of behaving rhesus macaque. CellReports *35*, 109239.

Borich, M.R., Brodie, S.M., Gray, W.A., Ionta, S., and Boyd, L.A. (2015). Understanding the role of the primary somatosensory cortex: Opportunities for rehabilitation. Neuropsychologia *79*, 246–255.

Bouguer, P. (1729). Essai d'optique sur la gradation de la lumière (1729) (Kessinger Publihsing, 2009).

Bouyer, J.J., Montaron, M.F., and Rougeul, A. (1981). Fast fronto-parietal rhythms during combined focused attentive behaviour and immobility in cat: cortical and thalamic localizations. Electroencephalogr. Clin. Neurophysiol. *51*, 244–252.

Bridi, M.C.D., De Pasquale, R., Lantz, C.L., Gu, Y., Borrell, A., Choi, S.Y., He, K., Tran, T., Hong, S.Z., Dykman, A., et al. (2018). Two distinct mechanisms for experience-dependent homeostasis. Nat. Neurosci. *21*, 843–850.

Brinkman, J., Colebatch, J.G., Porter, R., and York, D.H. (1985). Responses of Precentral Cells During Cooling of Post-Central Cortex in Conscious Monkeys.

Brown, C.E., Aminoltejari, K., Erb, H., Winship, I.R., and Murphy, T.H. (2009). In vivo voltage-sensitive dye imaging in adult mice reveals that somatosensory maps lost to stroke are replaced over weeks by new structural and functional circuits with prolonged modes of activation within both the peri-infarct zone and distant sites. J. Neurosci. *29*, 1719–1734.

Buzsáki, G., and Draguhn, A. (2004). Neuronal olscillations in cortical networks. Science (80-.). *304*, 1926–1929.

Buzsáki, G., and Wang, X.-J. (2012). Mechanisms of Gamma Oscillations. Annu. Rev. Neurosci. *35*, 203.

Callaway, E.M., and Luo, L. (2015). Monosynaptic circuit tracing with glycoprotein-deleted rabies viruses. J. Neurosci. *35*, 8979–8985.

Canolty, R.T., and Knight, R.T. (2010). The functional role of cross-frequency coupling. Trends Cogn. Sci. *14*, 506.

Chang, M.C., Park, J.M., Pelkey, K.A., Grabenstatter, H.L., Xu, D., Linden, D.J., Sutula, T.P., Mcbain, C.J., and Worley, P.F. (2011). Narp regulates homeostatic scaling of excitatory synapses on Parvalbumin interneurons. *13*, 1090–1097.

Chatterjee, S., Sullivan, H.A., MacLennan, B.J., Xu, R., Hou, Y.Y., Lavin, T.K., Lea, N.E., Michalski, J.E., Babcock, K.R., Dietrich, S., et al. (2018). Nontoxic, double-deletion-mutant rabies viral vectors for retrograde targeting of projection neurons. Nat. Neurosci. *21*, 638–646.

Chen, L., Heider, B., Williams, G., Healy, F., Ramsden, B., and Roe, A. (2002). A chamber and artificial dura method for long-term optical imaging in the monkey. J. Neurosci. Methods *113*, 41–49.

Chen, R., Classen, J., Gerloff, C., Celnik, P., Wassermann, E.M., Hallett, M., and Cohen, L.G. (1997). Depression of motor cortex excitability by low-frequency transcranial magnetic stimulation. Neurology *48*, 1398–1403.

Chen, S.X., Kim, A.N., Peters, A.J., and Komiyama, T. (2015). Subtype-specific plasticity of inhibitory circuits in motor cortex during motor learning. Nat. Neurosci. *18*, 1109–1115.

Cheng, M.Y., Wang, E.H., Woodson, W.J., Wang, S., Sun, G., Lee, A.G., Arac, A., Fenno, L.E., Deisseroth, K., and Steinberg, G.K. (2014). Optogenetic neuronal stimulation promotes functional recovery after stroke. Proc. Natl. Acad. Sci. U. S. A. *111*, 12913–12918.

Cheng, Y.P., Huang, J.J., Yeh, C.I., and Pei, Y.C. (2021). Alternation of Neuronal Feature Selectivity Induced by Paired Optogenetic-Mechanical Stimulation in the Barrel Cortex. Front. Neural Circuits *15*, 1–16.

Chin-Hao Chen, R., Atry, F., Richner, T., Brodnick, S., Pisaniello, J., Ness, J., Suminski, A.J., Williams, J., and Pashaie, R. (2020). A system identification analysis of optogenetically evoked electrocorticography and cerebral blood flow responses. J. Neural Eng. *17*, 056049.

Christidi, F., Tsiptsios, D., Fotiadou, A., Kitmeridou, S., Karatzetzou, S., Tsamakis, K., Sousanidou, A., Psatha, E.A., Karavasilis, E., Seimenis, I., et al. (2022). Diffusion Tensor Imaging as a Prognostic Tool for Recovery in Acute and Hyperacute Stroke. Neurol. Int. *14*, 841.

Christie, B.R., and Abraham, W.C. (1992). Priming of associative long-term depression in the dentate gyrus by theta frequency synaptic activity. Neuron *9*, 79–84.

Chrobak, J.J., and Buzsáki, G. (1998). Gamma oscillations in the entorhinal cortex of the freely behaving rat. J. Neurosci. *18*, 388–398.

Clark, W.M., Albers, G.W., Madden, K.P., and Hamilton, S. (2000). The rtPA (Alteplase) 0- to 6-hour

acute stroke trial, part A (A0276g): Results of a double-blind, placebo-controlled, multicenter study. Stroke.

Clarkson, A.N., Huang, B.S., MacIsaac, S.E., Mody, I., and Carmichael, S.T. (2010). Reducing excessive GABA-mediated tonic inhibition promotes functional recovery after stroke. Nature *468*, 305–309.

Clement, E.A., Richard, A., Thwaites, M., Ailon, J., Peters, S., and Dickson, C.T. (2008). Cyclic and Sleep-Like Spontaneous Alternations of Brain State Under Urethane Anaesthesia. PLoS One *3*, e2004.

Cooper, L.N., and Bear, M.F. (2012). The BCM theory of synapse modification at 30: Interaction of theory with experiment. Nat. Rev. Neurosci. *13*, 798–810.

Cramer, S.C. (2018). Treatments to Promote Neural Repair after Stroke. J. Stroke *20*, 57–70.

Dai, P.M., Huang, H., Zhang, L., He, J., Zhao, X.D., Yang, F.H., Zhao, N., Yang, J.Z., Ge, L.J., Lin, Y., et al. (2017). A pilot study on transient ischemic stroke induced with endothelin-1 in the rhesus monkeys. Sci. Rep. *7*, 1–12.

Deegan, A.J., and Wang, R.K. (2019). Microvascular imaging of the skin. Phys. Med. Biol. *64*.

Deegan, A.J., Wang, W., Men, S., Li, Y., Song, S., Xu, J., and Wang, R.K. (2018a). Optical coherence tomography angiography monitors human cutaneous wound healing over time. Quant. Imaging Med. Surg. *8*, 135–150.

Deegan, A.J., Talebi-Liasi, F., Song, S., Li, Y., Xu, J., Men, S., Shinohara, M.M., Flowers, M.E., Lee, S.J., and Wang, R.K. (2018b). Optical coherence tomography angiography of normal skin and inflammatory dermatologic conditions. Lasers Surg. Med. *50*, 183–193.

Deegan, A.J., Lu, J., Sharma, R., Mandell, S.P., and Wang, R.K. (2021). Imaging human skin autograft integration with optical coherence tomography. Quant. Imaging Med. Surg. *11*, 78496–78796.

Dimidschstein, J., Chen, Q., Tremblay, R., Rogers, S.L., Saldi, G.A., Guo, L., Xu, Q., Liu, R., Lu, C., Chu, J., et al. (2016). A viral strategy for targeting and manipulating interneurons across vertebrate species. Nat. Neurosci. *19*, 1743–1749.

Dirnagl, U., Iadecola, C., and Moskowitz, M.A. (1999). Pathobiology of ischaemic stroke: an integrated view. Trends Neurosci. *22*, 391–397.

Dobrzanski, G., Lukomska, A., Zakrzewska, R., Posluszny, A., Kanigowski, D., Urban-Ciecko, J., Liguz-Lecznar, M., and Kossut, M. (2022). Learning-induced plasticity in the barrel cortex is disrupted by inhibition of layer 4 somatostatin-containing interneurons. Biochim. Biophys. Acta - Mol. Cell Res. *1869*, 119146.

Doeltgen, S.H., and Ridding, M.C. (2011). Low-intensity, short-interval theta burst stimulation modulates excitatory but not inhibitory motor networks. Clin. Neurophysiol. *122*, 1411–1416.

Donato, F., Rompani, S.B., and Caroni, P. (2013). Parvalbumin-expressing basket-cell network plasticity induced by experience regulates adult learning. Nature *504*, 272–276.

Donkor, E.S. (2018). Stroke in the 21st Century: A Snapshot of the Burden, Epidemiology, and Quality of Life. Stroke Res. Treat. *2018*, 3238165.

Douglas, R.J., and Martin, K.A.C. (2004). Neuronal circuits of the neocortex. Annu. Rev. Neurosci. *27*, 419–451.

Douiri, A., Rudd, A.G., and Wolfe, C.D.A. (2013). Prevalence of poststroke cognitive impairment: South London stroke register 1995-2010. Stroke *44*, 138–145.

Edwardson, M.A., Lucas, T.H., Carey, J.R., and Fetz, E.E. (2013). New modalities of brain stimulation for stroke rehabilitation. Exp. Brain Res. *224*, 335–358.

Edwardson, M.A., Avery, D.H., and Fetz, E.E. (2014). Volitional muscle activity paired with transcranial magnetic stimulation increases corticospinal excitability. Front. Neurosci. *8*.

Egger, V., Feldmeyer, D., and Sakmann, B. (1999). Coincidence detection and changes of synaptic efficacy in spiny stellate neurons in rat barrel cortex. Nat. Neurosci. *2*, 1098–1105.

Fang, Q., and Boas, D.A. (2009). Monte Carlo Simulation of Photon Migration in 3D Turbid Media Accelerated by Graphics Processing Units. Opt. Express *17*, 20178.

Feigin, V.L., Stark, B.A., Johnson, C.O., Roth, G.A., Bisignano, C., Abady, G.G., Abbasifard, M., Abbasi-Kangevari, M., Abd-Allah, F., Abedi, V., et al. (2021). Global, regional, and national burden of stroke and its risk factors, 1990-2019: A systematic analysis for the Global Burden of Disease Study 2019. Lancet Neurol. *20*, 1–26.

Feldman, D.E. (2000). Timing-based LTP and LTD at vertical inputs to layer II/III pyramidal cells in rat barrel cortex. Neuron *27*, 45–56.

Feldman, D.E. (2002). Synapses, scaling and homeostasis in vivo. Nat. Neurosci. *5*, 712–714.

Feldman, D.E. (2009). Synaptic mechanisms for plasticity in neocortex. Annu. Rev. Neurosci. *32*, 33–55.

Feldman, D.E. (2012). The Spike-Timing Dependence of Plasticity. Neuron *75*, 556–571.

Feldmeyer, D. (2012). Excitatory neuronal connectivity in the barrel cortex. Front. Neuroanat. *6*.

Ferezou, I., Haiss, F., Gentet, L.J., Aronoff, R., Weber, B., and Petersen, C.C.H. (2007). Spatiotemporal Dynamics of Cortical Sensorimotor Integration in Behaving Mice. Neuron *56*, 907–923.

Ferrier, D. (1876). The Functions of the Brain. J. Ment. Sci.

Fino, E., Glowinski, J., and Venance, L. (2005). Bidirectional activity-dependent plasticity at corticostriatal synapses. J. Neurosci. *25*, 11279–11287.

Fino, E., Deniau, J.M., and Venance, L. (2007). Cell-specific spike-timing-dependent plasticity in GABAergic and cholinergic interneurons in corticostriatal rat brain slices. J. Physiol. *586*, 265.

Foeller, E., Celikel, T., and Feldman, D.E. (2005). Inhibitory sharpening of receptive fields contributes to whisker map plasticity in rat somatosensory cortex. J. Neurophysiol. *94*, 4387–4400.

Fricke, K., Seeber, A.A., Thirugnanasambandam, N., Paulus, W., Nitsche, M.A., and Rothwell, J.C. (2011). Time course of the induction of homeostatic plasticity generated by repeated transcranial direct current stimulation of the human motor cortex. J. Neurophysiol. *105*, 1141–1149.

Le Friec, A., Desmoulin, F., Demain, B., Davoust, C., Robert, L., Duval, T., Rémy, F., Cirillo, C., and

Loubinoux, I. (2020). A Reproducible New Model of Focal Ischemic Injury in the Marmoset Monkey: MRI and Behavioural Follow-Up. Transl. Stroke Res. 1–14.

Friel, K.M., Barbay, S., Frost, S.B., Plautz, E.J., Stowe, A.M., Dancause, N., Zoubina, E. V., and Nudo, R.J. (2007). Effects of a rostral motor cortex lesion on primary motor cortex hand representation topography in primates. Neurorehabil. Neural Repair *21*, 51–61.

Frost, S.B., Barbay, S., Friel, K.M., Plautz, E.J., and Nudo, R.J. (2003). Reorganization of remote cortical regions after ischemic brain injury: A potential substrate for stroke recovery. J. Neurophysiol. *89*, 3205–3214.

Gambino, F., and Holtmaat, A. (2012). Spike-timing-dependent potentiation of sensory surround in the somatosensory cortex is facilitated by deprivation-mediated disinhibition. Neuron *75*, 490–502.

Gambrill, A.C., Storey, G.P., and Barria, A. (2011). Dynamic regulation of NMDA receptor transmission. J. Neurophysiol. *105*, 162–171.

Gatica Tossi, M.A., Stude, P., Schwenkreis, P., Tegenthoff, M., and Dinse, H.R. (2013). Behavioural and neurophysiological markers reveal differential sensitivity to homeostatic interactions between centrally and peripherally applied passive stimulation. Eur. J. Neurosci. *38*, 2893–2901.

Gerlai, R., Thibodeaux, H., Palmer, J.T., Van Lookeren Campagne, M., and Van Bruggen, N. (2000). Transient focal cerebral ischemia induces sensorimotor deficits in mice. Behav. Brain Res. *108*, 63–71.

Goldenberg, A.M., Schmidt, S., Mitelman, R., Levy, D.R., Prigge, M., Katz, Y., Yizhar, O., Beck, H., and Lampl, I. (2023). Localized chemogenetic silencing of inhibitory neurons: a novel mouse model of focal cortical epileptic activity. Cereb. Cortex *33*, 2838–2856.

Gottschalk, W. (1992). Ein Messverfahren zur Bestimmung der optischen Parameter biologischer Gewebe in vitro.

Gould, I.G., Tsai, P., Kleinfeld, D., and Linninger, A. (2017). The capillary bed offers the largest hemodynamic resistance to the cortical blood supply. J. Cereb. Blood Flow Metab. *37*, 52–68.

Grefkes, C., and Ward, N.S. (2014). Cortical reorganization after stroke: How much and how functional? Neuroscientist *20*, 56–70.

Griggs, D., Khateeb, K., Zhou, J., Liu, T., Wang, R., and Yazdan-Shahmorad, A. (2021a). Multi-modal artificial dura for simultaneous large-scale optical access and large-scale electrophysiology in non-human primate cortex. J. Neural Eng. *18*, 55006.

Griggs, D.J., Khateeb, K., Philips, S., Chan, J.W., Ojemann, W., and Yazdan-Shahmorad, A. (2019). Optimized large-scale optogenetic interface for non-human primates. In Optogenetics and Optical Manipulation 2019, S.K. Mohanty, and E.D. Jansen, eds. (SPIE), p. 3.

Griggs, D.J., Belloir, T., and Yazdan-Shahmorad, A. (2021b). Large-scale neural interfaces for optogenetic actuators and sensors in non-human primates. *11663*, 1166305.

Griggs, D.J., Bloch, J., Fisher, S., S Ojemann, W.K., Coubrough, K.M., Khateeb, K., Chu, M., and Yazdan-Shahmorad, A. (2022). Demonstration of an Optimized Large-scale Optogenetic Cortical Interface for Non-human Primates; Demonstration of an Optimized Large-scale Optogenetic Cortical Interface for Non-human Primates. 2022 44th Annu. Int. Conf. IEEE Eng. Med. Biol. Soc.

Griggs, D.J., Bloch, J., Stanis, N., Zhou, J., Fisher, S., Jahanian, H., and Yazdan-Shahmorad, A. (2024). A large-scale optogenetic neurophysiology platform for improving accessibility in NHP behavioral experiments. BioRxiv 2024.06.25.600719.

Gronlier, E., Vendramini, E., Volle, J., Wozniak-Kwasniewska, A., Antón Santos, N., Coizet, V., Duveau, V., and David, O. (2021). Single-pulse electrical stimulation methodology in freely moving rat. J. Neurosci. Methods *353*, 109092.

Gulati, T., Won, S.J., Ramanathan, D.S., Wong, C.C., Bodepudi, A., Swanson, R.A., and Ganguly, K. (2015). Robust neuroprosthetic control from the stroke perilesional cortex. J. Neurosci. *35*, 8653–8661.

Guo, L., Kondapavulur, S., Lemke, S.M., Won, S.J., and Ganguly, K. (2021). Coordinated increase of reliable cortical and striatal ensemble activations during recovery after stroke. Cell Rep. *36*, 109370.

Guo, X., Phan, C., Batarseh, S., Wei, M., and Dye, J. (2024). Risk factors and predictive markers of post-stroke cognitive decline–A mini review. Front. Aging Neurosci. *16*, 1359792.

Guo, Y., Huang, S., de Pasquale, R., McGehrin, K., Lee, H.K., Zhao, K., and Kirkwood, A. (2012). Dark exposure extends the integration window for spike-timing-dependent plasticity. J. Neurosci. *32*, 15027–15035.

Hacke, W., Kaste, M., Bluhmki, E., Brozman, M., Dávalos, A., Guidetti, D., Larrue, V., Lees, K.R., Medeghri, Z., Machnig, T., et al. (2008). Thrombolysis with Alteplase 3 to 4.5 Hours after Acute Ischemic Stroke. N. Engl. J. Med. *359*, 1317–1329.

Han, Y., Huang, M. De, Sun, M.L., Duan, S., and Yu, Y.Q. (2015). Long-Term Synaptic Plasticity in Rat Barrel Cortex. Cereb. Cortex *25*, 2741–2751.

Hara, K., and Harris, R.A. (2002). The anesthetic mechanism of urethane: The effects on neurotransmitter-gated ion channels. Anesth. Analg. *94*, 313–318.

Hardingham, N., Wright, N., Dachtler, J., and Fox, K. (2008). Sensory Deprivation Unmasks a PKA-Dependent Synaptic Plasticity Mechanism that Operates in Parallel with CaMKII. Neuron *60*, 861–874.

Harrison, T.C., Silasi, G., Boyd, J.D., and Murphy, T.H. (2013). Displacement of sensory maps and disorganization of motor cortex after targeted stroke in mice. Stroke *44*, 2300–2306.

Hebb, D.O. (1949). The Organization of Behavior.

Hebbink, J., van Blooijs, D., Huiskamp, G., Leijten, F.S.S., van Gils, S.A., and Meijer, H.G.E. (2019). A Comparison of Evoked and Non-evoked Functional Networks. Brain Topogr. *32*, 405–417.

Heffner, H.E., and Heffner, R.S. (1986). Hearing loss in Japanese macaques following bilateral auditory cortex lesions. J. Neurophysiol. *55*, 256–271.

Hensch, T.K. (2005). Critical period plasticity in local cortical circuits. Nat. Rev. Neurosci. 2005 611 *6*, 877–888.

Hess, G., and Donoghue, J.P. (1994). Long-term potentiation of horizontal connections provides a mechanism to reorganize cortical motor maps. J. Neurophysiol. *71*, 2543–2547.

Huang, Y.-Y., Colino, A., Selig, D.K., and Malenka, R.C. (1992). The influence of prior synaptic activity on the induction of long-term potentiation. Science *255*, 730–733.

Huang, Y., Hajnal, B., Entz, L., Fabó, D., Herrero, J.L., Mehta, A.D., and Keller, C.J. (2019). Intracortical Dynamics Underlying Repetitive Stimulation Predicts Changes in Network Connectivity. J. Neurosci. *39*, 6122–6135.

Humphrey, N. (1974). Vision in a monkey wihtout striate cortex: a case study. Perception *3*, 241–255.

El Husseini, N., Katzan, I.L., Rost, N.S., Blake, M.L., Byun, E., Pendlebury, S.T., Aparicio, H.J., Marquine, M.J., Gottesman, R.F., and Smith, E.E. (2023). Cognitive Impairment After Ischemic and Hemorrhagic Stroke: A Scientific Statement From the American Heart Association/American Stroke Association. Stroke *54*, E272–E291.

Iyer, M.B., Schleper, N., and Wassermann, E.M. (2003). Priming Stimulation Enhances the Depressant Effect of Low-Frequency Repetitive Transcranial Magnetic Stimulation. J. Neurosci. *23*, 10867–10872.

Jackson, A., Mavoori, J., and Fetz, E.E. (2006). Long-term motor cortex plasticity induced by an electronic neural implant. Nature *444*, 56–60.

Jacob, V., Brasier, D.J., Erchova, I., Feldman, D., and Shulz, D.E. (2007). Spike timing-dependent synaptic depression in the in vivo barrel cortex of the rat. J. Neurosci. *27*, 1271–1284.

Jacquin, A., Binquet, C., Rouaud, O., Graule-Petot, A., Daubail, B., Osseby, G.V., Bonithon-Kopp, C., Giroud, M., and Béjot, Y. (2014). Post-stroke cognitive impairment: High prevalence and determining factors in a cohort of mild stroke. J. Alzheimer's Dis. *40*, 1029–1038.

James, W. (1890). The Principles of Psychology (New York: HENRY HOLT AND COMPANY).

Jiang, W., Gu, W., Hossmann, K.A., Mies, G., and Wester, P. (2006). Establishing a photothrombotic "ring" stroke model in adult mice with late spontaneous reperfusion: Quantitative measurements of cerebral blood flow and cerebral protein synthesis. J. Cereb. Blood Flow Metab. *26*, 927–936.

Jin, L., Sullivan, H.A., Zhu, M., Lavin, T.K., Matsuyama, M., Fu, X., Lea, N.E., Xu, R., Hou, Y.Y., Rutigliani, L., et al. (2024). Long-term labeling and imaging of synaptically connected neuronal networks in vivo using double-deletion-mutant rabies viruses. Nat. Neurosci. *27*, 373–383.

Ju, N., Jiang, R., Macknik, S.L., Martinez-Conde, S., and Tang, S. (2018). Long-term all-optical interrogation of cortical neurons in awake-behaving nonhuman primates. PLoS Biol. *16*.

Kaeser, M., Wyss, A.F., Bashir, S., Hamadjida, A., Liu, Y., Bloch, J., Brunet, J.F., Belhaj-Saif, A., and Rouiller, E.M. (2010). Effects of unilateral motor cortex lesion on ipsilesional hand's reach and grasp performance in monkeys: Relationship with recovery in the contralesional hand. J. Neurophysiol. *103*, 1630–1645.

Karabanov, A., Ziemann, U., Hamada, M., George, M.S., Quartarone, A., Classen, J., Massimini, M., Rothwell, J., and Siebner, H.R. (2015). Consensus paper: Probing homeostatic plasticity of human cortex with non-invasive transcranial brain stimulation. Brain Stimul. *8*, 993–1006.

Kashani, A.H., Chen, C.L., Gahm, J.K., Zheng, F., Richter, G.M., Rosenfeld, P.J., Shi, Y., and Wang, R.K. (2017). Optical coherence tomography angiography: A comprehensive review of current

methods and clinical applications. Prog. Retin. Eye Res. *60*, 66–100.

Katan, M., and Luft, A. (2018). Global Burden of Stroke. Semin. Neurol. *38*, 208–211.

Katz, B., and Miledi, R. (1968). The role of calcium in neuromuscular facilitation. J. Physiol. *195*, 481.

Keller, C.J., Huang, Y., Herrero, J.L., Fini, M.E., Du, V., Lado, F.A., Honey, C.J., and Mehta, A.D. (2018). Induction and Quantification of Excitability Changes in Human Cortical Networks. J. Neurosci. *38*, 5384–5398.

Khanna, P., Totten, D., Novik, L., Roberts, J., Morecraft, R.J., and Ganguly, K. (2021). Low-frequency stimulation enhances ensemble co-firing and dexterity after stroke. Cell *184*, 912-930.e20.

Khateeb, K., Griggs, D.J., Sabes, P.N., and Yazdan-Shahmorad, A. (2019a). Convection enhanced delivery of optogenetic adeno-associated viral vector to the cortex of rhesus macaque under guidance of online MRI images. J. Vis. Exp. *2019*.

Khateeb, K., Yao, Z., Kharazia, V.N., Burunova, E.P., Song, S., Wang, R., and Yazdan-Shahmorad, A. (2019b). A Practical Method for Creating Targeted Focal Ischemic Stroke in the Cortex of Nonhuman Primates∗. Proc. Annu. Int. Conf. IEEE Eng. Med. Biol. Soc. EMBS 3515–3518.

Khateeb, K., Bloch, J., Rahimi, M., Griggs, D.J., Song, S., Liu, T., Le, M.N., Kharazia, V., Wang, R., and Yazdan-Shahmorad, A. (2020). A lesion-based toolbox to study cortical physiology in primates.

Khateeb, K., Bloch, J., Zhou, J., Rahimi, M., Griggs, D.J., Kharazia, V.N., Le, M.N., Wang, R.K., and Yazdan-Shahmorad, A. (2022). A versatile toolbox for studying cortical physiology in primates. Cell Reports Methods *2*, 100183.

Khodagholy, D., Gelinas, J.N., Thesen, T., Doyle, W., Devinsky, O., Malliaras, G.G., and Buzsáki, G. (2015). NeuroGrid: Recording action potentials from the surface of the brain. Nat. Neurosci. *18*, 310–315.

Kirkwood, A., Lee, H.K., and Bear, M.F. (1995). Co-regulation of long-term potentiation and experience-dependent synaptic plasticity in visual cortex by age and experience. Nature *375*, 328–331.

Kirkwood, A., Rioult, M.G., and Bear, M.F. (1996). Experience-dependent modification of synaptic plasticity in visual cortex. Nature *381*, 526–528.

Koge, J., Yoshimura, S., Koga, M., Nakai, M., Wada, S., Sasahara, Y., Shiozawa, M., Miwa, K., Ishigami, A., Sonoda, K., et al. (2023). Nationwide Trends in Reperfusion Therapy and Outcomes of Acute Ischemic Stroke According to Severity: The Japan Stroke Data Bank. Stroke Vasc. Interv. Neurol. *3*.

Komarov, M., Malerba, P., Golden, R., Nunez, P., Halgren, E., and Bazhenov, M. (2019). Selective recruitment of cortical neurons by electrical stimulation. PLOS Comput. Biol. *15*, e1007277.

Kooijmans, R.N., Sierhuis, W., Self, M.W., and Roelfsema, P.R. (2020). A Quantitative Comparison of Inhibitory Interneuron Size and Distribution between Mouse and Macaque V1, Using Calcium-Binding Proteins. Cereb. Cortex Commun. *1*, 1–14.

Kotak, V.C., Fujisawa, S., Lee, F.A., Karthikeyan, O., Aoki, C., and Sanes, D.H. (2005). Hearing loss raises excitability in the auditory cortex. J. Neurosci. *25*, 3908–3918.

Lang, N., Siebner, H.R., Ernst, D., Nitsche, M.A., Paulus, W., Lemon, R.N., and Rothwell, J.C. (2004). Preconditioning with transcranial direct current stimulation sensitizes the motor cortex to rapid-rate transcranial magnetic stimulation and controls the direction of after-effects. Biol. Psychiatry *56*, 634–639.

Lawrence, E.S., Coshall, C., Dundas, R., Stewart, J., Rudd, A.G., Howard, R., and Wolfe, C.D.A. (2001). Estimates of the prevalence of acute stroke impairments and disability in a multiethnic population. Stroke *32*, 1279–1284.

Ledochowitsch, P., Yazdan-Shahmorad, A., Bouchard, K.E., Diaz-Botia, C., Hanson, T.L., He, J.W., Seybold, B.A., Olivero, E., Phillips, E.A.K., Blanche, T.J., et al. (2015). Strategies for optical control and simultaneous electrical readout of extended cortical circuits. J. Neurosci. Methods *256*, 220–231.

Lee, H.K., and Kirkwood, A. (2019). Mechanisms of Homeostatic Synaptic Plasticity in vivo. Front. Cell. Neurosci. *13*.

Levelt, C.N., and Ḧubener, M. (2012). Critical-period plasticity in the visual cortex. Annu. Rev. Neurosci. *35*, 309–330.

Levinson, L.H., Sun, S., Paschall, C.J., Perks, K.M., Weaver, K.E., Perlmutter, S.I., Ko, A.L., Ojemann, J.G., and Herron, J.A. (2024). Data processing techniques impact quantification of cortico-cortical evoked potentials. J. Neurosci. Methods *408*, 110130.

Levy, R.M., Harvey, R.L., Kissela, B.M., Winstein, C.J., Lutsep, H.L., Parrish, T.B., Cramer, S.C., and Venkatesan, L. (2016). Epidural Electrical Stimulation for Stroke Rehabilitation. Neurorehabil. Neural Repair.

Li, H.R., Harb, M., Heath, J.E., Trippett, J.S., Shapiro, M.G., and Szablowski, J.O. (2024). Engineering viral vectors for acoustically targeted gene delivery. Nat. Commun. 2024 151 *15*, 1–12.

Li, L., Gainey, M.A., Goldbeck, J.E., and Feldman, D.E. (2014). Rapid homeostasis by disinhibition during whisker map plasticity. Proc. Natl. Acad. Sci. U. S. A. *111*, 1616–1621.

Li, S., Lu, Y., Fang, S., Wang, L., and Peng, B. (2023). Inpatient rehabilitation therapy in stroke patients with reperfusion therapy: a national prospective registry study. BMC Neurol. *23*, 146.

Li, Y., Wei, W., and Wang, R.K. (2018). Capillary flow homogenization during functional activation revealed by optical coherence tomography angiography based capillary velocimetry. Sci. Rep. *8*, 1–9.

Lin, S.C., Gervasoni, D., and Nicolelis, M.A.L. (2006). Fast modulation of prefrontal cortex activity by basal forebrain noncholinergic neuronal ensembles. J. Neurophysiol. *96*, 3209–3219.

Liu, Y., and Rouiller, E.M. (1999). Mechanisms of recovery of dexterity following unilateral lesion of the sensorimotor cortex in adult monkeys. In Experimental Brain Research, (Springer Verlag), pp. 149–159.

Lo, J.W., Crawford, J.D., Desmond, D.W., Godefroy, O., Jokinen, H., Mahinrad, S., Bae, H.J., Lim, J.S., Köhler, S., Douven, E., et al. (2019). Profile of and risk factors for poststroke cognitive impairment in diverse ethnoregional groups. Neurology *93*, E2257–E2271.

Lu, J.T., Li, C.Y., Zhao, J.P., Poo, M.M., and Zhang, X.H. (2007). Spike-timing-dependent plasticity of

neocortical excitatory synapses on inhibitory interneurons depends on target cell type. J. Neurosci. *27*, 9711–9720.

Lucas, T.H., and Fetz, E.E. (2013). Myo-Cortical Crossed Feedback Reorganizes Primate Motor Cortex Output. J. Neurosci. *33*, 5261–5274.

MacKay, W.A., and Mendoncc ą, A.J. (1995). Field potential oscillatory bursts in parietal cortex before and during reach. Brain Res. *704*, 167–174.

Macknik, S.L., Alexander, R.G., Caballero, O., Chanovas, J., Nielsen, K.J., Nishimura, N., Schaffer, C.B., Slovin, H., Babayoff, A., Barak, R., et al. (2019). Advanced Circuit and Cellular Imaging Methods in Nonhuman Primates. J. Neurosci. *39*, 8267–8274.

Maeda, M., Takamatsu, H., Furuichi, Y., Noda, A., Awaga, Y., Tatsumi, M., Yamamoto, M., Ichise, R., Nishimura, S., and Matsuoka, N. (2005). Characterization of a novel thrombotic middle cerebral artery occlusion model in monkeys that exhibits progressive hypoperfusion and robust cortical infarction. J. Neurosci. Methods *146*, 106–115.

Markram, H., Lübke, J., Frotscher, M., and Sakmann, B. (1997). Regulation of synaptic efficacy by coincidence of postsynaptic APs and EPSPs. Science *275*, 213–215.

Maurya, S., Sarangi, P., and Jayandharan, G.R. (2022). Safety of Adeno-associated virus-based vector-mediated gene therapy—impact of vector dose. Cancer Gene Ther. *29*, 1305–1306.

McIntyre, C.C., and Grill, W.M. (1999). Excitation of central nervous system neurons by nonuniform electric fields. Biophys. J. *76*, 878–888.

McKeon, R., Smith, J.A., Reeve, C.D.C., Edghill, E.M., Hardie, R.P., Gaye, R.K., Stocks, J.L., Joachim, H.H., Beare, J.I., Thompson, D.W., et al. (1967). The Basic Works of Aristotle (Random House).

Meyer, H.S., Schwarz, D., Wimmer, V.C., Schmitt, A.C., Kerr, J.N.D., Sakmann, B., and Helmstaedter, M. (2011). Inhibitory interneurons in a cortical column form hot zones of inhibition in layers 2 and 5A. Proc. Natl. Acad. Sci. U. S. A. *108*, 16807–16812.

Miller, K.D., and MacKay, D.J.C. (1994). The Role of Constraints in Hebbian Learning. Neural Comput. *6*, 100–126.

Müller, J.F.M., Orekhov, Y., Liu, Y., and Ziemann, U. (2007). Homeostatic plasticity in human motor cortex demonstrated by two consecutive sessions of paired associative stimulation. Eur. J. Neurosci. *25*, 3461–3468.

Murata, Y., Higo, N., Oishi, T., Yamashita, A., Matsuda, K., Hayashi, M., and Yamane, S. (2008). Effects of motor training on the recovery of manual dexterity after primary motor cortex lesion in macaque monkeys. J. Neurophysiol. *99*, 773–786.

Murphy, T.H., and Corbett, D. (2009). Plasticity during stroke recovery: from synapse to behaviour. Nat. Rev. Neurosci. 2009 1012 *10*, 861–872.

Murphy, A.P., Leopold, D.A., Humphreys, G.W., and Welchman, A.E. (2016). Lesions to right posterior parietal cortex impair visual depth perception from disparity but not motion cues. Philos. Trans. R. Soc. B Biol. Sci. *371*.

Nagai, Y., Miyakawa, N., Takuwa, H., Hori, Y., Oyama, K., Ji, B., Takahashi, M., Huang, X.P., Slocum, S.T., DiBerto, J.F., et al. (2020). Deschloroclozapine, a potent and selective chemogenetic actuator

enables rapid neuronal and behavioral modulations in mice and monkeys. Nat. Neurosci. *23*, 1157–1167.

Nishimura, Y., Perlmutter, S.I., Eaton, R.W., and Fetz, E.E. (2013). Spike-timing dependent plasticity in primate corticospinal connections induced during free behavior. Neuron *80*, 1301.

Nitsche, M.A., Roth, A., Kuo, M.F., Fischer, A.K., Liebetanz, D., Lang, N., Tergau, F., and Paulus, W. (2007). Timing-Dependent Modulation of Associative Plasticity by General Network Excitability in the Human Motor Cortex. J. Neurosci. *27*, 3807.

Nitsche, M.A., Cohen, L.G., Wassermann, E.M., Priori, A., Lang, N., Antal, A., Paulus, W., Hummel, F., Boggio, P.S., Fregni, F., et al. (2008). Transcranial direct current stimulation: State of the art 2008. Brain Stimul. *1*, 206–223.

Nudo, R.J., and Milliken, G.W. (1996). Reorganization of movement representations in primary motor cortex following focal ischemic infarcts in adult squirrel monkeys. J. Neurophysiol. *75*, 2144–2149.

Nudo, R.J., Wise, B.M., SiFuentes, F., and Milliken, G.W. (1996). Neural substrates for the effects of rehabilitative training on motor recovery after ischemic infarct. Science (80-.). *272*, 1791–1794.

Nudo, R.J., Larson, D., Plautz, E.J., Friel, K.M., Barbay, S., and Frost, S.B. (2003). A squirrel monkey model of poststroke motor recovery. ILAR J. *44*, 161–174.

O'Brien, R.J., Kamboj, S., Ehlers, M.D., Rosen, K.R., Fischbach, G.D., and Huganir, R.L. (1998). Activity-dependent modulation of synaptic AMPA receptor accumulation. Neuron *21*, 1067–1078.

Ojemann, W., Griggs, D., Ip, Z., Caballero, O., Jahanian, H., Martinez-Conde, S., Macknik, S., and Yazdan-Shahmorad, A. (2020). A MRI-Based Toolbox for Neurosurgical Planning in Nonhuman Primates. J. Vis. Exp. *2020*, 1–16.

Padberg, J., Recanzone, G., Engle, J., Cooke, D., Goldring, A., and Krubitzer, L. (2010). Lesions in posterior parietal area 5 in monkeys result in rapid behavioral and cortical plasticity. J. Neurosci. *30*, 12918–12935.

Park, K.S., Shin, J.G., Qureshi, M.M., Chung, E., and Eom, T.J. (2018). Deep brain optical coherence tomography angiography in mice: in vivo, noninvasive imaging of hippocampal formation. Sci. Rep. *8*, 11614.

Paxinos, G., and Watson, C. (2007). The Rat Brain in Stereotaxic Coordinates (Elsevier Inc.).

Paxinos, G., Huang, X.-F., Petrides, M., and Toga, A.W. (2009). The Rhesus Monkey Brain in Stereotaxic Coordinates (San Diego, California, USA).

Peters, A.J., Liu, H., and Komiyama, T. (2017). Learning in the Rodent Motor Cortex. Annu. Rev. Neurosci. *40*, 77–97.

Philpot, B.D., Sekhar, A.K., Shouval, H.Z., and Bear, M.F. (2001). Visual experience and deprivation bidirectionally modify the composition and function of NMDA receptors in visual cortex. Neuron *29*, 157–169.

Philpot, B.D., Espinosa, J.S., and Bear, M.F. (2003). Evidence for Altered NMDA Receptor Function as a Basis for Metaplasticity in Visual Cortex. J. Neurosci. *23*, 5583.

Pierce, A.F., Shupe, L., Fetz, E., and Yazdan-Shahmorad, A. (2025). Flexible modeling of large-scale neural network stimulation: electrical and optical extensions to The Virtual Electrode Recording Tool for EXtracellular Potentials (VERTEX). BioRxiv 2024.08.20.608687.

Pons, T.P., Garraghtyt, P.E., and Mishkin, M. (1988). Lesion-induced plasticity in the second somatosensory cortex of adult macaques.

Pötter-Nerger, M., Fischer, S., Mastroeni, C., Groppa, S., Deuschl, G., Volkmann, J., Quartarone, A., Münchau, A., and Siebner, H.R. (2009). Inducing Homeostatic-Like Plasticity in Human Motor Cortex Through Converging Corticocortical Inputs. J. Neurophysiol. *102*, 3180–3190.

Prabhakaran, S., Ruff, I., and Bernstein, R.A. (2015). Acute Stroke Intervention A Systematic Review.

Quinlan, E.M., Olstein, D.H., and Bear, M.F. (1999). Bidirectional, experience-dependent regulation of N-methyl-D-aspartate receptor subunit composition in the rat visual cortex during postnatal development. Proc. Natl. Acad. Sci. U. S. A. *96*, 12876–12880.

Rannals, M.D., and Kapur, J. (2011). Homeostatic strengthening of inhibitory synapses is mediated by the accumulation of GABA A receptors. J. Neurosci. *31*, 17701–17712.

Rebesco, J.M., and Miller, L.E. (2011). Enhanced detection threshold for in vivo cortical stimulation produced by Hebbian conditioning. J. Neural Eng. *8*.

Rebesco, J.M., Stevenson, I.H., Körding, K.P., Solla, S.A., and Miller, L.E. (2010). Rewiring neural interactions by micro-stimulation. Front. Syst. Neurosci. *4*, 1536.

Rumbaugh, G., and Vicini, S. (1999). Distinct synaptic and extrasynaptic NMDA receptors in developing cerebellar granule neurons. J. Neurosci. *19*, 10603–10610.

Rutherford, L.C., Nelson, S.B., and Turrigiano, G.G. (1998). BDNF has opposite effects on the quantal amplitude of pyramidal neuron and interneuron excitatory synapses. Neuron *21*, 521–530.

Sceniak, M.P., and MacIver, M.B. (2006). Cellular actions of urethane on rat visual cortical neurons in vitro. J. Neurophysiol. *95*, 3865–3874.

Schaffer, C.B., Friedman, B., Nishimura, N., Schroeder, L.F., Tsai, P.S., Ebner, F.F., Lyden, P.D., and Kleinfeld, D. (2006). Two-photon imaging of cortical surface microvessels reveals a robust redistribution in blood flow after vascular occlusion. PLoS Biol. *4*, 258–270.

Schmid, M.C., Panagiotaropoulos, T., Augath, M.A., Logothetis, N.K., and Smirnakis, S.M. (2009). Visually Driven Activation in Macaque Areas V2 and V3 without Input from the Primary Visual Cortex. PLoS One *4*, e5527.

Schwock, F., Bloch, J., Khateeb, K., Zhou, J., Atlas, L., and Yazdan-Shahmorad, A. (2024). Inferring Neural Communication Dynamics from Field Potentials Using Graph Diffusion Autoregression. BioRxiv 2024.02.26.582177.

Seeman, S.C., Mogen, B.J., Fetz, E.E., and Perlmutter, S.I. (2017). Paired stimulation for spike-timing-dependent plasticity in primate sensorimotor cortex. J. Neurosci. *37*, 1935–1949.

Siebner, H.R., Lang, N., Rizzo, V., Nitsche, M.A., Paulus, W., Lemon, R.N., and Rothwell, J.C. (2004). Preconditioning of Low-Frequency Repetitive Transcranial Magnetic Stimulation with Transcranial Direct Current Stimulation: Evidence for Homeostatic Plasticity in the Human Motor Cortex. J.

Neurosci. *24*, 3379–3385.

Sjöström, P.J., and Häusser, M. (2006). A Cooperative Switch Determines the Sign of Synaptic Plasticity in Distal Dendrites of Neocortical Pyramidal Neurons. Neuron *51*, 227–238.

Smits, E., Gordon, D.C., Witte, S., Rasmusson, D.D., and Zarzecki, P. (1991). Synaptic potentials evoked by convergent somatosensory and corticocortical inputs in raccoon somatosensory cortex: Substrates for plasticity. J. Neurophysiol. *66*, 688–695.

Sommer, C.J. (2017). Ischemic stroke: experimental models and reality. Acta Neuropathol.

Song, S., and Abbott, L.F. (2001). Cortical Development and Remapping through Spike Timing-Dependent Plasticity. Neuron *32*, 339–350.

Song, J., Patel, R. V., Sharif, M., Ashokan, A., and Michaelides, M. (2022). Chemogenetics as a neuromodulatory approach to treating neuropsychiatric diseases and disorders. Mol. Ther. *30*, 990–1005.

Stanis, N., Khateeb, K., Zhou, J., Wang, R.K., and Yazdan-Shahmorad, A. (2023). Protocol to study ischemic stroke by photothrombotic lesioning in the cortex of non-human primates. STAR Protoc. *4*, 102496.

Szablowski, J.O., Lee-Gosselin, A., Lue, B., Malounda, D., and Shapiro, M.G. (2018). Acoustically targeted chemogenetics for the non-invasive control of neural circuits. Nat. Biomed. Eng. *2*, 475–484.

Takano, B., Drzezga, A., Peller, M., Sax, I., Schwaiger, M., Lee, L., and Siebner, H.R. (2004). Short-term modulation of regional excitability and blood flow in human motor cortex following rapid-rate transcranial magnetic stimulation. Neuroimage *23*, 849–859.

Takatsuru, Y., Fukumoto, D., Yoshitomo, M., Nemoto, T., Tsukada, H., and Nabekura, J. (2009). Neuronal circuit remodeling in the contralateral cortical hemisphere during functional recovery from cerebral infarction. J. Neurosci. *29*, 10081–10086.

Takeuchi, N., and Izumi, S.I. (2015). Combinations of stroke neurorehabilitation to facilitate motor recovery: perspectives on Hebbian plasticity and homeostatic metaplasticity. Front. Hum. Neurosci. *9*, 349.

Tavildar, S., Mogen, B., Zanos, S., Seeman, S.C., Perlmutter, S.I., Fetz, E., and Ashrafi, A. (2019). Inferring cortical connectivity from ECOG signals using graph signal processing. IEEE Access *7*, 109349–109362.

Teo, L., and Bourne, J.A. (2014). A reproducible and translatable model of focal ischemia in the visual cortex of infant and adult marmoset monkeys. Brain Pathol. *24*, 459–474.

Thio, B.J., and Grill, W.M. (2023). Relative contributions of different neural sources to the EEG. Neuroimage *275*.

Thomson, A.M., and Lamy, C. (2007). Functional Maps of Neocortical Local Circuitry. Front. Neurosci. *1*, 19–42.

Ting, W.K.C., Huot-Lavoie, M., and Ethier, C. (2020). Paired associative stimulation fails to induce plasticity in freely behaving intact rats. ENeuro *7*.

Todd, G., Flavel, S.C., and Ridding, M.C. (2009). Priming theta-burst repetitive transcranial magnetic stimulation with low- and high-frequency stimulation. Exp. Brain Res. *195*, 307–315.

Tort, A.B.L., Komorowski, R., Eichenbaum, H., and Kopell, N. (2010). Measuring phase-amplitude coupling between neuronal oscillations of different frequencies. J. Neurophysiol. *104*, 1195–1210.

Trautmann, E.M., O'Shea, D.J., Sun, X., Marshel, J.H., Crow, A., Hsueh, B., Vesuna, S., Cofer, L., Bohner, G., Allen, W., et al. (2021). Dendritic calcium signals in rhesus macaque motor cortex drive an optical brain-computer interface. Nat. Commun. 2021 121 *12*, 1–20.

Tremblay, S., Acker, L., Afraz, A., Albaugh, D.L., Amita, H., Andrei, A.R., Angelucci, A., Aschner, A., Balan, P.F., Basso, M.A., et al. (2020). An Open Resource for Non-human Primate Optogenetics. Neuron *108*, 1075-1090.e6.

Turrigiano, G. (2012). Homeostatic synaptic plasticity: Local and global mechanisms for stabilizing neuronal function. Cold Spring Harb. Perspect. Biol. *4*.

Turrigiano, G.G., and Nelson, S.B. (2000). Hebb and homeostasis in neuronal plasticity. Curr. Opin. Neurobiol. *10*, 358–364.

Turrigiano, G.G., Leslie, K.R., Desai, N.S., Rutherford, L.C., and Nelson, S.B. (1998). Activity-dependent scaling of quantal amplitude in neocortical neurons. Nature *391*, 892–896.

Tzounopoulos, T., Kim, Y., Oertel, D., and Trussell, L.O. (2004). Cell-specific, spike timing-dependent plasticities in the dorsal cochlear nucleus. Nat. Neurosci. *7*, 719–725.

Vallar, G., Rusconi, M.L., Bignamini, L., Geminiani, G., and Perani, D. (1994). Anatomical correlates of visual and tactile extinction in humans: A clinical CT scan study. J. Neurol. Neurosurg. Psychiatry *57*, 464–470.

Vandenberghe, R., and Gillebert, C.R. (2009). Parcellation of parietal cortex: Convergence between lesion-symptom mapping and mapping of the intact functioning brain. Behav. Brain Res. *199*, 171–182.

Vargo, S.M., Hong, N., Belloir, T., Stanis, N., Zhou, J., Khateeb, K., Hatanaka, G., Ahmed, Z., Kimukin, I., Griggs, D.J., et al. (2025). Smart Dura: a functional artificial dura for multimodal neural recording and modulation. BioRxiv 2025.02.26.640369.

Virani, S.S., Alonso, A., Aparicio, H.J., Benjamin, E.J., Bittencourt, M.S., Callaway, C.W., Carson, A.P., Chamberlain, A.M., Cheng, S., Delling, F.N., et al. (2021). Heart Disease and Stroke Statistics - 2021 Update: A Report From the American Heart Association. Circulation *143*, E254–E743.

Virley, D., Hadingham, S.J., Roberts, J.C., Farnfield, B., Elliott, H., Whelan, G., Golder, J., David, C., Parsons, A.A., and Hunter, A.J. (2004). A New Primate Model of Focal Stroke: Endothelin-1-Induced Middle Cerebral Artery Occlusion and Reperfusion in the Common Marmoset. J. Cereb. Blood Flow Metab. *24*, 24–41.

Vitureira, N., and Goda, Y. (2013). The interplay between hebbian and homeostatic synaptic plasticity. J. Cell Biol. *203*, 175–186.

Vogels, T.P., Sprekeler, H., Zenke, F., Clopath, C., and Gerstner, W. (2011). Inhibitory plasticity balances excitation and inhibition in sensory pathways and memory networks. Science (80-.). *334*, 1569–1573.

Wang, H.C., LeMessurier, A.M., and Feldman, D.E. (2022). Tuning instability of non-columnar neurons in the salt-and-pepper whisker map in somatosensory cortex. Nat. Commun. *13*, 1–18.

Whitlock, J.R. (2017). Posterior parietal cortex. Curr. Biol. *27*, R691–R695.

Whitt, J.L., Petrus, E., and Lee, H.K. (2014). Experience-dependent homeostatic synaptic plasticity in neocortex. Neuropharmacology *78*, 45–54.

Wickersham, I.R., Finke, S., Conzelmann, K.K., and Callaway, E.M. (2007). Retrograde neuronal tracing with a deletion-mutant rabies virus. Nat. Methods *4*, 47–49.

Wilmes, K.A., Sprekeler, H., and Schreiber, S. (2016). Inhibition as a Binary Switch for Excitatory Plasticity in Pyramidal Neurons. PLOS Comput. Biol. *12*, e1004768.

Winship, I.R., and Murphy, T.H. (2008). In vivo calcium imaging reveals functional rewiring of single somatosensory neurons after stroke. J. Neurosci. *28*, 6592–6606.

Wongsarnpigoon, A., and Grill, W.M. (2008). Computational modeling of epidural cortical stimulation. J. Neural Eng. *5*, 443–454.

Wu, D., Chen, J., Wang, B., Zhang, M., Shi, J., Ma, Y., Zhu, Z., Yan, F., He, X., Li, S., et al. (2016). Endovascular ischemic stroke models of adult rhesus monkeys: A comparison of two endovascular methods. Sci. Rep. *6*, 1–10.

Wurtz, R.H., and Goldberg, M.E. (1972). Activity of superior colliculus in behaving monkey. IV. Effects of lesions on eye movements. J. Neurophysiol. *35*, 587–596.

Xerri, C., Merzenich, M.M., Peterson, B.E., and Jenkins, W. (1998). Plasticity of primary somatosensory cortex paralleling sensorimotor skill recovery from stroke in adult monkeys. J. Neurophysiol. *79*, 2119–2148.

Xu, J., Song, S., Wei, W., and Wang, R.K. (2017). Wide field and highly sensitive angiography based on optical coherence tomography with akinetic swept source. Biomed. Opt. Express *8*, 420.

Xue, M., Atallah, B. V., and Scanziani, M. (2014). Equalizing excitation–inhibition ratios across visual cortical neurons. Nat. 2014 5117511 *511*, 596–600.

Yaroslavsky, A.N., Schulze, P.C., Yaroslavsky, I. V., Schober, R., Ulrich, F., and Schwarzmaier, H.J. (2002). Optical properties of selected native and coagulated human brain tissues in vitro in the visible and near infrared spectral range. Phys. Med. Biol. *47*, 2059–2073.

Yazdan-Shahmorad, A., Kipke, D.R., and Lehmkuhle, M.J. (2011). Polarity of cortical electrical stimulation differentially affects neuronal activity of deep and superficial layers of rat motor cortex. Brain Stimul. *4*, 228–241.

Yazdan-Shahmorad, A., Kipke, D.R., and Lehmkuhle, M.J. (2013). High gamma power in ECoG reflects cortical electrical stimulation effects on unit activity in layers V/VI. J. Neural Eng. *10*, 066002.

Yazdan-Shahmorad, A., Diaz-Botia, C., Hanson, T., Ledochowitsch, P., Maharabiz, M.M., and Sabes, P.N. (2015). Demonstration of a setup for chronic optogenetic stimulation and recording across cortical areas in non-human primates. Opt. Tech. Neurosurgery, Neurophotonics, Optogenetics II *9305*, 93052K.

Yazdan-Shahmorad, A., Diaz-Botia, C., Hanson, T.L., Kharazia, V., Ledochowitsch, P., Maharbiz, M.M., and Sabes, P.N. (2016). A Large-Scale Interface for Optogenetic Stimulation and Recording in Nonhuman Primates. Neuron *89*, 927–939.

Yazdan-Shahmorad, A., Silversmith, D.B., Kharazia, V., and Sabes, P.N. (2018a). Targeted cortical reorganization using optogenetics in non-human primates. Elife.

Yazdan-Shahmorad, A., Tian, N., Kharazia, V., Samaranch, L., Kells, A., Bringas, J., He, J., Bankiewicz, K., and Sabes, P.N. (2018b). Widespread optogenetic expression in macaque cortex obtained with MR-guided, convection enhanced delivery (CED) of AAV vector to the thalamus. J. Neurosci. Methods.

Yazdan-Shahmorad, A., Silversmith, D.B., and Sabes, P.N. (2018c). Novel techniques for large-scale manipulations of cortical networks in non-human primates. Conf. Proc. ... Annu. Int. Conf. IEEE Eng. Med. Biol. Soc. IEEE Eng. Med. Biol. Soc. Annu. Conf. *2018*, 5479–5482.

Yee, A.X., Hsu, Y.T., and Chen, L. (2017). A metaplasticity view of the interaction between homeostatic and Hebbian plasticity. Philos. Trans. R. Soc. Lond. B. Biol. Sci. *372*.

Zeiger, W.A., Marosi, M., Saggi, S., Noble, N., Samad, I., and Portera-Cailliau, C. (2021). Barrel cortex plasticity after photothrombotic stroke involves potentiating responses of pre-existing circuits but not functional remapping to new circuits. Nat. Commun. 2021 121 *12*, 1–14.

Zenke, F., and Gerstner, W. (2017). Hebbian plasticity requires compensatory processes on multiple timescales. Philos. Trans. R. Soc. B Biol. Sci. *372*.

Zenke, F., Gerstner, W., and Ganguli, S. (2017). The temporal paradox of Hebbian learning and homeostatic plasticity. Curr. Opin. Neurobiol. *43*, 166–176.